Numerical Simulations of Kinetic Plasmas

by

Vegard Lundby Rekaa

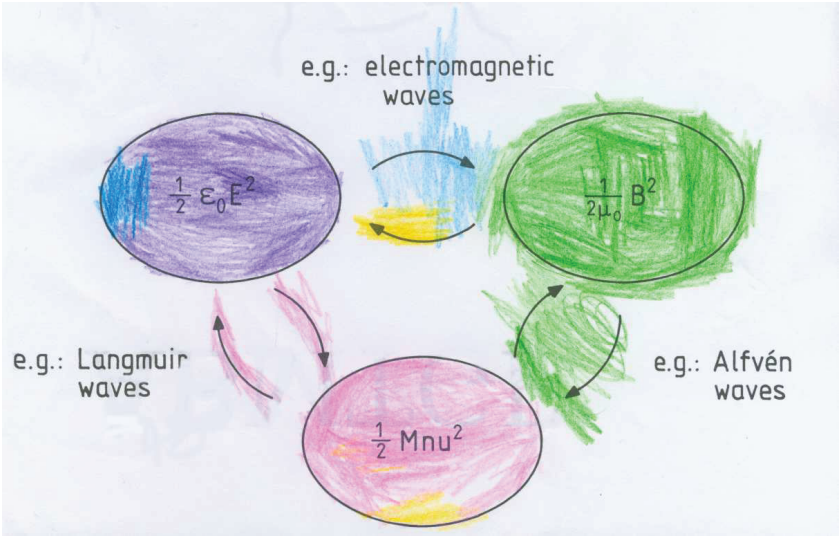

Dissertation

for the degree of

Philosophiæ Doctor

Department of Physics

University of Oslo

March 2014

Series of dissertations submitted to the
Faculty of Mathematics and Natural Sciences, University of Oslo
No. 1496

ISSN 1501-7710

Cover: Inger Sandved Anfinsen.
Printed in Norway: AIT Oslo AS.

Produced in co-operation with Akademika Publishing.
The thesis is produced by Akademika Publishing merely in connection with the thesis defence. Kindly direct all inquiries regarding the thesis to the copyright holder or the unit which grants the doctorate.

The figure on the opposite page illustrates the energy exchange in plasma waves. Colourized by the author's daughter, Marie Rekaa, 4 years old.

Acknowledgments

I would like to thank my supervisors at the University of Oslo, Professor Hans Pécseli and Professor Jan Trulsen for their advice and guidance in this research. Your guidance, good company and patience with my endless queries have made my Ph.D. studies a positive experience from the beginning. Your words of advice and humorous comments will be missed! I would also like to thank Professor Sandra Chapman and Professor Richard Dendy at the University of Warwick for their hospitality and guidance with the final paper in this thesis. It has been a pleasure working with you.

Further, many thanks to my colleagues and fellow students at the University of Oslo and University of Warwick for their excellent company and fruitful discussions. Their support and good ideas was always there for me when nothing else seemed to work. A special thanks to Dr. Wojchiech Miloch who has followed me throughout my Ph.D. with his helpful advice and ideas, and inspired me to always stretch further in order to reach my goals.

Last but not least, I would like to thank my family and friends, especially my wife Ellen and two daughters Marie and Tuva. Their warmth and support motivated me towards this final goal, my Ph.D. thesis, which you have in front of you right now.

In memory of my grandfather

Sven Erik Lundby (1918-2013)
For his endless curiosity and support

List of publications

Papers included in the dissertation

Paper I V. L. Rekaa, H. L. Pécseli, J. K. Trulsen, Numerical studies of a plasma diode with external forcing, *Physics of Plasmas*, **19**, 082115 (2012)

Paper II V. L. Rekaa, H. L. Pécseli, J. K. Trulsen, Self-similar space-time evolution of an initial density discontinuity, *Physics of Plasmas*, **20**, 072117 (2013)

Paper III V. L. Rekaa, S. C. Chapman, R. O. Dendy, Ion pre-acceleration in fully self-consistent PIC simulations of supercritical perpendicular reforming shocks in multiple ion species plasmas, *Astrophysical Journal* (submitted)

Relevant paper not included in the dissertation

Paper IV W. J. Miloch, V. L. Rekaa, H. L. Pécseli, J. K. Trulsen, Ion acoustic double layers forming behind irradiated solid objects in streaming plasmas, *J. Plasma Physics*, **76**, 429-439 (2010)

Relevant conference proceeding

Conf I V. L. Rekaa, S. C. Chapman, R. O. Dendy, Perpendicular shock reformation and multi-ion species acceleration in astrophysical plasmas, 40th EPS Conference on Plasma Physics, Espoo, Finland 07/2013

Contents

List of Figures

Chapter 1

Introduction

Plasma is a partially or fully ionized gas, in which a portion of the electrons are free to move without being bound to an atom or molecule. The individual motion of charged particles makes the plasma electrically conductive and therefore subject also to electromagnetic forces. Charged plasma particles give rise to space-charge regions and local currents, thereby generating electric and magnetic fields in the plasma. Plasma particles respond collectively to these fields, allowing complicated couplings of plasma oscillations, plasma waves, instabilities and electric currents.

Studies of plasma media are often motivated by the wide spread occurrence of plasmas in the Earth's near and distant space environments, where most of the classical matter is in the plasma state ($> 99\%$). In our Solar system, for instance, most of the matter is in the Sun, where it can safely be taken to be fully ionized. The greatest incentive for modern plasma studies is concentrated around fusion plasma physics (Wilhelmsson, 2000), which may be the solution to mankind's energy demand for all foreseeable future. Experimental devices have an important role in plasma physics research. One example is Q-machines, where low temperature Alkali plasmas are studied by means of Langmuir probes. Other devices of interest are the double plasma devices and various forms of discharges, each designed to study different plasma phenomena. An overview on the occurrence of plasmas in nature and experiments is illustrated in Figure 1.1, where the various plasmas are organized by their typical

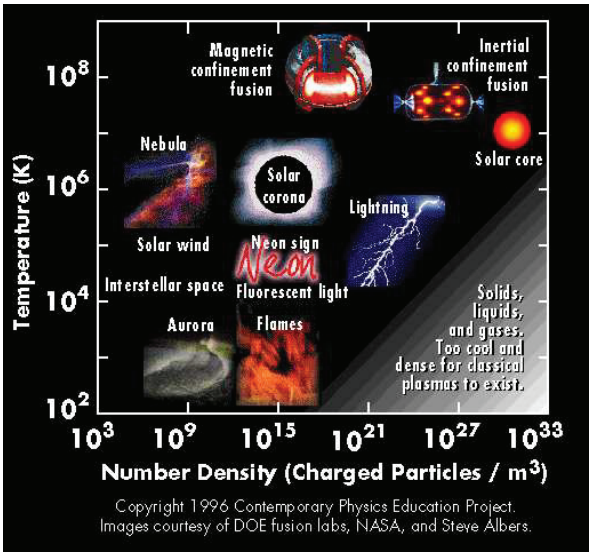

Figure 1.1: Plasmas are found in many contexts, both natural and in industry and experiments. This figure present some of these and their general properties in terms of temperature T and number densities n.

temperatures and number densities.

Numerical simulations provides a bridge between theory and experiments in plasma physics. Theoretical models often assume idealized, simplified models, e.g. through linearisation. Experimental studies suffer from limited diagnostics and secondary effects from the diagnostic equipment. This thesis focus on the use of kinetic simulations of plasmas, where the plasma particle dynamics are modelled using their positions, velocities and time as independent variables, using a continuity equation in phase space.

This thesis is organized as follows: Chapter 2 introduces some basic concepts in plasma physics, and the theoretical framework from which the numerical simulations of this thesis are developed. Chapter 3 gives details of Particle-in-Cell methods used in the numerical simulations, with emphasis on the implementation of open boundaries and binary collisions. Chapter 4 gives a short summary of the attached papers, in which the results of this thesis are presented.

Chapter 2

Theoretical background

In this chapter, some basic concepts in plasma physics are laid out, giving the reader the basic tools to understand the results in the final chapters of this thesis. In section 2.1 the concept of collective dynamics of the plasma particles is introduced, and the most common mathematical descriptions of plasmas: magnetohydrodynamics in section 2.4 and plasma kinetic theory in section 2.5. Section 2.6 introduces the basic concepts of collisions in plasmas and the description of these in kinetic theory, while section 2.7 presents some instructive examples of waves and oscillations in plasmas relevant for this thesis.

2.1 Debye shielding

There exists a limit in plasma physics where the influence of individual particles can be neglected compared to the collective dynamics of the plasma, a limit most easily explained through the following example: Consider a point charge q_0 placed within a quasi-neutral plasma. The Coulomb potential associated with the charge in free space is given as a function of the distance r from q_0, $\phi_0(r) = q_0/4\pi\varepsilon_0 r$, where ε_0 is the electric permittivity of free space. The surrounding plasma particles react to the Coulomb potential and reorganize, effectively shielding the plasma particles outside a characteristic radius $r = \lambda_D$ from q_0. Mathematically, the shielding enters as an exponential correction to ϕ_0,

$$\phi(r) = \phi_0(r)e^{-r/\lambda_D} \, .$$

This effect is known as *Debye shielding*, and the characteristic length scale λ_D known as *Debye length* is given by the expression

$$\lambda_D = \sqrt{\frac{\varepsilon_0 k_B T}{\sum_s n_s q_s^2}} \, , \tag{2.1}$$

where k_B is Boltzmann's constant, T is the plasma temperature in units of Kelvin and n_s and q_s the number density and charge of the involved particle species s. The potentials $\phi_0(r)$ and $\phi(r)$ are shown in Figure 2.1 on semi-log axes.

The general result of the foregoing analysis is that any charged particle interact with other plasma particles within a sphere of radius $r = \lambda_D$ centred at the position of the particle; a *Debye*

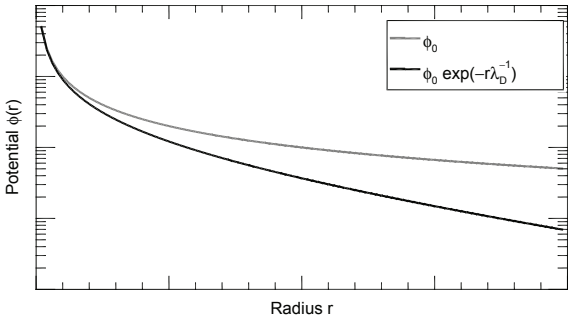

Figure 2.1: The Coulomb potential $\phi_0(r)$ and the shielded potential $\phi(r)$ (on logarithmic axis) as functions of distance r (on linear axis) from the point-charge q_0.

sphere. A dimensionless quantity can be formed from the Debye length and the plasma density,

$$N_p \equiv n\lambda_D^3 \,, \tag{2.2}$$

which is known as the *plasma parameter* and is commonly understood as the number of particles in the Debye sphere. Even though the number density n explicitly enters the expression for N_p, suggesting that high values of n correspond to high values of N_p, but at the same time the Debye shielding becomes more effective at high values of n, reducing the size of the Debye sphere. Effectively, the plasma parameter is reduced with increasing number density n, given by the scaling $N_p \sim n^{-1/2}$. From these arguments, it is shown that for a fixed temperature T, dilute plasmas are dominated by collective dynamics while in dense plasmas, more particles follow individual trajectories.

2.2 Plasma dynamics

Plasmas, as any other medium, must obey a continuity equation in some form relating the flow of some quantity with the temporal changes of that quantity in a finite volume. Taking fluid theory as an example, where macroscopic quantities like number density n, mean velocity $\mathbf{U}$ and temperature T are functions of the position $\mathbf{x}$ and time t alone, one relation of these quantities is given by the continuity equation for number density n and particle flux $n\mathbf{U}$,

$$\frac{\partial n}{\partial t} + \nabla \cdot (n\mathbf{U}) = \mathcal{P} - \mathcal{S} \,. \tag{2.3}$$

The source (production) $\mathcal{P}$ and sink $\mathcal{S}$ terms are included to maintain generality of the equation. Plasmas in which these are important are e.g. in the lower ionosphere and in plasma devices operated at high number densities. However, examples of plasmas where these terms may be neglected are many, so the most common form of the continuity equation (2.3) is that where $\mathcal{P} = \mathcal{S} = 0$.

An expression for the mean velocity $\mathbf{U}$ is obtained from Newton's second law for gases,

$$\rho\left(\frac{\partial \mathbf{U}}{\partial t} + (\mathbf{U}\cdot\nabla)\mathbf{U}\right) = n\mathbf{F} - \nabla p\,, \tag{2.4}$$

where $\rho = mn$ is the mass density of the plasma, $\mathbf{F}$ is a force field acting on the plasma and p is the pressure. A complete solution is obtained given an expression for the force field $\mathbf{F}$ and an equation of state $p = p(\rho)$. Unlike neutral gases and liquids, the dominant forces acting on the plasma are electric and magnetic forces, their collective influence on the plasma particles is given by the Lorentz force

$$\mathbf{F} = q\left(\mathbf{E} + \mathbf{U}\times\mathbf{B}\right)\,, \tag{2.5}$$

where q is the electric charge of the plasma particles. Here, $\mathbf{F}$ is understood as the force acting on a charged particle moving with the average flow velocity $\mathbf{U}$. Electric and magnetic fields can both be generated externally by some global mechanism and internally from perturbations in the plasma. Thus, to obtain a complete expression for the Lorentz force, a set of equations describing the dynamics of electric and magnetic fields is required.

2.3 Maxwell's equations

The theory of electromagnetism, through Maxwell's equations, describe the interconnected dynamics of electric and magnetic fields and their response to space-charges and currents in the plasma (Pécseli, 2013; Chen, 1984). Maxwell's equations are:
Poisson's equation

$$\nabla\cdot\mathbf{E} = \frac{\rho_e}{\varepsilon_0}\,, \tag{2.6}$$

Gauss law for magnetism

$$\nabla\cdot\mathbf{B} = 0\,, \tag{2.7}$$

Faraday's law of induction

$$\nabla\times\mathbf{E} = -\frac{\partial\mathbf{B}}{\partial t} \tag{2.8}$$

and Ampere's law including Maxwell's displacement current

$$\nabla\times\mathbf{B} = \mu_0\left(\mathbf{j} + \varepsilon_0\frac{\partial\mathbf{E}}{\partial t}\right)\,, \tag{2.9}$$

where ε_0 and μ_0 are the electric permittivity and magnetic permeability of free space, respectively. Expressions for charge density ρ_e and plasma current $\mathbf{j}$ are necessary in order to obtain complete solutions of the above equations. Assuming the plasma consist of electrons and singly charged (positive) ions, simple expressions for charge density and plasma current are constructed from the number densities n_e and n_i, velocities $\mathbf{U}_e$ and $\mathbf{U}_i$ and charge $q_e = -e$ and $q_i = e$:

$$\rho_e = e(n_i - n_e) \quad \text{and} \quad \mathbf{j} = e(n_i\mathbf{U}_i - n_e\mathbf{U}_e)\,.$$

Generalising these expressions to plasmas of any number of species s, where arbitrary values of each species charge q_s, number density n_s and mean velocity $\mathbf{U}_s$ are known, gives

$$\rho_e = \sum_s q_s n_s \quad \text{and} \quad \mathbf{j} = \sum_s q_s n_s \mathbf{U}_s \, .$$

A continuity equation of charge density ρ_e and the plasma current $\mathbf{j}$ can be found from the continuity equation of number density and flow (2.3),

$$\frac{\partial \rho_e}{\partial t} + \nabla \cdot \mathbf{j} = 0 \, , \tag{2.10}$$

which in itself is an equally important requirement for the plasma dynamics, and a helpful addition to the set of equations. One application demonstrated in section 3.3, where field solvers in Particle-in-Cell methods are discussed, is obtained by inserting (2.3) into Poisson's equation (2.6), thus eliminating the charge density ρ_e. This offers to rationalize the field solvers as the charge density ρ_e is implicitly found from accumulating the plasma current $\mathbf{j}$.

It is helpful to introduce the scalar and vector potentials, ϕ and $\mathbf{A}$, defined through

$$\mathbf{B} = \nabla \times \mathbf{A} \quad \text{and} \quad \mathbf{E} = -\nabla\phi - \frac{\partial \mathbf{A}}{\partial t} \, . \tag{2.11}$$

A separate class of problems exist in plasma physics known as the *electrostatic approximation* where the vector potential is nearly stationary, $\partial \mathbf{A}/\partial t \approx 0$. Inserting this condition into Faraday's law of induction (2.8) yields the trivial solution of a curl-free electric field, $\nabla \times \mathbf{E} = 0$. Taking the time derivative of Amperes law (2.9), and inserting expressions for $\mathbf{E}$ and $\mathbf{B}$ from the electrostatic approximation, it is found that any temporal variation in the plasma current $\partial \mathbf{j}/\partial t$ due to internally induced plasma dynamics is balanced by the time derivative of Maxwell's displacement current, $\varepsilon_0 \partial^2 \mathbf{E}/\partial t^2$. The only equation left to solve in order to obtain a complete solution of the fields is then Poisson's equation (2.6), which in the electrostatic approximation takes the form

$$\nabla^2 \phi = -\frac{\rho_e}{\varepsilon_0} \, . \tag{2.12}$$

The electrostatic approximation allows for direct solutions of several interesting problems in plasma physics, some of these are touched upon in this thesis and parts of the numerical simulations performed are based upon this approach.

2.4 Magnetohydrodynamics

The set of equations presented so far: the continuity equation (2.3), Newton's second law (2.4), an equation of state $p = p(\rho)$ (e.g. ideal gas law) and Maxwell's equations (2.6)-(2.9), when solved self-consistently, is generally referred to as *Magnetohydrodynamics* (MHD). MHD in its common form is a one fluid models, where the relative motion between electrons and ions is accounted for by Ampere's law (2.9). It is generally assumed that $\mathbf{j} \times \mathbf{B}$ dominate electric forces, so the latter are usually ignored. MHD is valid for large scale, slowly evolving systems, where the velocity distributions are assumed to be local shifted Maxwellians at all times. This restriction allows an approximation where Maxwell's displacement current in (2.9) is ignored in

comparison to the plasma current $\mathbf{j}$. Such problems are often referred to as macroscopic (Chen, 1984; Pécseli, 2013).

Collisions may also be included into the MHD equations, e.g. through sink/source terms in the continuity equation (2.3) or terms representing momentum transfer between plasma species in Newtons 2nd law for gases (2.4). The actual form of such terms will depend on the type of collision processes examined.

Since the problems addressed in this thesis are concerned with phenomena on microscopic scales, i.e. evolving on electron timescales and where velocity distributions are not expected to be Maxwellian, MHD will not be described further here.

2.5 Plasma kinetic theory

While classical fluid and gas dynamics assume local shifted Maxwellian distribution functions, *plasma kinetic theory* aims to establish the velocity distributions $f(\mathbf{x}, \mathbf{u}, t)$ of the particles as functions of independent variables for space, time and here also velocity. The plasma dynamics is found from evolving the distribution functions f, one for each plasma specie, with *the Vlasov equation*

$$\frac{\partial}{\partial t} f + \mathbf{u} \cdot \nabla f + \frac{1}{m} \mathbf{F} \cdot \nabla_{\mathbf{u}} f = 0 \,, \tag{2.13}$$

which is a continuity equation of f in a 6 dimensional phase space (3 in configuration, 3 in velocity) and time, and the distribution functions f are considered actual distributions of the plasma particles in volume elements $d\mathbf{x}d\mathbf{u} = dxdydzdu_x du_y du_z$. In the Vlasov equation (2.13, $\mathbf{F}$ is a force field by which the plasma is influenced, i.e. the Lorentz force (2.5), rewritten here for a microscopic description

$$\mathbf{F} = q\left(\mathbf{E} + \mathbf{u} \times \mathbf{B}\right) \,, \tag{2.14}$$

where $\mathbf{u}$ is the independent velocity variable and not the mean velocity $\mathbf{U}$ as before. The m in (2.13) is the mass of the plasma particles. The vector operator $\nabla_{\mathbf{u}}$ represents partial derivation with respect to velocity, $\nabla_{\mathbf{u}} = \{\partial/\partial u_x, \partial/\partial u_y, \partial/\partial u_z\}$.

The macroscopic quantities introduced in fluid theory, section 2.4, can be devised from plasma kinetic theory by integrating f over velocity space, i.e.

$$n = \int f d\mathbf{u} \quad \text{and} \quad \mathbf{U} = \langle \mathbf{u} \rangle = \frac{1}{n} \int \mathbf{u} f d\mathbf{u} \,,$$

where $\int d\mathbf{u}$ is a short hand notation for the triple integral $\int_{-\infty}^{\infty}\int_{-\infty}^{\infty}\int_{-\infty}^{\infty} du_x du_y du_z$. Similarly, by integrating the Vlasov equation (2.13) and assuming local (shifted) Maxwellian distribution functions, the continuity equation (2.3) and Newton's second law (2.4) from section 2.4 are obtained by some additional approximations. Charge density and plasma current are found from the integrals

$$\rho_e = \sum_s \int q_s f_s d\mathbf{u} \quad \text{and} \quad \mathbf{j} = \sum_s \int \mathbf{u} q_s f_s d\mathbf{u} \,, \tag{2.15}$$

where the sum is taken of the contributions from the involved plasma species s.

Formally, there exist a limit where the Vlasov equation becomes exact: the *Vlasov limit*. Each particle is subdivided such that the particles charge q_s and mass m_s tend to zero, in

such a way that in the limit where each species density $n_s \to \infty$, we get $q_s n_s \to const$ and $m_s n_s \to const$ and that the charge to mass ratios m_s/q_s remain constant. In this limit, the plasma parameter (2.2) $N_p \to \infty$. Kinetic plasma models can account for relative motions of charged particles, electrons and ions in particular, on a microscopic level. Kinetic models are also capable of describing interactions between particles and propagating waves.

2.6 Collisions in plasmas

For realistic conditions, plasmas often exhibit various forms of collisions, e.g. Coulomb scattering and charge exchange collisions. Collisional processes are often described by the mean free path ℓ_c and mean free time τ_c of the various mechanisms. These are especially helpful when deciding whether a plasma is collisional or not, through comparing them to the characteristic length λ_p and time scales τ_p of the plasma: Plasmas are considered collisional if the mean free path and mean free time are less or comparable to the plasma characteristic scales, i.e. when $\ell_c \lesssim \lambda_p$ and $\tau_c \lesssim \tau_p$, while the opposite is true when $\tau_c \gg \tau_p$ and $\ell_c \gg \lambda_p$. Examples of plasmas where either of these conditions are satisfied are 1) the Solar wind, where the studied phenomena occurring inside the Sun-Earth system while the mean free path is at the order of astronomical units[1], and 2) in the lower Earth's ionosphere where precipitating particles from higher altitudes collide with neutral and ionized gases in the high altitude atmosphere.

In the problems relevant for this thesis, collisions between particles belonging to the same plasma species are ignored, as they do not lead to any transport or exchange of momentum (or loss/production of particles) between the plasma components.

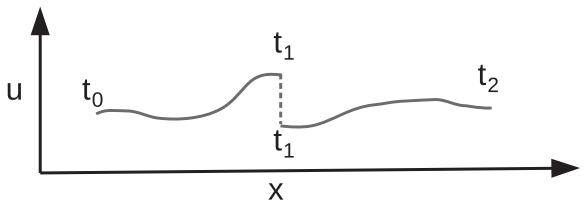

Figure 2.2: A phase space trajectory of a particle colliding at time t_1, resulting in a discontinuous phase space trajectory.

The Vlasov equation (2.13) describe an *incompressible* flow of the distribution functions f in phase space, which is another way of saying that the plasma is *collisionless*. Introducing a non-zero collisional operator

$$\left.\frac{\partial f}{\partial t}\right|_{coll} \neq 0 \,,$$

on the right hand side of (2.13) breaks with the restriction of incompressible flow as particles are allowed to move discontinuously from one volume element $d\mathbf{x}d\mathbf{u}$ to another. Figure 2.2 illustrate such a phase space trajectory, where the velocity of the particles changes abruptly

[1] 1 astronomical unit $= 1AU \approx 150\,000\,000$km

at time t_1. Note that the particle does not change it's position, which would violate the basic concept of collisions.

2.7 Waves and oscillations in plasmas

Waves and oscillations in plasmas are commonly described as the exchange of energy between different states; kinetic energy of the plasma particles, $mnu^2/2$, magnetic field energy $B^2/2\mu_0$ and electric field energy $\varepsilon_0 E^2/2$. Figure 2.3 illustrate this schematically, where e.g. electrostatic waves are associated with an exchange of kinetic and electric field energy, electromagnetic radiation is associated with exchange of electric and magnetic field energy, or the more general waves modes often found in plasmas where energy is exchanged between all three states. The figure is best understood when applied to standing waves. Waves in plasmas is an important feature of the phenomena studied in this thesis, so to give the reader a basic understanding of these, some instructive examples of plasma waves are given in this section. Furthermore, several quantities introduced in these examples are used as normalization quantities of the results. To understand the results correctly, a basic knowledge of these examples is required.

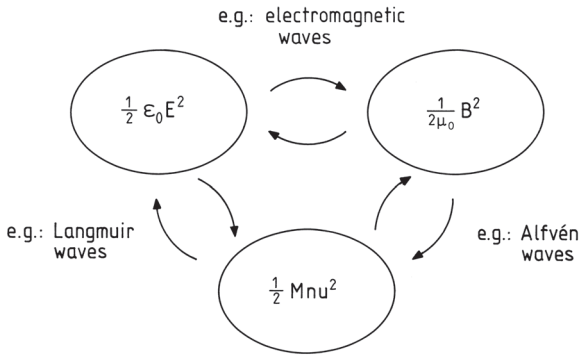

Figure 2.3: Illustration of characteristics of different wave-types in plasmas. Figure reproduced from Pécseli (2013).

Electrostatic

Consider a plasma where the ions are assumed to be immobile, fields are electrostatic and the plasma is cold, $T \to 0$. Perturbing the plasma from the equilibrium state by displacing the electrons slightly, a restoring electric force will cause the electrons to oscillate with the *plasma frequency*

$$\omega_{pe} = \sqrt{\frac{q_e^2 n_e}{\varepsilon_0 m_e}}\,, \tag{2.16}$$

where $q_e = -e$, m_e and n_e are the electrons charge, mass and number density, respectively.

Introducing a finite temperature $T > 0$, thus allowing the pressure forces to act along side the electric forces in restoring the perturbations with comparable influence, the electron plasma

frequency give rise to propagating wave modes. These waves are commonly known as *Langmuir waves*, and their dispersion relation is given by the *Bohm-Gross relation*,

$$\omega^2 = \omega_{pe}^2 + 3k^2 u_{th,e}^2 \,, \tag{2.17}$$

where $u_{th,e} = \sqrt{k_B T/m_e}$ is the thermal velocity of electrons. Note how the Bohm-Gross relation (2.17) reduce to the electron plasma frequency (2.16) for all wave numbers k when $T \to 0$.

Similar oscillations and propagating wave modes are found for the ions, when these are assumed mobile. In the simplest approximation with mobile ions, electrons are considered a mass-less, neutralising fluid ($m_e \to 0$), with the result that the electrons follow a Boltzmann distribution in an electrostatic potential ϕ,

$$n_e = n_0 \exp\left(\frac{e\phi}{k_B T}\right) \,. \tag{2.18}$$

A similar expression is thus obtained for the *ion plasma frequency*,

$$\omega_{pi} = \sqrt{\frac{q_i^2 n_i}{\varepsilon_0 m_i}} \ll \omega_{pe} \,. \tag{2.19}$$

Introducing a finite temperature for the electrons and ions, acoustic waves can propagate in the plasma through the intermediary of electric fields. Again, the electrons are assumed Boltzmann distributed (2.18), and through linear analysis, the dispersion relation for *ion acoustic waves* is obtained,

$$\omega^2 = C_s^2 k^2 \,, \tag{2.20}$$

where $C_s = \sqrt{k_B T/m_i}$ is the speed of sound in the plasma. Note that ion acoustic waves can propagate by the electron pressure alone, i.e. if $T_e > 0$, even though $T_i = 0$.

Electromagnetic

The discussion on waves and oscillations in plasmas so far have only dealt with electrostatic modes. The more general electromagnetic case contains several interesting wave modes, only two classes of which will be discussed here: Electromagnetic radiation (light waves) and Alfvén waves (Pécseli, 2013). Solving Maxwell's equation for a vacuum yields the standard text book result of electromagnetic waves with the dispersion relation

$$\omega^2 = c^2 k^2 \,, \tag{2.21}$$

where $c = 1/\sqrt{\varepsilon_0 \mu_0}$ is the speed of light. When propagating in a plasma, light waves couple with the electron plasma frequency (2.16) at low wave numbers k, giving the modified dispersion relation for light waves in plasmas

$$\omega^2 = \omega_{pe}^2 + c^2 k^2 \,. \tag{2.22}$$

Alfvén waves are low frequency waves of the ions and magnetic field, where the ions give

the waves inertia while the magnetic field $\mathbf{B}$ acts as the restoring force. Classical *Alfvén waves* are formed when the plasma flow is incompressible, $\nabla \cdot \mathbf{u} = 0$. Shear Alfvén waves may propagate also at oblique angels relative to $\mathbf{B}$, their the dispersion relation given by

$$\omega^2 = V_A^2 k^2 \cos^2\theta \,, \tag{2.23}$$

where $V_A = B/\sqrt{2\mu_0}$ is the Alfvén velocity and θ is the angle between $\mathbf{k}$ and $\mathbf{B}$, so that $\theta = 0$ corresponds to the incompressible Alfvén waves propagating along $\mathbf{B}$. *Compressible Alfvén waves* arise where the flow no longer is divergence free, $\nabla \cdot \mathbf{u} \neq 0$, and they include ion acoustic waves (2.20) as a special limit. Given an equation of state $p = p(\rho)$, the dispersion relation is obtained for these wave modes from linear analysis,

$$\frac{\omega^2}{k^2} = \frac{1}{2}(C_s^2 + V_A^2) \pm \frac{1}{2}\sqrt{(C_s^2 + V_A^2)^2 - 4C_s^2 V_A^2 \cos^2\theta} \,, \tag{2.24}$$

where C_s, V_A and θ have the same definitions as given earlier.

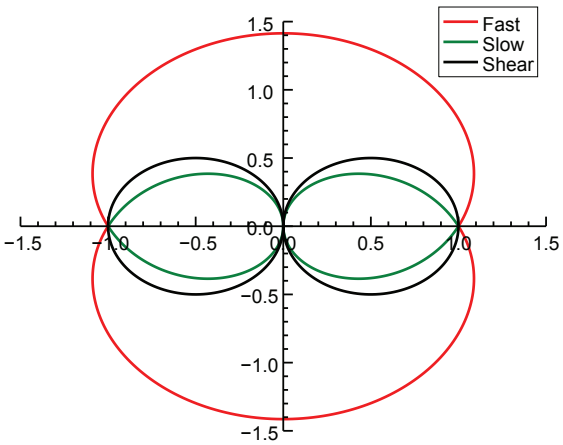

Figure 2.4: Phase velocity ω/k of fast (red) and slow (green) magnetosonic waves (2.24) and shear Alfvén waves (black) (2.23) as function of the angle θ between $\mathbf{k}$ and $\mathbf{B}$. Phase velocities are normalized to the Alfvén speed V_A, where $C_s = V_A$ in the current example.

These waves are known as *magnetosonic waves*, since they are combinations of sound waves and incompressible Alfvén waves. Their combined velocity, $\sqrt{C_s^2 + V_A^2}$ is similarly known as the *magnetosonic speed*. Two solutions exist for any non-zero values of C_s and V_A, depending on the choice of sign in (2.24), known as *fast* (+) and *slow* (-) magnetosonic waves. The phase velocity ω/k of fast and slow magnetosonic waves, and phase velocity ω/k of the shear Alfvén waves (2.23), are plotted as function of the angle of propagation θ in Figure 2.4. By formally allowing $V_A \to 0$, ion acoustic waves (2.20) is obtained at all θ.

It is interesting to note that for waves propagating parallel to the magnetic field, i.e. when $\theta = 0$ or π, magnetosonic and shear Alfvén waves collapse to give the dispersion relation for incompressible Alfvén waves with $(\omega/k)^2 = V_A^2$. In the opposite case, when waves are propa-

gating strictly perpendicular to the magnetic field, i.e. $\theta = \pi/2$ or $3\pi/2$, only fast magnetosonic waves persist.

2.8 Applications

The contexts in which the results of this thesis are interpreted divide into two categories presented in this section. One case relates to Q-machine experiments, the other to astrophysical shocks. Although they may appear unrelated from an outside perspective, when viewed as manifestations of basic plasma phenomena suitable for in-depth numerical studies by use of Particle-in-Cell methods, where these methods offer new insight into the phenomena, their relevance to each other becomes more obvious.

Q-machine experiments

Q-machines consist of a vacuum vessel in which plasma is produced by surface or contact ionisation on a hot metallic plate. The plasma is confined by a strong axial magnetic field, and in its standard version illustrated in Figure 2.5, is single ended, bounded by a cathode and an anode (Motley, 1975). The Q-machines was originally built to investigate Landau damping (Wong et al., 1964) of ion acoustic waves due to the quiet qualities of the machines. It was also found that Q-machines excelled in experiments with low frequency electrostatic waves in magnetised plasmas in general (Hendel et al., 1968; Schlitt and Hendel, 1972). Perhaps the most relevant results from the Q-machines today, are those obtained on anomalous transport (Simonen et al., 1970; Iizuka and Schrittwieser, 1993) with application to e.g. plasma fusion devices (Liewer, 1985).

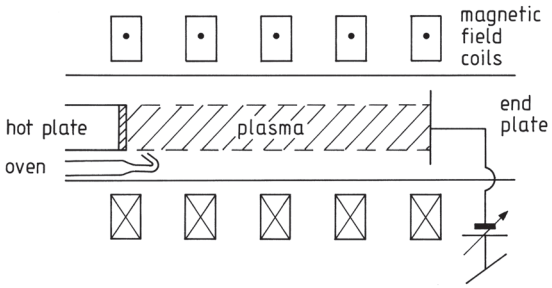

Figure 2.5: Schematic representation of a Q-machine. Figure reproduced from (Pécseli, 2013).

Q-machines, like any other experimental devices, suffer from natural limitations in the diagnostics available. Spatial and temporal resolution was limited and probes are known to affect the plasma. Revisiting these problems with kinetic simulations, from which high resolution phase space diagnostics are available, new insight is given to classical problems in plasma physics without the use of intrusive diagnostics.

Particle acceleration in astrophysical shocks

Supernova remnants (SNR) are structures in space resulting from the explosions of a stars in supernovae. It consists of ejecta material from the explosion and is generally found to contain shock waves (Koyama et al., 1995; Enomoto et. al., 2002). SNRs, e.g. as in Figure 2.6, are considered to be the major source of galactic cosmic rays (Plaga, 2008), in which plasma shock waves are believed to be responsible for the pre-acceleration mechanisms. Quasi-perpendicular shocks, a class of shocks often found in SNRs, at the Heliopause and at the Earth's bow shock, are able to accelerate ions to supra-thermal energies, allowing further acceleration to cosmic ray energies through the second order Fermi processes (Fermi, 1949; Bell, 1978; Blandford and Ostriker, 1978).

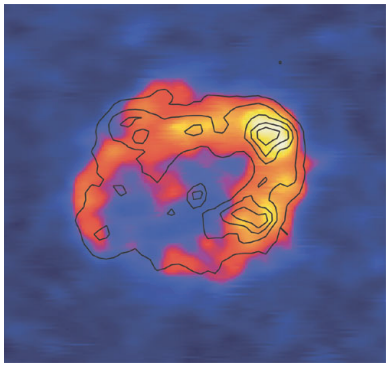

Figure 2.6: The shell of supernova remnant SNR XR J$1713.7 - 3946$*, a candidate source of cosmic rays. Figure reproduced from Aharonian et al. (2007).*

Observations of cosmic rays originating in SNRs show only the bulk properties of the accelerated ions at late times, giving no direct evidence to the underlying mechanisms. Fully self-consistent numerical simulations of these shocks offer insight into these mechanisms, where the plasma conditions of SNRs are used as input parameters in the numerical model. Particle-in-Cell simulations of shocks in electron-proton plasmas (Lembege and Savoini, 1992; Schmitz et al., 2002; Scholer et al., 2003; Shimada and Hoshino, 2000; Lee et al., 2004) have shown that these shocks are reforming at the spatiotemporal scales of the protons, facilitating ion acceleration at the shock front and in the downstream turbulent fields. Since only a part of the particles are accelerated to significant velocities, a traditional fluid model is not applicable for describing these phenomena: only kinetic models contain sufficient details.

The self-consistent inclusion of heavy ion species in Particle-in-Cell models by Chapman et al. (2005) have shown that the shock dynamics and acceleration mechanisms depend strongly on the relative ion densities. At relatively low heavy ion densities, $\sim 25\%$ with respect to the total ion density, a cross over occurred to a shock dominated by the heavy ions, and that ion energisation through the shock was enhanced considerably for these intermediate ion densities.

Chapter 3

Numerical Simulations

Plasma phenomena are intricate in their nature, and both theoretical analysis and experimental diagnostics suffer from limitations in the methods. While theoretical analysis often assume linearised models or a simplified geometry to address the problem, experiments suffer from limitations in diagnostics and that each probe or measurement affects the plasma in some degree. Numerical simulations provide a bridge between the limitations in theoretical models and shortage of unbiased diagnostics in experiments (Tang and Chan, 2005).

Commonly, there are two classes of numerical methods used in plasma physics, based on the theoretical frameworks discussed in sections 2.4 and 2.5; fluid and kinetic models. Kinetic models excel at short-scale, rapidly evolving systems as they resolve scale lengths down to the Debye length (2.1) and times less than the electron plasma frequency (2.16), not to mention allowing for non-Maxwellian velocity distributions. Fluid models can handle much larger systems and complex geometries with low computational cost compared to the kinetic approach, but at the cost of spatial resolution and restricting to slowly evolving phenomena in which velocity distributions quickly relaxes to Maxwellian distributions if perturbed. A third class exist, where kinetic and fluid descriptions are combined into *hybrid* models. Here, ions may be treated kinetically while electrons are assumed a mass-less neutralising fluid, thus bridging the gap between kinetic and fluid models with respect to computational load and spatio-temporal resolution.

The numerical methods used in this thesis are Particle-in-Cell methods which are derived from kinetic theory. Section 3.1 introduce the general properties of Particle-in-Cell, while sections 3.2 and 3.3 discuss details of the particle orbit integration schemes and field solvers used in this thesis. Emphasis is put on the implementation of open boundaries, in section 3.4, and binary collisions, in section 3.5, thus raising these as two of the most important contributions to plasma numerical simulations of this thesis.

3.1 Particle-in-Cell

In PIC methods, the distribution functions introduced in kinetic theory, section 2.5, are represented as a collection of numerical 'super-particles', each described by individual positions, velocities, mass and charge. The operations performed during each time step is as follows: Plasma current $\mathbf{j}$ and charge density ρ_e are calculated from the positions and velocities of the

particles on a spatial grid using (2.15). Maxwell's equations (2.6)-(2.9) are solved, giving expressions of the fields as funcions of the spatial coordinate only. The Lorentz force (2.14) calculated from these fields for each particle, where a mapping of the force is performed from the spatial grid to the particles. Their velocities and positions are then updated for the next time step (Birdsall and Langdon, 1985). Schematics of the time cycle of the PIC methods is shown in Figure 3.1.

PIC methods excel in the sense that while resolving electron time scales, they do so at a lower computational cost than the direct approach of e.g. molecular dynamics. In the latter, the interaction between particles is calculated for an ensemble of $\mathcal{N}$ particles, requiring $\sim \mathcal{N}^2$ operations every time step. The short hand notation for this is order $\mathcal{O}(\mathcal{N}^2)$. Even for moderate values of $\mathcal{N}$, the number of operations required to solve for the full plasma dynamics gets too large for large computers nowadays (Klimontovich, 1967). PIC methods avoid this problem by mapping the particles charge and current contributions onto a spatial grid of $\mathcal{N}_g$ cells, an algorithm of order $\mathcal{O}(\mathcal{N})$, then solving for the fields on the spatial grid which require operations of the order $\mathcal{O}(\mathcal{N}_g \log \mathcal{N}_g)$. The total computational load of PIC is therefore $\mathcal{O}(\mathcal{N} + \mathcal{N}_g \log \mathcal{N}_g)$ which is much less than $\mathcal{O}(\mathcal{N}^2)$, given that $\mathcal{N}_g \ll \mathcal{N}$.

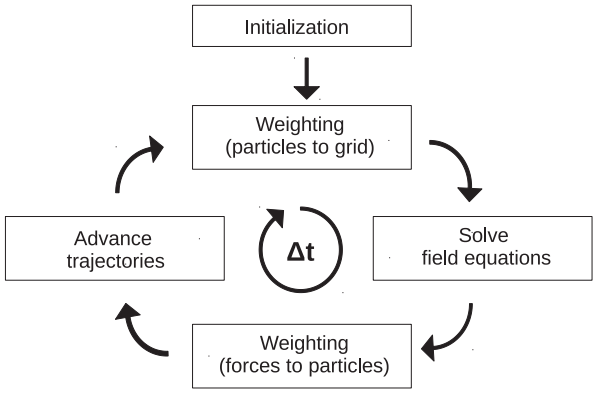

Figure 3.1: The basic scheme of the particle-in-cell time cycle.

Further rationalization is achieved in PIC methods by representing real particles with computational 'super-particles', where one computational particle represents several real particles. This transformation of the particles 'weight' is valid as long as the charge-to-mass ratios of the particles, and the weighted charge and mass densities of each species s remain unchanged, i.e. $n_s m_s = const$ and $n_s q_s = const$. Inherently, PIC methods are only valid when the real particles exhibit collective dynamics on the scale of super-particles, which from the arguments given in section 2.1 is achieved when the plasma parameter (2.2) N_p is large.

The accuracy of PIC methods depends most of all on the number of computational particles per grid cell, $\mathcal{N}_{\text{cell}} \equiv \mathcal{N}/\mathcal{N}_g$, where the signal-to-noise ratio (SNR) of the field solver scale with $\mathcal{N}_{\text{cell}}^{-1/2}$. Instead of simply increasing $\mathcal{N}_{\text{cell}}$ to achieve better SNR, which would also increase the computational load equally, particles are assigned finite size charge distributions on the grid. This ensures a smooth mapping of each particles charge onto the grid, and a weighted mapping of the Lorentz force from several grid cells onto each particle. The finite size distributions,

known as *shape functions*, come in various shapes and sizes depending on the problems studied. A popular compromise between relatively low SNR and complexity applicable to many plasma phenomena involves triangular shape functions spanning $2-3$ grid cells simultaneously, and with $\mathcal{N}_{\text{cell}} \sim 100$. Higher accuracy is required when considering e.g. relativistic plasmas and in the field of quantum electron dynamics, where higher order and wider shape functions are required (see e.g. Haugbølle et al. (2013)).

It is important that PIC methods resolve the Debye length (2.1), $\Delta x \lesssim \lambda_D$, otherwise the plasma will experience artificial heating, effectively increasing the Debye length of the plasma until $\lambda_D \approx \Delta x$ (Birdsall and Langdon, 1985). The temporal resolution is limited by the Courant-Levy-Friedrich condition (Courant et al., 1928), requiring that no particles travel more than the size of one grid cell during the integration time step Δt, i.e. $\Delta t < \Delta x/u_{max}$.

Two PIC codes have been used in this thesis, an electrostatic and an electromagnetic code. The electrostatic PIC code was developed by the author for his Master's degree (Rekaa, 2009) and is a one dimensional code where only the parallel component of the electric field, together with all three velocity components of the particles are evolved in time as functions of one spatial coordinate. The electromagnetic code[1] is developed and maintained by staff at the Centre for Fusion, Space and Astrophysics at the University of Warwick, U.K., and is a relativistic, one dimensional code, where all three field and velocity components are evolved in time as functions of one spatial coordinate.

3.2 Particle orbit integration

There are several particle orbit integration schemes available to PIC codes, e.g. Euler's method, Leapfrog, Predictor-Corrector and Runge-Kutta's 2nd and 4th order methods, just to mention a few. The by far most common in PIC codes, which is also used in the PIC codes of this thesis, is the Leapfrog algorithm. In this method, velocities $\mathbf{u}$ are evaluated at the mid time steps $(i \pm 1/2)\Delta t$ while positions $\mathbf{x}$ and accelerations $\mathbf{a}$ are evaluated at the whole time steps $i\Delta t$, giving the full set of discretized equations for the particle motion,

$$\mathbf{a}_i = \mathbf{F}(\mathbf{x}_i)/m \ , \tag{3.1}$$

$$\mathbf{u}_{i+1/2} = \mathbf{u}_{i-1/2} + \mathbf{a}_i \Delta t \ , \tag{3.2}$$

$$\mathbf{x}_{i+1} = \mathbf{x}_i + \mathbf{u}_{i+1/2} \Delta t \ . \tag{3.3}$$

The popularity of the Leapfrog method comes from the fact that it integrates the particle orbits to second order accuracy with 1st order equations. Higher order methods like the Predictor-Corrector method is preferred when higher accuracy is needed.

Boundary conditions

Boundary conditions on particles describe how particles leaving or entering the spatial domain are treated. The simplest cases are periodic and reflecting boundaries, where in many cases, the mathematical description of the boundaries becomes exact. In periodic boundaries, any

[1] EPOCH: $http://ccpforge.cse.rl.ac.uk/gf/project/epoch/$

particle leaving the domain is re-injected with identical parameters (e.g. velocity, charge, mass) through the opposite domain boundary. Reflecting boundaries on the other hand, re-inject any particle leaving the domain at the same boundary but with reversed velocity component normal to the boundary surface. Open boundaries, where particles are allowed to leave the domain (and from the simulations all together) and also where new particles may be injected from an assumed plasma source are generally more complex. Further details of open boundaries and the implementation of these are given in section 3.4.

3.3 Field solvers

To find expressions for the acceleration $\mathbf{a}$ introduced in section 3.2, self-consistent solutions of Maxwell's equations (2.6)-(2.9) are obtained from the charge density ρ_e and plasma current $\mathbf{j}$, given by the particles positions and velocities in the orbit integration scheme. The available techniques for solving Maxwell's equations in PIC codes fall into two categories: electrostatic and electromagnetic field solvers. Instead of discussing all the available field solvers in general, the two techniques used in the PIC codes of this thesis, respectively, are presented, and their properties discussed.

Electrostatic

The electrostatic code solves Poisson's equation (2.12) for the scalar potential ϕ,

$$\nabla^2 \phi_i = -\frac{\rho_{e,i}}{\varepsilon_0} \,, \tag{3.4}$$

at each time step i, and the Lorentz force is given by $\mathbf{F}_i = -q\nabla\phi_i$. Solving Poisson's equation (3.4) requires an iterative approach, where the right hand side ρ_e/ε_0 is known. Given suitable boundary conditions for the electrostatic field ϕ_i, complete solutions are obtained. While the Gauss-Seidel and Red-Black schemes are the two most common approaches for solving (3.4) numerically, the preferred scheme in the current thesis is the Multi-Grid method (Hackbusch, 1985) due to it's efficiency compared to other iterative approaches.

Electromagnetic

The electromagnetic PIC code solves the continuity equation for charge density ρ_e and plasma current $\mathbf{j}$ (2.10) inserted into Poisson's equation (2.6) to obtain a solution for the electric field, where instead of calculating ρ_e explicitly, it is implicitly found from the accumulation of $\nabla \cdot \mathbf{j}$ over time. The time discretized equation for the electric field is thus

$$\mathbf{E}_{i+1} = \mathbf{E}_i + \frac{\Delta t}{\varepsilon_0}\mathbf{j}_{i+1/2} \tag{3.5}$$

calculated at each time step i. The time discretized equation for the magnetic field is found from Faraday's law of induction (2.8),

$$\mathbf{B}_{i+1/2} = \mathbf{B}_{i-1/2} - \Delta t \nabla \times \mathbf{E}_i \,. \tag{3.6}$$

Since both the electric and magnetic fields contribute to the Lorentz force $\mathbf{F}$ (2.14), the force now depends on the positions $\mathbf{x}$ as well as the velocities $\mathbf{u}$ of the particles. Note that plasma current $\mathbf{j}$ and magnetic field $\mathbf{B}$ are calculated at the mid time steps $t = (i \pm 1/2)\Delta t$, from similar arguments as for the Leapfrog method.

The discretized equations used to solve for the electric field in the electromagnetic code (3.5) have the advantage of being quicker than the direct solution of Poisson's equation (3.4) used in the electrostatic code. However, as the plasma current is accumulated over time, this approach is sensitive to systematic errors in the algorithms from which $\mathbf{j}$ is calculated, especially at the boundaries where the mapping of particle contributions gets more complicated. Even small deviations $\delta\mathbf{j}$ from the expected value $\mathbf{j}_0$ give rise to artificial electric fields if the mean value of $\delta\mathbf{j}$ is non-zero, $\langle\delta\mathbf{j}\rangle \neq 0$.

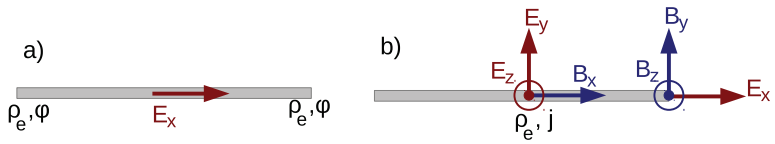

Figure 3.2: Schematics of a staggered grid cell in the electrostatic code (a) and the electromagnetic code (b) along one spatial dimension x. Arrows and letters indicate where the respective quantities and field components are calculated.

Additional accuracy of the field solvers is achieved by introducing staggered grids, that the quantities entering the field solvers are calculated at shifted positions relative to each other. Figure 3.2 illustrate the staggered grid cells of the electrostatic and electromagnetic PIC codes, where the latter is recognized as a Yee-grid in one spatial dimension (Yee, 1966). By shifting these locations relative to each other, higher order accuracy is obtained from the same arguments that allow the Leapfrog method to integrate the particle orbits (see section 3.2) to 2nd order accuracy with only 1st order equations.

Boundary conditions

Boundary conditions on the fields, i.e. where either the values of the fields or their derivatives are given at the boundaries, are required to obtain complete solutions of the field solvers. The choice of boundary conditions usually represent the physical conditions surrounding the simulated plasma, but also decides the context in which the plasma phenomena are studied. Boundary conditions may thus represent walls of a plasma vessel, cathodes, anodes, plasma reservoirs, vacuum, etc. The boundary conditions must be consistent with the state of the simulated plasma at all times to avoid sharp transitions of any quantity close to the boundary, and they must represent consistent solutions of Maxwell's equations.

3.4 Open particle boundaries

Open boundaries are commonly understood as boundaries where plasma is allowed to flow in and out of the simulation domain. The implementation of open boundaries is non-trivial as these generally involve several elements, all which must be implemented consistently with each other, the plasma conditions in the boundary region, boundary conditions on the fields, etc. The current section address two of these elements: 1) how particles with shape functions extending through a boundary surface are treated; and 2) how the velocity distributions are represented by random numbers in the simulations.

Particle shape functions at the boundary

Section 3.1 introduced the concept of shape functions, where particles are attributed finite size charge distributions, mapping their contributions to the grid (and fields from the grid back to the particles) over several grid cells simultaneously. The finite size of the particles implies that even though the particles (centroid) positions is clearly outside or inside the spatial domain, their shape functions may still extend through the boundary surface. Particles close to the boundary will contribute differently to the fields, since only parts of their shape functions overlap grid cells in the spatial domain. Similarly, the Lorentz force when mapped back to these particles will have reduced influence and may also be biased from these effects.

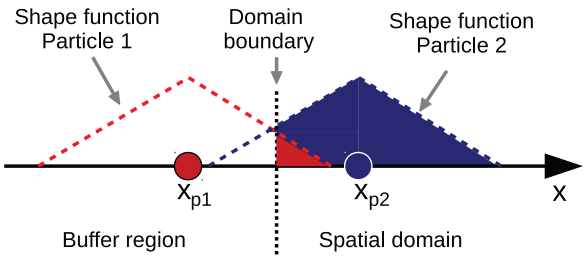

Figure 3.3: Illustration of two particles with shape functions extending through the domain boundary with centroid positions outside (x_{p1}) and inside (x_{p2}) the spatial domain. Their contributions to the field solvers are indicated by the coloured regions.

When considering particles leaving or entering the domain, their shape functions must to be taken into consideration before they enter and after they have left, otherwise abrupt changes in the charge density and plasma current at the boundary may cause unphysical contributions to the fields. One solution to this problem, which is used in the numerical simulations of this thesis, is to introduce a buffer region, in which particles reside as long as their shape functions extend into the spatial domain. Particle creation and removal may thus be done in the far end of the buffer region, where they give no contributions to the fields whatsoever. A 1D representation of a buffer region is given in Figure 3.3, together with two particles close to the boundary. The coloured regions indicate the fractions of the respective shape functions by which they contribute to the fields.

Also the fields in the buffer region must be treated separately. The simplest choice would be to simply extend the field boundary conditions into the buffer region. Other alternatives may involve absorbing boundary conditions, where any oscillations propagating into the buffer region is damped, thus allowing a smooth transitions between the plasma states of the simulated plasma and of the assumed conditions outside the buffer region. The same conditions that applies to field boundary conditions in general apply similarly here to the buffer regions: the fields in the buffer region must be self-consistent, consistent with the plasma conditions on both sides and represent consistent solutions of Maxwell's equation.

Velocity distributions of injected particles

Particle injection algorithms usually assume a plasma source for which the velocity distribution (VDF) $f(\mathbf{u})$ is known. The VDF of particles injected through a boundary surface from the plasma source is then

$$g_{\mathrm{u}}(u) = uf(u) \; , \tag{3.7}$$

where $\mathbf{n}_B$ is the normal vector of the boundary surface, and $u \equiv \mathbf{u}\cdot\mathbf{n}_B$ is the velocity component along $\mathbf{n}_B$. The particle flux through the boundary surface is found from the integral

$$\mathcal{F}_+ = \int_0^\infty uf(u)\, du \; ,$$

where the $+$-sign emphasize that only uni-directional flux is considered, and $f(\mathbf{u})$ is normalized so that $n = \int_{-\infty}^{\infty} f(\mathbf{u}) d\mathbf{u}$ is the number density of the plasma source. Since PIC methods represent the VDFs with particles, a method for generating random numbers from the VDF $g_{\mathrm{u}}(u)$ (3.7) is required. Therefore, a transformation of random variables is necessary to convert random numbers from a uniform distribution to random numbers representative of $g_{\mathrm{u}}(u)$.

The method of inverse transform sampling in statistics (the *inverse method*) offers such a transformation (Devroye, 1986; Trulsen, 2005). Consider first the case where a general probability distribution function (PDF) $g_{\mathrm{x}}(x)$ is given, with cumulative distribution function (CDF)

$$G_{\mathrm{x}}(x) = \int_a^x g_{\mathrm{x}}(x')\, dx' \; , \tag{3.8}$$

where $x \in [a, b]$ such that $\int_a^b g_{\mathrm{x}}(x)dx = 1$, and correspondingly an expression for y, $G_{\mathrm{y}}(y)$. The fundamental theorem of probability calculus gives that for corresponding values of x and y, the CDFs are equal, $G_{\mathrm{x}}(x) = G_{\mathrm{y}}(y)$. For strictly increasing $G_{\mathrm{y}}(y)$, the inverse function G_{x}^{-1} always exist, which can be used to obtain a solution of y,

$$y = G_{\mathrm{y}}^{-1}(G_{\mathrm{x}}(x)) \; . \tag{3.9}$$

Inserting $g_{\mathrm{u}}(u)$ (3.7) for $g_{\mathrm{y}}(y)$ and $g_{\mathrm{R}}(R)$ for $g_{\mathrm{x}}(x)$ into the transformation (3.9), where R is a random number drawn from a uniform distribution $R \in \mathrm{U}[0, 1]$ with CDF $G_{\mathrm{R}}(R) = R$, values are obtained for u from the transformation

$$u = G_{\mathrm{u}}^{-1}(G_{\mathrm{R}}(R)) = G_{\mathrm{u}}^{-1}(R) \; . \tag{3.10}$$

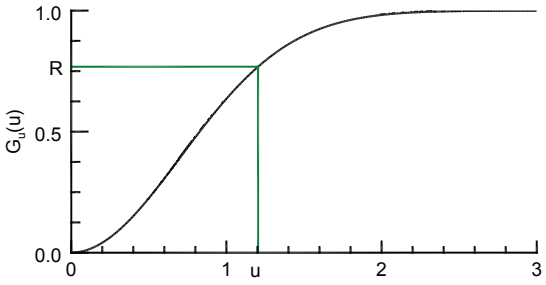

Figure 3.4: Mapping of a random uniform number $R \in [0,1]$ to a velocity u from the VDF $g_u(u)$ (3.7) via its CDF $G_u(u)$.

Figure 3.4 illustrates the transformation (3.10) where the VDF $f(\mathbf{u})$ that enters the expression for $g_{\mathrm{u}}(u)$ (3.7) is for the current example taken to be a centred Maxwellian and the velocity $u \in [-3,3]$ is in normalized units.

Analytical solutions of the inversion method, with several applications to numerical simulations of plasma physics, exists for two special cases: 1) when $g_{\mathrm{u}}(u)$ itself is a Maxwellian; and 2) when $f(u)$ that enters the expression for $g_{\mathrm{u}}(u)$ (3.7) is Maxwellian. In the first case, the analytical expressions is found through a conversion of two random variables (R_1, R_2) to polar form (R, θ), where $R^2 = R_1^2 + R_2^2$ and $\tan\theta = R_1/R_2$. A pair of random numbers (u, v) drawn from a Maxwellian distribution is obtained through the transformations

$$\begin{aligned} u =& R\cos\theta = \sqrt{-2\ln R_1}\cos(2\pi R_2)\ , \\ v =& R\sin\theta = \sqrt{-2\ln R_1}\sin(2\pi R_2)\ . \end{aligned}$$

In the second case, the analytical expression is trivially obtained since the CDF of $g_{\mathrm{u}}(u)$ is simply $G_{\mathrm{u}}(u) = 1 - \exp(-u^2)$, offering the direct transform

$$u = \sqrt{-\ln(1-R)} = \sqrt{-\ln(R)}$$

for a random number $R \in \mathrm{U}[0,1]$.

Although these analytical transforms are applicable to some of the problems studied in this thesis, the direct implementation of the transformation, given by (3.9) and Figure 3.4, is preferred to maintain generality of the codes.

3.5 Collisions

The collisional processes considered here are those where the plasma particles collide with neutral atoms uniformly distributed in space, stationary in time, and with a priori assumed velocity distributions. The available mechanisms are thus elastic or inelastic scattering of the plasma particles with the neutral atoms, or charge exchange collisions where an ion exchange an electron with the neutral gas atoms.Collisional processes are commonly described by the

cross section $\sigma(\mathcal{E})$, given as functions of the kinetic energy of the particle pairs

$$\mathcal{E} = \frac{1}{2}\left(\frac{m_1 m_2}{m_1 + m_2}\right)|\mathbf{u}_2 - \mathbf{u}_1|^2 = \frac{1}{2} m_R u_R^2 \,,$$

in the centre-of-mass frame of reference, where m_1, m_2 and $\mathbf{u}_1$, $\mathbf{u}_2$ are the respective particles mass and velocity in the laboratory frame of reference. The reduced mass m_R and relative velocity u_R are introduced for ease of notation. The collision frequency $\nu(\mathcal{E})$ is then given as

$$\nu(\mathcal{E}) = u_R n_n \sigma(\mathcal{E}) \tag{3.11}$$

where n_n is the number density of the neutral gas. The mean free time τ_c, introduced in section 2.6, is found by the taking inverse of the frequency, $\tau_c = \nu(\mathcal{E})^{-1}$.

The numerical treatment of binary collisions in PIC codes can be described in terms of solving two distinct problems: 1) selecting simulated particles for collisions; and 2) once selected, altering their velocity in correspondence with the collisional parameters given.

Selection by null-collisions

The numerical collision model developed for the present study is based on a Monte Carlo Collision (MCC) model for PIC codes and is directly based upon previous works (Vahedi and Surendra, 1995; Birdsall, 1991). Where traditional collision models calculate the time between collisions for each particle (McDaniel, 1989; McDaniel et al., 1993), the MCC-PIC package generalizes these calculations to allow for more efficient algorithms.

The collision algorithm is based on the null-collision methodology (Skullerud, 1968). Instead of entering the rather time-consuming evaluation of the cross section $\sigma(\mathcal{E})$ or equivalently the collision frequency $\nu(\mathcal{E})$ for each simulation particle at each time step, a maximum collision frequency ν_{max} is introduced for each particle specie,

$$\nu_{\text{max}} \equiv \max_{\mathcal{E}} \left(\sum_k \nu_k(\mathcal{E}) \right), \tag{3.12}$$

where $\nu_k(\mathcal{E})$ is the collision frequency of type k for the given specie. Potential candidates for collision events during the time interval Δt are now drawn with probability

$$P = 1 - \exp(-\nu_{\text{max}} \Delta t) \,.$$

For these candidates *only*, the exact evaluation of $\nu(\mathcal{E})$ is performed. A fraction $\nu(\mathcal{E})/\nu_{\text{max}}$ of the potential candidates drawn are then subjected to an actual collision event. The remaining fraction suffer a "null-collision", that is they avoid collisions in the given time interval Δt.

The evaluation of collision frequencies in the MCC-PIC package is illustrated in Figure 3.5 for two (fictive) collision mechanisms with frequencies $\nu_1(\mathcal{E})$ and $\nu_2(\mathcal{E})$. The sum of these $\sum_k \nu_k = \nu_1(\mathcal{E}) + \nu_2(\mathcal{E})$, is obtained and a null-event frequency $\nu_{\text{null}}(\mathcal{E})$ is constructed so that the sum $\nu_1(\mathcal{E}) + \nu_2(\mathcal{E}) + \nu_{\text{null}}(\mathcal{E})$ is constant for all $\mathcal{E}$ and equal to ν_{max} (3.12). The vertical

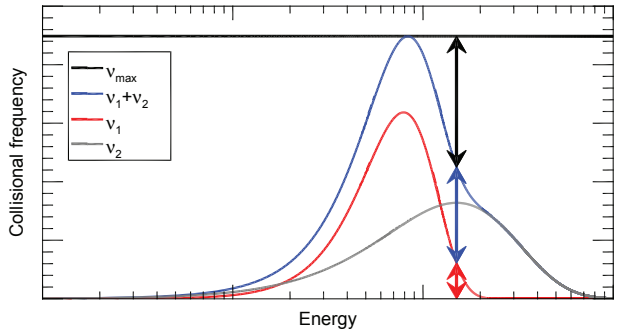

Figure 3.5: Collision frequency $\nu_1(\mathcal{E})$ in red and $\nu_2(\mathcal{E})$ in grey representing two collision processes acting on one plasma species. The sum of these $\nu_1(\mathcal{E}) + \nu_2(\mathcal{E})$ is given in blue and the peak value of the sum, ν_{max}, given in black. Frequency ranges Γ_k for a given kinetic energy $\mathcal{E}_0$ of a colliding pair is indicated by vertical arrows.

arrows positioned at the kinetic energy of a colliding pair $\mathcal{E}_0$, indicate the frequency ranges

$$\begin{aligned}\Gamma_1 &\equiv [0, \nu_1(\mathcal{E}_0)\rangle \ , \\ \Gamma_2 &\equiv [\nu_1(\mathcal{E}_0), \nu_1(\mathcal{E}_0) + \nu_2(\mathcal{E}_0)\rangle \text{ and} \\ \Gamma_{\text{null}} &\equiv [\nu_1(\mathcal{E}_0) + \nu_2(\mathcal{E}_0), \nu_{\text{max}}] \ .\end{aligned}$$

A Monte-Carlo selection is performed, where collision type k is triggered when the criterion

$$R \in \Gamma_k / \nu_{\text{max}}$$

is satisfied for a random number R drawn from a uniform distribution $U[0, 1]$.

Figure 3.6 show test results from the MCC-PIC selection algorithms, for the elastic scattering of electrons and neutral Argon atoms, where the cross section $\sigma(\mathcal{E})$ used as input to the MCC-PIC package is obtained from laboratory experiments (Ferch et al., 1985). The top panel show the particle distributions of the electrons $f_e(\mathcal{E}_e)$ and Argon atoms $f_{Ar}(\mathcal{E}_{\text{Ar}})$ as functions of the kinetic energy of each particle specie $\mathcal{E}_e$ and $\mathcal{E}_{\text{Ar}}$. The bottom panel show the collision frequency $\nu_0(\mathcal{E})$ given by $\sigma(\mathcal{E})$, and the confidence intervals

$$\nu_0 \pm \Delta\nu = \nu_0(\mathcal{E}) \left(1 \pm \frac{1}{\sqrt{N_{\text{coll}}(\mathcal{E})}} \right) \tag{3.13}$$

is estimated from the number of collisions $N_{\text{coll}}(\mathcal{E})$ in each energy interval $(\mathcal{E}, \mathcal{E} + d\mathcal{E})$. The confidence intervals are sufficiently narrow for energies $\lesssim 10$ as in this region $N_{\text{coll}} \gg 1$. However, for higher energies, and especially for $\mathcal{E} \gtrsim 20$, the confidence intervals becomes too wide for any reliable application. Collision frequencies of the collided particles, $\nu_{\text{exp}}(\mathcal{E})$, is estimated from the time between collisions $\tau_{c,j}$ for each particle j, sorted by the energy $\mathcal{E}$ of the

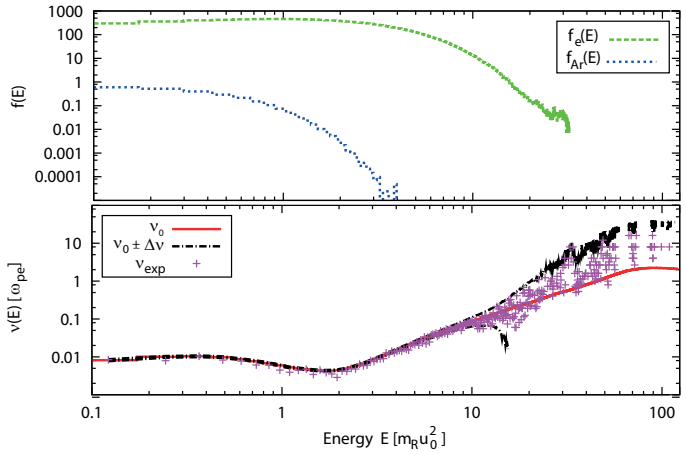

Figure 3.6: Test results of the null-method. Top panel show the particle distributions $f_e(\mathcal{E}_e)$ of electrons (green) and $f_{Ar}(\mathcal{E}_{Ar})$ (blue) of a neutral Argon gas, as functions of their respective kinetic energy $\mathcal{E}_e$ and $\mathcal{E}_{Ar}$ in the laboratory frame of reference. Lower panel show the collision frequency $\nu_0(\mathcal{E})$ (red) of electron-Argon scattering as function of the relative kinetic energy $\mathcal{E}$ of the colliding pairs in the centre-of-mass frame of reference. Estimated collisional frequencies $\nu_{exp}(\mathcal{E})$ from the numerical collisions are shown (purple $+$-marks). Confidence intervals $\nu_0 + \Delta\nu$ are shown in black.

collisions. The collision frequency $\nu_{\text{exp}}(\mathcal{E})$ is thus an average of $\tau_{c,j}^{-1}$ over all collisions in the energy intervals $(\mathcal{E}, \mathcal{E} + d\mathcal{E})$,

$$\nu_{\text{exp}}(\mathcal{E}) = \frac{1}{N_{\text{coll}}(\mathcal{E})} \sum_j \tau_{c,j}^{-1}(\mathcal{E}) \; . \tag{3.14}$$

The values of $\nu_{\text{exp}}(\mathcal{E})$ are plotted together with $\nu_0(\mathcal{E})$ in the bottom panel of Figure 3.6, where it is evident that the MCC-PIC package is able to reproduce the given collision frequencies $\nu_0(\mathcal{E})$ within the confidence intervals (3.13).

Performing collisions

The numerical representation of collisions in PIC codes is done by transforming the velocities of the simulated particles

$$\mathbf{u} \to \mathbf{u}' \; , \tag{3.15}$$

in accordance with the collisional mechanisms modelled, where $\mathbf{u}'$ is the particles velocity after having collided. The details of the transformation is given by the cross section $\sigma(\mathcal{E})$, scattering angle $\chi(\mathcal{E})$ and change in energy $\Delta\mathcal{E}(\mathcal{E})$, usually obtained from laboratory experiments of the various collision mechanisms. The current algorithms for colliding particles take these properties as input and calculates the velocity transform for each single event. Figure 3.7 illustrates a binary Coulomb collision between two particles of equal charge, in the laboratory and in the

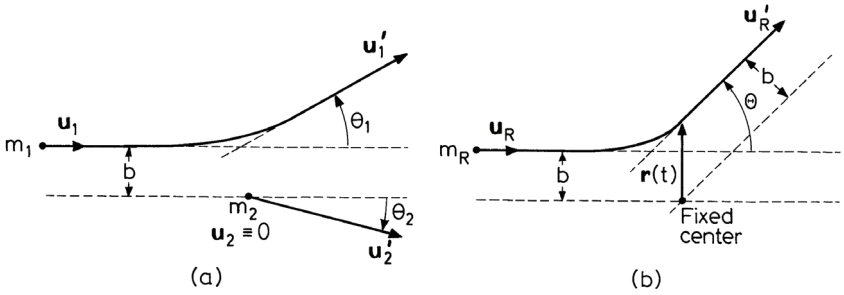

Figure 3.7: Collisions between two charged particles with charge e in the fixed frame (a) and center-of-mass frame (b) of reference. The line with the arrow indicates the trajectory of the particle. Figure reproduced from Pécseli (2013).

centre-of-mass frames of reference, where the primed quantities, e.g. $\mathbf{u}'_R$, indicate the particle properties after the collision.

The simplest mechanisms considered here are charge exchange collisions, where singly charged ions and neutral atoms of the same specie (e.g. Argon) exchange one electron, thus causing the atom to become an ion and the ion an atom. With respect to the plasma dynamics, this appears as if the ions suddenly adapt the velocities of the (former) atom. Given a colliding pair of an ion and an atom, the velocity transform (3.15) is done by replacing the ion velocity with the atom velocity,

$$\mathbf{u}_{\text{ion}} = \mathbf{u}_{\text{atom}} \ .$$

Given the initial assumptions that the distribution functions of the neutral atoms is stationary in time, uniform in space and a priori specified in velocity space, it is not necessary to model the newly formed atom.

Elastic and inelastic scattering involves more complex algorithms, where the change in energy $\Delta\mathcal{E}(\mathcal{E})$, the scattering angle $\chi(\mathcal{E})$ and the plane in which the collision occurs given by the initial relative velocity $\mathbf{u}_R$ and the azimuthal angle ϕ, enters trigonometric equations of the velocity transformation (3.15). Each of these quantities must be evaluated in the centre-of-mass frame of reference, so a transform of velocities and energies from the laboratory to the centre-of-mass frame of reference is required. The relative velocity $\mathbf{u}_R$ is rotated by the scattering angle $\chi(\mathcal{E})$ and in the plane given by the azimuthal angle ϕ, and the magnitude of $\mathbf{u}_R$ is changed if the collision process is inelastic, i.e. $\Delta\mathcal{E}(\mathcal{E}) < 0$. Finally, the velocities are transformed back to the laboratory frame of reference,

$$\mathbf{u} \xrightarrow{\chi,\phi,\Delta\mathcal{E}} \mathbf{u}' \ ,$$

thus completing the velocity transform (3.15)

Chapter 4

Summary of papers

Paper I presents results of a PIC numerical study of the phase space dynamics of a plasma diode and the transition from a stable configuration to one where oscillations are driven by the potential relaxation instability. We examine the non-linear interaction of electrons and ions with the oscillations and identify how the different inertia of electrons and ions control the oscillation frequency. How these oscillations react to forced oscillations in the diode potential, and damping effects due to charge exchange and ion scattering collisions are investigated to give a broader understanding of the dynamics.

Paper II discuss results of PIC numerical study of the self-similar expansion of an initial step-like ion density distribution in a plasma column. We identify strong acceleration of the ions at an early stage during the expansion phase and the expansion with the self-similar variable $\xi = x/t$. We observe the transition to a non-self-similar expansion as the mean free path ℓ_c of charge exchange collisions is decreased to a fraction of the plasma column length.

Paper III investigates particle acceleration at quasi-perpendicular, supercritical, collisionless shocks in supernova remnants in the presence of minority heavy ion species. These shocks are believed to be the origin of cosmic ray particles and the pre-acceleration mechanisms in these shocks are investigated. We present the first systematic set of fully self-consistent PIC simulations spanning the full range of heavy ion densities, and how shock acceleration mechanisms depend on these.

Bibliography

Aharonian, F. et al. (2007). Primary particle acceleration above 100 TeV in the shell-type supernova remnant RX J1713.7-3946 with deep HESS observations. *Astronomy & Astrophysics 464*, 235.

Bell, A. B. (1978). Acceleration of cosmic-rays in shock fronts. *MNRAS 182*, 147–156.

Birdsall, C. K. (1991). Particle-in-cell charged-particle simulations, plus monte carlo collisions with neutral atoms. *IEEE Transactions on Plasma Science 19*, 2.

Birdsall, C. K. and A. B. Langdon (1985). *Plasma Physics Via Computer Simulations*. New York, NY, USA: McGraw-Hill, Inc.

Blandford, R. D. and J. P. Ostriker (1978). Particle acceleration by astrophysical shocks. *Astrophysical Journal 221*, L29–L32.

Box, G. and M. Muller (1958). A note on the generation of random number deviates. *Annals Math. Stat. 29*, 610–611.

Chapman, S. C., R. E. Lee, and R. O. Dendy (2005). Perpendicular shock reformation and ion acceleration. *Space Science Reviews 121*, 5–19.

Chen, F. F. (1984). *Introduction to Plasma Physics and Controlled Fusion*, Volume 1. New York and London: Plenum Press.

Courant, R., K. Friedrichs, and H. Lewy (1928). On the partial difference equations of mathematical physics. *Mathematische Annale 100*, 32–74.

Devroye, L. (1986). *Non-Uniform Random Variate Generation*. New York, NY, USA: Springer-Verlag.

Enomoto, R. et. al. (2002). The acceleration of cosmic-ray protons in the supernova remnant RX J1713.7-3946. *Nature 416*, 423.

Ferch, J., B. Granitza, C. Masche, and W. Raith (1985). Electron-argon total cross section measurements at low energies by time-of-flight spectroscopy. *Journal of Physics B: Atomic and Molecular Physics 18*(5), 967.

Fermi, E. (1949). On the origin of cosmic radiation. *Physical Review 75*, 1169–1174.

Hackbusch, W. (1985). *Multi-Grid Methods and Applications*. Springer Science+Business Media UK Ltd., London WC1X 8HB, United Kingdom: Springer.

Haugbølle, T., J. T. Frederiksen, and Å. Nordlund (2013). photon-plasma: A modern high-order particle-in-cell code. *Physics of Plasmas 20*, 6.

Hendel, H. W., T. K. Chu, and P. A. Politzer (1968). Collisional drift waves – identification, stabilization, and enhanced plasma transport. *Phys. Fluids 11*, 2426.

Iizuka, S. and R. Schrittwieser (1993). Effects of a radial electric-field on low-frequency instabilities in a magnetized plasma. *Plasma Physics and Controlled Fusion 35*(1), 77–91.

Klimontovich, I. U. L. (1967). *The statistical Theory of Non-Equilibrium Processes in a Plasma*. Cambridge, Massachusetts, USA: The Massachusetts Institute of Technology Press.

Koyama, K., R. Petre, and E. V. Gotthelf (1995). Evidence for shock acceleration of high-energy electrons in the supernova remnant SN1006. *Nature 378*, 225.

Lee, R. E., S. C. Chapman, and R. O. Dendy (2004). Numerical simulations of local shock reformation and ion acceleration in supernova remnants. *Astrophysical Journal 604*, 187–195.

Lembege, B. and P. Savoini (1992). Nonstationarity of a two dimensional quasi-perpendicular supercritical collisionless shock by self reformation. *Physics of Fluids B: Plasma Physics 4*, 3533.

Liewer, P. C. (1985). Measurements on microturbulence in Tokamaks and comparison with theories of turbulence and anomalous transport. *Nucl. Fusion 25*, 543–621.

McDaniel, E. W. (1989). *Atomic collisions : electron and photon projectiles*. New York, NY, USA: Wiley.

McDaniel, E. W., J. B. A. Mitchell, and M. E. Rudd (1993). *Atomic collisions : heavy particle projectiles*. New York, NY, USA: Wiley.

Motley, R. W. (1975). *Q-machines*. New York: Academic Press.

Pécseli, H. L. (2013). *Waves and Oscillations in Plasmas*. Taylor & Francis Group, Boca Raton, FL, USA: CRC Press.

Plaga, R. (2008). Astrophysics: Rays from the dark. *Nature 453*, 48–49.

Rekaa, V. L. (2009). Numerical simulations of double layers in plasmas. Master's thesis, Institute of Physics, University of Oslo, Norway.

Schlitt, L. G. and H. W. Hendel (1972). Effects of parallel wavelength on the collisional drift instability. *Phys. Fluids 15*, 1578.

Schmitz, H., S. C. Chapman, and R. O. Dendy (2002). The influence of electron temperature and magnetic field strength on cosmic-ray injection in high mach number shocks. *Astrophysical Journal 570*, 637–646.

Scholer, M., I. Shinohara, and S. Matsukiyo (2003). Quasi-perpendicular shocks: Length scale of the cross-shock potential, shock reformation, and implication for shock surfing. *Journal of Geophysical Research 108*, 4–1 – 4–11.

Shimada, N. and M. Hoshino (2000). Strong electron acceleration at high mach number shock waves: Simulation study of electron dynamics. *Astrophysical Journal Letters 543*, L67.

Simonen, T., T. Chu, and H. Hendel (1970). Anomalous resistivity due to current-driven instabilities in Q-machine plasmas. *Bulletin of the American Physical Society 15*(4), 532.

Skullerud, H. R. (1968). Stochastic computer simulation of ion motion in a gas subjected to a constant electric field. *Journal of Physics D-Applied Physics 1*(11), 1567.

Tang, W. M. and V. S. Chan (2005). Advances and challenges in computational plasma science. *Plasma Physics and Controlled Fusion 47*, R1–R34.

Trulsen, J. K. (2005). *Introduction to Numerical Simulation of Many-Particle Systems, Methods and Applications*. Institute of Theoretical Astrophysics, University of Oslo, Norway.

Vahedi, V. and M. Surendra (1995). Monte carlo collision model for the particle-in-cell method: applications to argon and oxygen discharges. *Computer Physics Communications 87*, 179–198.

Wilhelmsson, H. (2000). *Fusion. A Voyage Through the Plasma Universe*. Bristol and Philadelphia: Institute of Physics Publishing.

Wong, A., R. W. Motley, and N. D'Angelo (1964). Landau damping of ion acoustic waves in highly ionized plasmas. *Phys. Rev. 133*, A436–A442.

Yee, K. S. (1966). Numerical solution of initial boundary value problems involving Maxwell's equations in isotropic media. *IEEE Transactions on Antennas and Propagations 14*, 302–307.

Paper I

I

Numerical studies of a plasma diode with external forcing

V. L. Rekaa, H. L. Pécseli and J. K. Trulsen
Physics of Plasmas, **19**, 082115 (2012)

PHYSICS OF PLASMAS 19, 082115 (2012)

Numerical studies of a plasma diode with external forcing

V. L. Rekaa,[1,a)] H. L. Pécseli,[1,b)] and J. K. Trulsen[2,c)]
[1]Department of Physics, University of Oslo, Box 1048 Blindern, N-0316 Oslo, Norway
[2]Institute of Theoretical Astrophysics, University of Oslo, Box 1029 Blindern, N-0315 Oslo, Norway

(Received 30 March 2012; accepted 7 August 2012; published online 23 August 2012)

With reference to laboratory Q-machine studies we analyze the dynamics of a plasma diode under external forcing. Assuming a strong axial magnetic field, the problem is analyzed in one spatial dimension by a particle-in-cell code. The cathode is assumed to be operated in electron rich conditions, supplying an abundance of electrons. We compare different forcing schemes with the results obtained by solving the van der Pol equation. In one method of forcing we apply an oscillation in addition to the DC end plate bias and consider both amplitude and frequency variations. An alternative method of perturbation consists of modelling an absorbing grid at some internal position. Also in this case we can have a constant frequency with varying amplitude or alternatively an oscillation with chirped frequency but constant amplitude. We find that the overall features of the forced van der Pol equation are recovered, but the details in the plasma response need more attention to the harmonic responses, requiring extensions of the model equation. The analysis is extended by introducing collisional effects, where we emphasize charge exchange collisions of ions, since these processes usually have the largest cross sections and give significant modifications of the diode performance. In particular we find a reduction in oscillator frequency, although a linear scaling of the oscillation time with the system length remains also in this case. © *2012 American Institute of Physics*. [http://dx.doi.org/10.1063/1.4747620]

I. INTRODUCTION

The present paper discusses the performance of a long plasma diode of length $\mathcal{L}$ as studied by numerical methods. The basic model corresponds to a single ended Q-machine,[1,2] where electrons are emitted thermally while ions are produced by surface ionization at a hot cathode. In the basic version of the Q-machine the ions are produced by contact ionization[3] of hot alkali metals with suitable work functions.[4] The metal plate also supplies electrons by Richardson emission. We will in the following assume that a confining axial magnetic field is sufficiently strong to justify a description in one spatial dimension. This configuration has been studied extensively for instance to find steady state potential variations, some involving trapped plasma populations or "virtual cathodes."[5–7] For weaker magnetic fields the dynamics are changed since the particles are no longer confined to move along the magnetic field lines.[8] Our analysis emphasizes results relevant for Q-machines where $\mathcal{L}/\lambda_{De} > \sqrt{M/m}$ in terms of the Debye length λ_{De} and the electron-ion mass ratio M/m, but the basic principles have more general applications, for instance for diodes.[9,10] Diodes as well as Q-machines can be operated in electron rich or ion rich conditions, depending on the relative abundance of the two species emitted at the surface. The present study assumes electron rich conditions which are also the most common one for Q-machine applications.

The performance of an oscillating diode with a cold positively biased end plate is usually modelled by a van der Pol equation.[11–13] The present study will address the accuracy of the van der Pol model for describing the diode for unstable conditions. For a freely oscillating diode, the conditions are well defined. In the case of external forcing, also included in the van der Pol model, the situation is ambiguous: it is not obvious how to apply perturbations to a physical diode. Several methods will be discussed and compared here. The basic diagnostics of the diode performance will be the fluctuating current through the diode.

Several studies discuss chaotic behaviour of diodes,[14,15] but these topics will not be addressed here. Also, non-neutral diodes have been studied elsewhere.[16–19]

II. STANDARD CONDITIONS

Under standard operating conditions for a Q-machine, we have electron rich conditions, where the hot plate at $x = 0$ can supply electrons in abundance. The electrons are emitted with a velocity distribution $n_{0e}\sqrt{2m/\pi T_0}\exp(-\frac{1}{2}mu^2/T_0)$ for $u > 0$, where T_0 is the hot plate temperature in energy units, and similarly for ions we have $n_{0i}\sqrt{2M/\pi T_0}\exp(-\frac{1}{2}Mu^2/T_0)$, where we assume $n_{0e} > n_{0i}$. The distribution functions are normalized over the interval $u \in \{0;\infty\}$. Our reference case corresponds to electron rich conditions with $n_{0e}/n_{0i} = 2$. For such cases, the plasma assumes a negative potential in front of the cathode in order to reflect the surplus of electrons, while ions on the other hand are accelerated by the potential drop. The numerical plasma injection scheme used here differs from the one used in some other related studies.[20]

With standard operation, the cold end plate at $x = \mathcal{L}$ is biased negatively at a potential $-\Psi$, reflecting most of the electrons: only the most energetic tail of the Maxwellian velocity distribution has sufficient energy to overcome the

a)Electronic mail: v.l.rekaa@fys.uio.no.
b)Electronic mail: hans.pecseli@fys.uio.no.
c)Electronic mail: jan.trulsen@astro.uio.no.

reflecting potential, while all ions will be absorbed at the end plate. For long systems we have conditions where the plasma is quasi-neutral and has a large region at an approximately constant potential, the plasma potential $-\Phi_p$. The plasma is not in thermal equilibrium and for $x > 0$ it has no characteristic temperature. A useful length-measure will here be the Debye length defined in terms of the reference temperature T_0. Similarly we can define a reference ion sound speed by the same temperature. For conditions relevant for the present study, the plasma density will be inhomogeneous and non-stationary. To have an unambiguous definition of a Debye length we use n_{0e} for the density.

We first assume the axially varying potential to be negative, $-\Phi(x)$ with $\Phi(x) > 0$, for all x. For the ion density we have the consistency relation

$$n_i(x) = n_{0i} \exp(e\Phi/T_0)(1 - \mathrm{erf}\sqrt{e\Phi/T_0}), \quad (1)$$

with erf being the error function. For the electrons we have

$$n_e(x) = n_{0e} \exp(-e\Phi/T_0)\left(1 + \mathrm{erf}\sqrt{e(\Psi - \Phi)/T_0}\right), \quad (2)$$

as long as the end plate potential is below the plasma potential in the device, $\Psi > \Phi_p > 0$. For given T_0, n_{0e}, n_{0i}, and Ψ, the plasma potential Φ_p is found by setting $n_e = n_i$. For varying Ψ, the resulting equation is solved most easily by graphical methods. No solution with a quasi-neutral plateau exists for small Ψ (more precisely, for $n_{0e}/n_{0i} = 2$ and a range $-1.73 < e\Psi/T_0 < 0.2$, no solution with a quasi-neutral plateau exists. This domain corresponds to oscillatory solutions). For a very negative end plate bias $\Psi \to \infty$ with $\mathrm{erf}\sqrt{e(\Psi - \Phi)/T_0} \to 1$, where all electrons are reflected at $x = \mathcal{L}$, the plasma potential is determined as the solution of $\exp(2e\Phi_p/T_0)(1 - \mathrm{erf}\sqrt{e\Phi_p/T_0}) = 2n_{0e}/n_{0i}$, giving for instance $e\Phi_p/T_0 \approx 2.57$ for $n_{0e}/n_{0i} = 2$. Plasma potentials observed in Q-machines[1] are of this order of magnitude. The mass ratio does not enter the result, and only the density ratio n_{0e}/n_{0i} is important, not the individual densities. As long as the end plate is negative compared to the plasma potential, $|\Psi| > |\Phi_p|$, we have the ion current contribution to be constant and equal to the ion flux at the hot plate, $en_{0i}\sqrt{2T_0/M\pi}$. The electron current $en_{0e}\sqrt{2T_0/m\pi}\exp(-e\Psi/T_0)$, on the other hand, changes due to the change in electrons absorbed at the end plate when Ψ is varied.

The average ion velocity at any position x is given by

$$U_i = \sqrt{\frac{2T_0}{\pi M}}\frac{n_{0i}}{n_i(x)} = \sqrt{\frac{2T_0}{\pi M}}\frac{\exp(-e\Phi(x)/T_0)}{1 - \mathrm{erf}\sqrt{e\Phi(x)/T_0}}, \quad (3)$$

using Eq. (1). Defining the edge of the end plate sheath as the position where we have quasi-neutrality, $n_i = n_e$, we can determine the average velocity of the ions as they arrive at the sheath edge for varying bias Ψ. For our reference case with $n_{0e}/n_{0i} = 2$ we find graphically that $U_i \geq 1.8\sqrt{T_0/M}$ for all values of Ψ that allow solutions for a steady state plasma potential Φ_p. A sound speed for the present conditions cannot be defined uniquely, since in general neither ions nor electrons are in thermal equilibrium, but if we use $C_s \approx \sqrt{T_0/M}$ as an estimate, we can argue that the Bohm condition[21,22] is fulfilled with a good margin also in the present case. For the present conditions, the ion accelerating pre-sheath is found at the cathode. Here the pre-sheath is not quasi-neutral as usually assumed.[22]

As long as the end plate bias is below the plasma potential, $|\Phi_p| < |\Psi|$, we have a monotonically decreasing potential $\Phi(x)$, giving a one-to-one correspondence between potential and the axial x-position. Plotting the density difference $n_i - n_e$ as a function of Φ we find that $n_e > n_i$ for all $|\Phi| < |\Phi_p|$, while $n_e < n_i$ for all $|\Phi| > |\Phi_p|$. If we insert the charge density $e(n_i - n_e)$ with Eqs. (1) and (2) into Poisson's equation we conclude (even without solving for $\Phi(x)$) that the curvature of the potential variation $d^2\Phi(x)/dx^2$ is consistent with an electron rich sheath at $x \approx 0$ and an ion rich sheath at $x \approx \mathcal{L}$.

When the end plate potential is changed to be less negative, more electrons will be absorbed at $x = \mathcal{L}$, while all ions will still be absorbed. Eventually the plasma potential and end plate potential become equal. As the end plate potential is made even less negative, the curvature $d^2\Phi(x)/dx^2$ should change to give an electron rich sheath. Since all particles originate from the cathode at $x = 0$, the only way more electrons can arrive at $x \approx \mathcal{L}$ is by changing the plasma potential to be less negative, so that less electrons are reflected by the sheath at $x \approx 0$. From then on the plasma potential will follow the end plate bias as $\Psi \to 0$. At some critical potential it is no longer possible to supply enough electrons and the sheath at the end plate becomes unstable. It is the dynamics of these unstable conditions we study in this work. The origin of the oscillations is often termed the "potential relaxation" instability.[23,24]

Particular attention is here given to the diode response to external perturbations when its end plate is biased positively with conditions that give spontaneously excited oscillations. The results are compared to predictions obtained by the standard van der Pol equation[11,12] that is often used to model this type of diodes. It is demonstrated that this model can account for the free oscillations, while only qualitative agreement is found for the driven cases. Several methods for introducing perturbations of the diode were considered.

Our particle-in-cell (PIC) code is standard,[25] with one important feature being the freedom to impose conditions at the ends of the system, allowing for both Dirichlet and von Neumann conditions. The code allows for introducing collisional effects also. We use the mass ratio for electrons and Hydrogen ions, $M/m = 1836$ and approximately 10^6 particles of each species. The assumed mass ratio can only be considered as representative: a Q-machine, for instance, is usually operated with low ionisation potentials alkali metals, resulting in larger mass ratios. Some early numerical study of diode performance[26] assumed ion to electron mass ratios $M/m \leq 128$, and 3×10^3 particles altogether. Later studies[13] were content with $M/m = 10$, arguing that not much additional knowledge is gained by use of larger M/m-values.

III. PLASMA CONDITIONS WITH VARYING BASIC PARAMETERS

For computational reasons we restrict the length of the system to be $\mathcal{L} = 10^3\lambda_{De}$, noting that we by this choice have

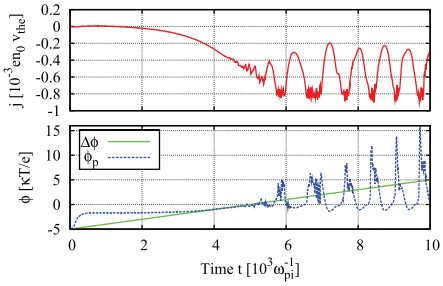

FIG. 1. Variation of the current through the diode (top) and plasma potential at $x = \mathcal{L}/2$ (bottom) for varying end plate bias. Also the externally applied potential sweep at the end plate is shown. The initial current is vanishing since we start with an empty diode.

$\mathcal{L} \gg \lambda_{De}\sqrt{M/m}$ in the reference cases studied. In all cases we initiate the plasma column so that the electrons and ions from the cathode are injected into empty space at $t = 0$. For the given initial condition, the plasma current contains a transient initial part. As an interesting feature we note that very early in the process some of the ions are accelerated to very high velocities, up to 20% of the electron thermal velocity, although the density of these ions is very low.[27] At a later stage, the ions are accelerated by the potential drop at the cathode sheath, and here the velocities are only of the order of $\sqrt{T_0/M}$. The initial acceleration is seen best in a video representation.

To illustrate the basic operating conditions of the plasma diode, we show in Fig. 1 the variations in diode current and plasma potential at $x = \mathcal{L}/2$ as the end plate potential is swept from a large negative to a large positive bias. As long as $-\Psi$ is negative we find a slow change in the current, but at a well defined threshold value, here at $\Psi \approx 0$, we find a sudden onset of low frequency oscillations. The variations in plasma potential and current follow each other, so in the following we use the diode current as the sole diagnostic for the diode performance. Details of the phase space dynamics of ions as well as electrons can be seen in Video 1 (see summary in Fig. 2). During the time interval when $-1 < e\Psi/T_0 < 1$, we find the onset of an instability with wave-length $\lambda \approx \frac{1}{4}\mathcal{L}$, with characteristics different from the saturated diode oscillations. These spontaneously excited, short wavelength, oscillations are assumed to be caused by the ion-electron two stream instability. These oscillations are found only for a narrow interval of the end plate bias.

As long as the end plate potential is sufficiently negative to reflect the majority of the electrons, we find a stable negative plasma potential Φ_p. As the end plate potential $-\Psi$ is made less negative we reach the condition where $|\Psi| = |\Phi_p|$, and from this stage the plasma potential is following Ψ until $\Psi \approx 0$. At this point the sheath becomes unstable, and large

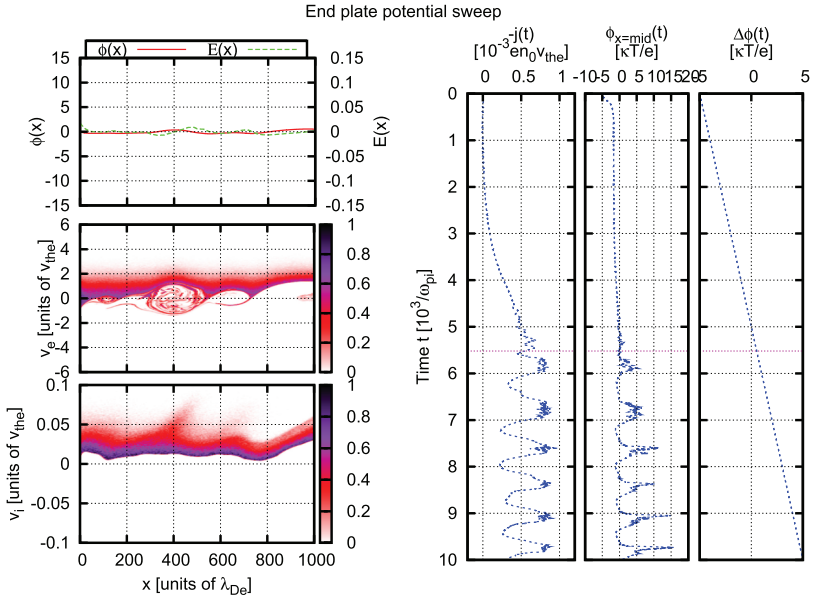

FIG. 2. Summary figure for Video 1, showing also the phase space dynamics. The column to the left shows from the top the potential and electric fields as a function of position. Below we find first the electron phase space and then at the bottom, the ion phase space. The triple column on the right hand side shows the net plasma current (left) and the applied signal (right) with time increasing from top to bottom. The middle panel shows the plasma potential at a position $x = \mathcal{L}/2$. A moving dotted horizontal line gives the time during the video. The frames to the left are obtained at the time indicated by a horizontal dotted line on the right hand side (enhanced online) [URL: http://dx.doi.org/10.1063/1.4747620.1].

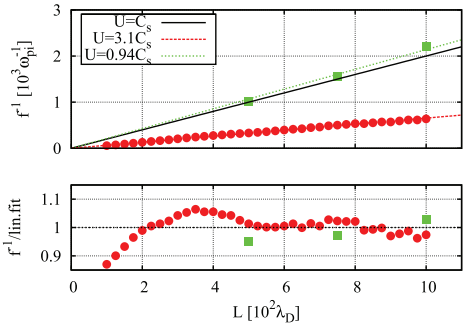

FIG. 3. Illustration of the period of the oscillation of the diode at a large positive bias for varying length of the system $\mathcal{L}$ shown in the top frame with filled red circles. The full line gives $2\mathcal{L}/C_s$ as reference. In the bottom frame we divided the observed normalized oscillation period by the best linear fit to the data in the top frame. With filled green squares we give selected results where the ions undergo change exchange collisions, as explained in Sec. VI.

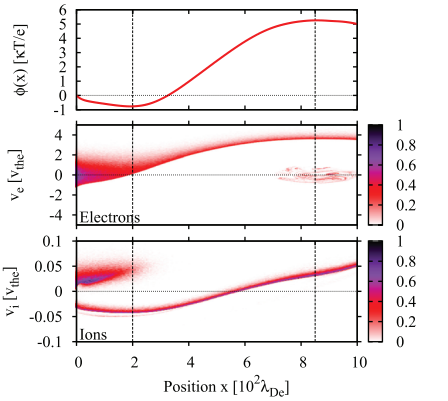

FIG. 4. Selected sample of spatial potential variation together with corresponding electron and ion phase spaces, illustrating transient double layer like features. The time is $t = 1270.47\,\omega_{pi}^{-1}$, i.e., a late time when the plasma has settled in a steady oscillatory state.

amplitude, low frequency oscillations are excited (see also Fig. 1). Once the system is unstable, its basic oscillation frequency and saturated amplitude is found to be independent of further increases in the end plate potential, indicating a saturation. The basic oscillation frequency of the oscillations is inversely proportional to the length of the system, as illustrated in Fig. 3. This scaling could invite an interpretation of the instability as a current driven ion acoustic mode,[28] where the most unstable frequency could be assumed to be $f_a \approx C_s/2\mathcal{L}$. If we introduce the standard definition $C_s = \sqrt{T_0/M}$, we find that the observed frequency is approximately 3 times larger than f_a. The simulation allows parameter variations to be obtained with an accuracy much better than what is found in a laboratory. We note that for $\mathcal{L} < 500\lambda_{De}$ there are small but measurable and systematic deviations from this simple proportionality between f_0^{-1} and $\mathcal{L}$. For very short systems, $\mathcal{L} < 80\lambda_{De}$, the oscillations disappear. We attribute this feature to be associated with an overlap of the electron and ion rich sheaths at $x \approx 0$ and $x \approx \mathcal{L}$, respectively.

The details of the phase space dynamics are best seen in Video 1 (Fig. 2). In Fig. 4 we show a sample of phase space for a selected time when the end plate is kept on a constant positive potential. At this time we find features usually associated with a double layer,[23,29] in this case one moving with a velocity of approximately 0.02 v_{the} with v_{the} being the electron thermal velocity derived from the cathode temperature T_0. The analogy is best seen by concentrating on the part of phase space between the two vertical dashed lines. The important feature is that the free ions moving in the negative direction towards the cathode are some that have been reflected by the positive potential at the end plate. The trapped electron component is in reality a "blob" of electrons oscillating in a moving local potential maximum.[9] The double layer like structure dissolves when the source of reflected ions from the end plate is temporarily disrupted. The whole process repeats with the period of the instability.

For completeness we show in Fig. 5 the space-time variation of the electrostatic potential and the corresponding net plasma current variation. The slope of the slanting shaded area in both figures gives a characteristic propagation velocity that corresponds to the velocity of the double layer like feature in Fig. 4.

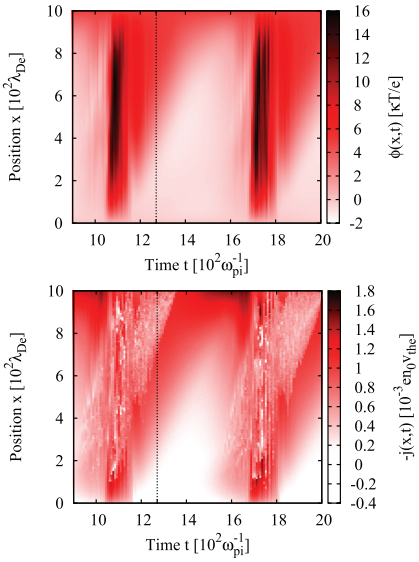

FIG. 5. Selected time interval of unstable diode oscillations. The top figure shows the space-time variation of the electrostatic potential, the lower figure shows the corresponding net plasma current variation. The vertical dashed line shows the time for the phase-space presentation shown in Fig. 4. In both cases the cathode is at the bottom of the figure.

Video 1 (Fig. 2) shows the full temporal evolution of electron and ion phase spaces. The formation and propagation of the transient double layer can be observed, in particular. From Fig. 1 we note a locally enhanced high frequency noise component at the negative extremum of the plasma current. Inspection of Video 1 (Fig. 2) demonstrates that this noise is due to a localized irregular "blob" of electrons trapped near a local potential maximum. The oscillations of these trapped electrons in their local, approximately parabolic, potential well gives rise to the observed noise. The details in the dynamics of the trapped electron population will be susceptible to collisions as discussed in Sec. VI.

As a test, we monitored the total number of simulation particles in the system during the simulations. This number was pulsating with the periodicity of the oscillations due to the modulated losses, but with constant end-plate potential we saw no systematically decreasing or increasing trend in the particle number, when averaged over one oscillation period.

IV. THE VAN DER POL MODEL

A standard and widely used analytical model for studying the nonlinear properties of driven linearly unstable systems is the van der Pol model

$$\frac{d^2}{dt^2}\xi - (\alpha - \beta\xi^2)\frac{d}{dt}\xi + \omega_0^2\xi = A\omega_0^2 \sin(\omega_e t), \qquad (4)$$

where we included a harmonic forcing. The coefficients $\alpha > 0$ and $\beta > 0$ refer to the linear growth phase and the nonlinear saturation, respectively, while ω_0 is the natural frequency of the oscillator and A is the amplitude of the forcing term. The variable ξ denotes any quantity of physical interest; in most of the present study it will be taken to be the current through the system. The right hand side of Eq. (4) can be made more general, but the form used here is the one found most often. The form Eq. (4) can be simplified by introducing a normalized time $\tau = t\omega_0$ and a normalized amplitude $\eta = \xi/\xi_0$ with $\xi_0 \equiv \sqrt{\alpha/\beta}$ to obtain $d^2\eta/dt^2 - \epsilon(1-\eta^2)d\eta/dt + \eta = A\sin(\tau\omega_e/\omega_0)/\xi_0$ where $\epsilon = \alpha/\omega_0$.

The results of Fig. 1 indicate that the onset of the oscillations is sudden: they reach maximum amplitude within approximately one period of oscillations. This feature was confirmed also by other detailed simulations where the end plate potential was changed from being below to being above threshold by a step function. The van der Pol model therefore needs a growth rate comparable to the frequency. In Fig. 6 we show results for diode simulation data (shown with full line) and numerical solutions of the van der Pol equation (4) with $A = 0$ and parameters adjusted to $\alpha/\omega_0 = 0.1$ for optimum fit. The parameters are chosen to give the best fit to the numerical observations. The results summarized Fig. 6 indicate that the van der Pol equation is able to give a very convincing representation of the performance of the steady state oscillations of the plasma diode without forcing. We have analyzed a wide parameter range giving consistent results.

In Fig. 7 we show numerical solutions of the normalized van der Pol equation. Two cases are considered: one (top figure) by applying a chirped frequency with constant amplitude as forcing on the right hand side, and one (bottom figure) with a

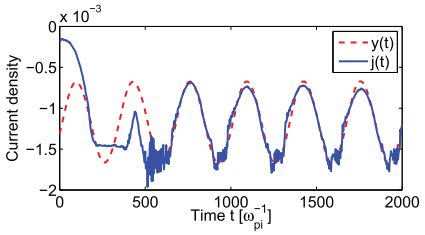

FIG. 6. Solution of the normalized van der Pol equation (dashed line) with parameters fitted to the data from the diode simulations (full line). Equation (4) is here solved without forcing with $\alpha/\omega_0 = 0.1$. The simulation data for the plasma current are obtained with a constant positive end plate bias.

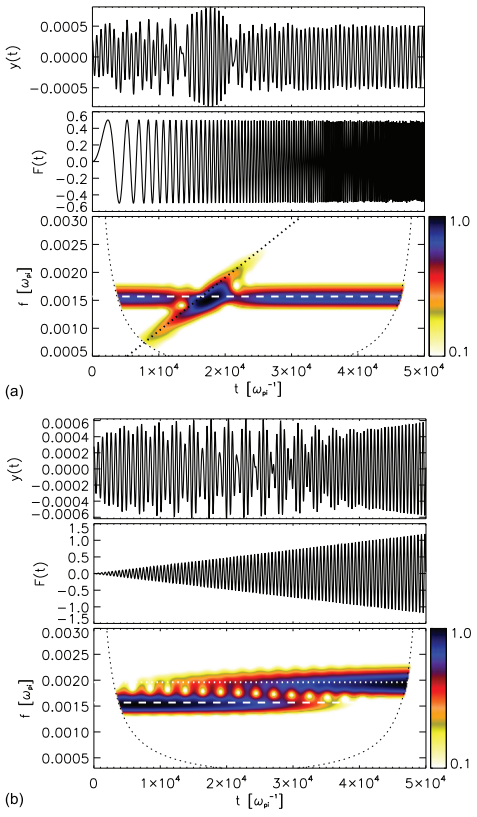

FIG. 7. Top figure: numerical solution of the van der Pol equation (4) in its normalized form with $\epsilon = 0.1$, here applying a chirped frequency with constant amplitude as forcing on the right hand side. The dotted oblique line gives the local frequency of the applied forcing. Bottom figure: forcing with constant frequency but with a linearly increasing amplitude. The wavelet transform of the resulting signal is shown in both cases.

constant frequency (here taken to be larger than f_0) but with a linearly increasing amplitude. The wavelet transform of the resulting signal is shown for both cases. The conspicuous feature of the solution with chirped frequency is the "frequency pulling" characteristic of the van der Pol equation. This is seen as the tilted frequency response in the local wavelet transform in the lower panel of Fig. 7(a), where the frequency of the oscillation response becomes synchronized with the applied signal. An increase in amplitude of the forcing increases the time interval where the synchronization can be observed. We note the absence of harmonic interactions in the numerical solutions. The constant frequency solutions illustrate how the natural mode of oscillation is stabilized (that is the frequency shifted or synchronized with the external forcing) for a sufficiently large amplitude of the excitation.

V. PERTURBATIONS OF THE DIODE

Mathematically, the question of forcing within the van der Pol equation is simple: an additional term is inserted on the right hand side as shown in Eq. (4). For a physical diode, a forcing can be applied in several ways, not necessarily equivalent.

The diode can be forced by applying a signal either to the end plate or at some internal position in the system. The two cases will be distinguished here, external end plate and internal forcings. One of the aims will be to analyze two of the characteristic features of the van der Pol model, synchronization and frequency pulling.[11,12,28] These features can be demonstrated most easily by a wavelet analysis of the data.[30]

We made two series of simulations, using two different forcing signals: one with a fixed frequency but varying amplitude and one with fixed amplitude but with "chirped" frequency.

The simplest form of external excitation (both in laboratory and in simulations) consists of applying an external signal to the cold end plate of the diode. The plasma diode can also be forced internally. In a Q-machine this forcing is usually achieved by immersing a fine-meshed grid in the plasma and then applying some time-varying signal to this grid. The operation of such a grid and its interaction with the plasma has been subject to some controversy,[6,31] where one model assumes that the local charge distribution is important and another that the modulated ion absorption is the dominant excitation mechanism. We start by discussion the two latter cases.

A. Oscillating localized electric field

We considered a model where externally controlled charges were introduced at two nearby grid-points (here separated by $10\lambda_D$) with opposite polarity. These charges came in addition to the ones arriving at the grid-points from the surrounding plasma. The excitation mechanism is here due to particle acceleration by the local electric field between the two charged grid-points. This form of excitation corresponds to a velocity modulation rather than a density modulation. We found that internal excitation by this method was indeed possible, but the charges applied had to be very large. The results were inconclusive and are not reported here. The excitation mechanism using an oscillating electric dipole was important for the early discussions of analytical studies of linear ion acoustic Landau damping.[31] As a practical method of wave excitation it seems to have little value in comparison to the model based on a grid giving a modulated particle absorption to be discussed in Sec. V B.

B. Locally modulated ion absorption

In Fig. 8 we show results from numerical simulations with internal excitation by modulated particle absorption, here by a signal chirped in frequency with constant oscillation amplitude. Ions are absorbed with a probability independent of their velocity. This form of excitation corresponds to the generally accepted model for wave excitation by a grid immersed perpendicular to the magnetized plasma column in a Q-machine.[6,28,32] For the case illustrated in Fig. 8 the absorption is strong, varying harmonically in the range 0%–70% at a position $3\mathcal{L}/7$, that is, the absorbing "grid" is at the position $x/\lambda_{De} \approx 430$. This method of excitation captures the essential part of grid excitation in, for instance, Q-machines at low applied frequencies. A missing element in the simulations is the electric fields being set up by the potential difference between the grid and the plasma vessel when a time varying potential is applied to the grid.

We note the distinct frequency pulling signature when the chirped frequency comes near the natural nonlinear oscillation frequency of the diode, i.e., in the frequency interval $f_0/2 - 3f_0/2$, approximately, where f_0 is the natural oscillation frequency. At the same time we note also an enhancement of the second harmonic, a feature not accounted for by the van der Pol equation. Even more interesting is the strong frequency pulling of the basic oscillator frequency observed

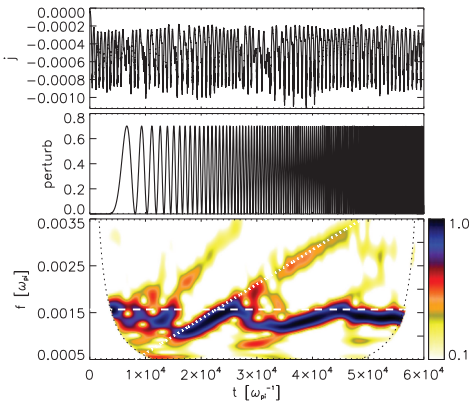

FIG. 8. Numerical simulations with internal excitation by modulated particle absorption, here by a chirped signal with constant amplitude. The top panel show the net current through the diode, the middle panel shows the time-varying absorption at a reference position, here at $x = (3/7)\mathcal{L}$, while the lower panel shows the wavelet transform of the time varying current. The horizontal dashed line in the lower panel shows the natural oscillation of the free oscillator for the given DC end plate bias, while the dotted oblique line gives the local frequency of the applied forcing.

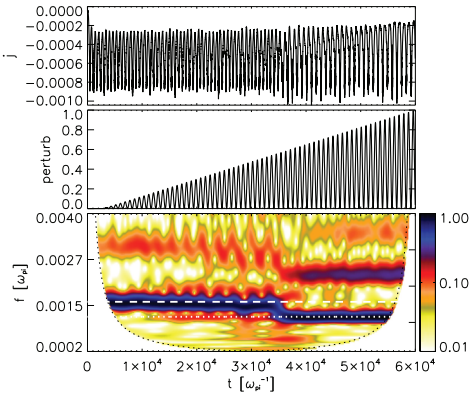

FIG. 9. Numerical simulations with internal excitation by modulated particle absorption, here by a signal with constant frequency somewhat below the natural oscillation frequency given by the dashed line (see also Video 2 (Fig. 10)). The amplitude of the oscillations increases from zero level with full ion transmission to 100% modulation where the ion transmission oscillates between 0 and 100%. The top panel show the net current through the diode, the middle panel shows the time-varying absorption at a reference position at $x = (3/7)\mathcal{L}$, while the lower panel shows the wavelet transform of the time varying current. The dashed line in the lower panel shows the natural oscillation frequency of the free oscillator for the given end plate bias, while the dotted line gives the frequency of the applied forcing.

when the applied frequency is in the range $3f_0/2 - 2f_0$. In this latter range, the strong oscillation has a frequency close to half the applied frequency. At reduced excitation amplitudes we will, however, see perturbations of the diode oscillations also at half oscillator frequency. These effects are masked in Fig. 8 by the frequency pulling which becomes effective already at frequencies close to half of the free oscillation frequency.

At time intervals when the applied frequency lies near the natural oscillation frequency f_0 and $3f_0/2$, we note excitation also of $f_0/2$. A weak signature of this frequency is seen also when the applied frequency is near $2f_0$.

We have tried different positions of the excitation point. Taking, for instance, $5\mathcal{L}/7$ we recover all the basic features of Fig. 8, but now with a reduced amplitude. Our conclusion from these and similar results is that the strongest excitation is found when the perturbation is close to the cathode. In this case the induced perturbation has the longest interaction distance with the ion flow before it reaches the end plate.

In Fig. 9 we show results where the frequency of the ion absorption is constant, but the temporally varying absorption ratio increases from 0 to 100% in the peak values. See also Video 2 (Fig. 10). The applied frequency is here below the natural frequency of the diode oscillations. For the present choice of parameters we find a transition in the oscillator characteristics at an absorption level of approximately 60%. Here the natural diode oscillations disappear completely, while we find a perfect locking to the applied frequency. At

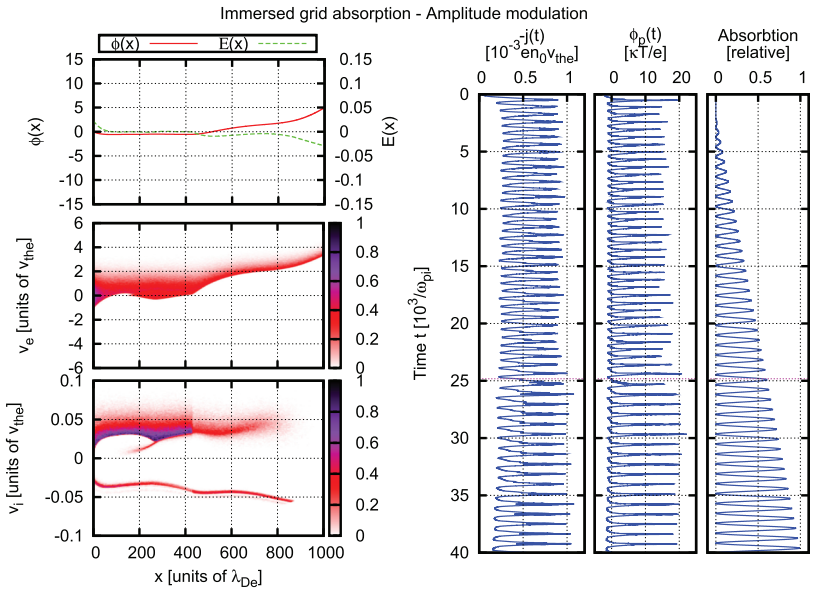

FIG. 10. Summary figure for Video 2, showing also the phase space dynamics. The simulations model an absorbing grid at position $x = 430\lambda_D$ where the time varying relative absorption is shown in the third frame to the right. See Fig. 2 for a detailed description of the set-up (enhanced online) [URL: http://dx.doi.org/10.1063/1.4747620.2].

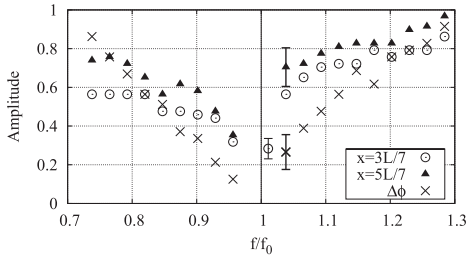

FIG. 11. Variation of the stabilizing amplitude with applied frequency. The error bar shown is representative for all open circles. Open circles correspond to the excitation applied at a position $3\mathcal{L}/7$, triangles to a position $5\mathcal{L}/7$. The error bar for the filled triangle represents the maximum uncertainty for those symbols. The figure also shows results (with $\times$-signs and a representative error bar) for the case where a signal is applied to the end plate.

the same time we find a very strong second harmonic enhancement, even the third harmonic becomes noticeable here. Prior to the onset of the synchronization we note a strong modulation of the free oscillator frequency and, in particular, also its second harmonic.

Consistent with the properties of the van der Pol model, we note that for a certain applied amplitude the free oscillation at frequency f_0 is quenched or stabilized, see again Video 2 (Fig. 10) (it may be confusing to use the term "stabilization" since the system is still oscillating at a large amplitude, but now at the applied frequency). The amplitude needed for this quenching depends on the applied frequency. We show in Fig. 11 results for the variation of this threshold amplitude for varying applied frequencies for two positions of the excitation. There is a noticeable asymmetry with respect to f/f_0, but qualitatively the results are similar to those expected from the van der Pol model, i.e., the threshold amplitude decreases as $|f - f_0|$ decreases, as also found experimentally.[32]

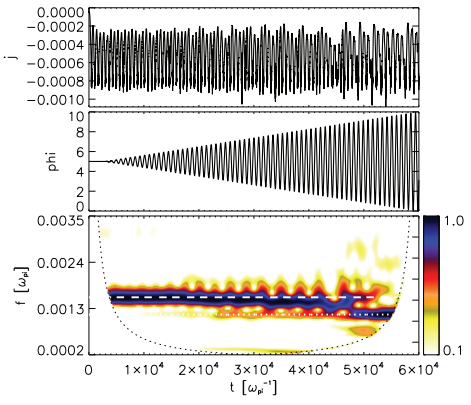

FIG. 12. The figure shows results for the case where a constant frequency with slowly increasing amplitude is applied to the positive end plate bias. The figure should be compared to Fig. 9.

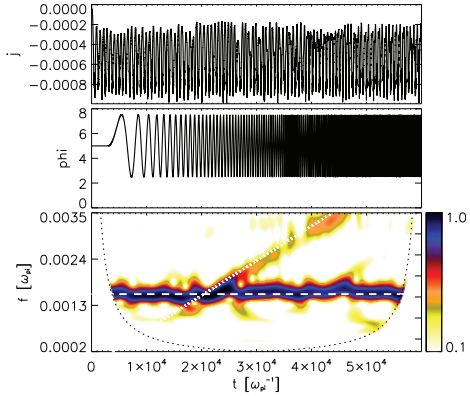

FIG. 13. The figure shows results for the case where a chirped frequency with constant amplitude is applied to the end plate. The figure should be compared to Fig. 8.

C. Modulated end plate bias

The external forcing can be applied also to the terminating end plate by adding a signal to the DC-bias. We used both amplitude and frequency modulations, as in Figs. 8 and 9. Illustrative results are shown Figs. 12 and 13 for a fixed frequency with linearly increasing amplitude and a fixed amplitude with chirped frequency, respectively. In many respects the results are similar to those found in Figs. 8 and 9, with one significant difference being in the harmonic content. We note the frequency pulling in Fig. 13 is very similar to that in Fig. 8, also when the local frequency approximates $2f_0$. Also, the frequency modulation in Fig. 12 is similar to what is seen in Fig. 9, but the signal at the second harmonic is completely absent. The feature near the frequency $f_0/2$ is absent in Fig. 13.

We show in Fig. 11 with crosses the normalized stabilizing amplitude A/A_0 where A_0 is the DC-bias applied to the end plate. For amplitudes $A > A_0$ the fundamental steady state oscillation amplitude is stabilized. We note also in this case a variation $A/A_0 \sim |f - f_0|$.

As a general feature we find that large amplitude oscillations have to be applied to the end plate in order to find observable effects: the amplitudes have to be significant fractions of the DC-bias. The necessary amplitudes depend on the DC-bias, provided the diode is conditioned to be in a fluctuating state.

VI. EFFECTS OF COLLISIONS

The foregoing analysis assumed ideal collisionless conditions. For realistic conditions we will often find that collisional effects cannot be ignored. Considering, for instance, a Q-machine operated with Caesium, which is a common practice, it is well known that the cross section for collisions of thermal electrons at relevant temperatures and neutral Caesium is particularly large.[33] Neutral Caesium originating from the neutral oven is found in abundance near the cathode. Also,

the ions will in this case experience collisions with the neutrals, where charge exchange collisions have the largest cross section, this type of interaction being resonant.[34]

We extended the analysis by considering also collisional interactions in the PIC-code.[20] Some basic features of our model are summarized in the Appendix. The numerical code offers an opportunity to introduce collisional effects for one species at a time: this is unphysical but offers an insight into the details in the process. We study ion neutral elastic collisions (IS), electron neutral elastic collisions (ES), and charge exchange ion collisions (CE). A summary of simulation results is presented in Fig. 14, where $\mathcal{L} = 10^3 \lambda_{De}$ as in Fig. 6. Two parameter regimes are analyzed: one where the scattering neutral gas temperature T_n equals the reference temperature T_0, while another case assumes $T_n = 0.15\,T_0$. In all cases we have taken the mean free path for collisions to be approximately 140 λ_D. For reference, we also include a result for the case where we have all collision processes activated: the mean free path for ion elastic and charge exchange collisions is here $460\lambda_D$ for both, giving an average ion mean free path of $230\lambda_D$, while the electron mean free path for elastic collision is $260\lambda_D$.

The characteristic diode oscillations are changed by the electron neutral collisions when we compare with the reference collisionless simulation also shown in Fig. 14. The high frequency oscillations due to the trapped electron component (see Video 1, Fig. 2) is quenched by the collisions, where we have the collisional mean free path to be shorter than the width of the potential well.[35] The form of the current signal becomes closer to the result obtained by the van der Pol model (see also Fig. 6). The sheath region near the emitting region at $x = 0$ is electron rich already without collisions,

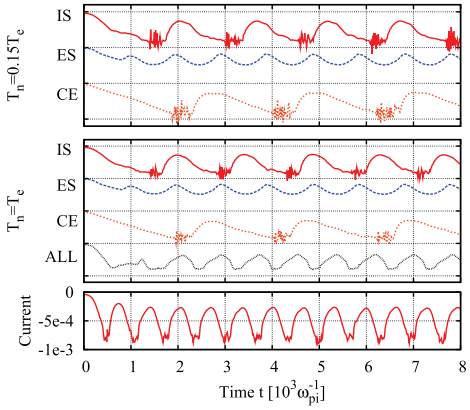

FIG. 14. Diode currents for selected collision processes. The bottom trace shows the reference calculations without collisions. The middle trace shows IS, ES, and CE, all assuming that the scattering neutral gas has the electron reference temperature at x = 0. The top frame shows results corresponding to the middle frame, but now with the scattering gas being colder, $T_n = 0.15\,T_0$. The trace denoted "ALL" represents a simulation where all collisions are activated simultaneously.

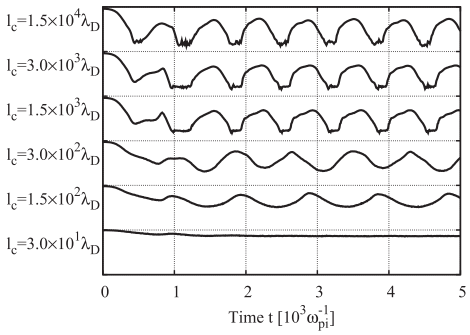

FIG. 15. Diode currents for different electron neutral collisions. The imposed collisional mean free path ℓ_c is indicated at each curve. The ions are here collisionless.

and an additional slowing down of the electrons due to the collisions is merely enhancing the local excess of electrons there. The temperature of the scattering neutrals has little effect in this context.

While Fig. 14 is a summary plot, we show in Fig. 15 the detail of the effect of elastic collisions of electrons and neutrals. As long as the collisional mean free path is longer than $\mathcal{L}$ as in the three top traces in Fig. 15, the collisions have modest effect, but as the collisions become more abundant, the frequency of the oscillations decreases slowly with decreasing collisional mean free path. At the same time the amplitude decreases to be almost indiscernible when the mean free path is approximately $\mathcal{L}/30$. At this stage the electron mobility is low, and the local electron density becomes large in front of the emitting surface. For the shortest mean free paths in Fig. 14, we observe the transient formation of an ion phase space vortex.[36,37] The life time of these vortices seems to increase with decreasing collisional mean free paths. If we decrease the collision mean free path even further, we find a new type of small amplitude oscillations with a frequency that is higher than seen in Fig. 14: these oscillations are due to the mobile ions.

Ion collisions are effective in modifying the diode; charge exchange collisions are more effective than elastic ion collisions. To gain some insight into the details of the elastic ion collision processes, we determined an estimate for the joint probability density $P(E_1, E_2)$, where E_1 is the ion energy at the beginning of a mean free collision path and E_2 the energy of the ion at the next collision time. The analysis does not discriminate the positions of the collisional ion. The marginal distributions $P(E_1)$ and $P(E_2)$ are obtained by projecting $P(E_1, E_2)$ on the E_1 and E_2 planes. We found that approximately we have $P(E_1, E_2) \approx P(E_1)P(E_2)$, indicating that to a good approximation we can assume E_1 and E_2 to be statistically independent. This means that the collective electric fields are just as effective as the elastic collisions in randomizing the ion energies. The main characteristics of the oscillations with significant charge exchange collisions (traces "CE" in Fig. 14) is a decrease in the oscillation period (for elastic

collisions, this has been observed also experimentally[2,38]), together with a distortion of the form of the oscillations, that becomes "saw-tooth" like. When all collisional effects are activated (see the trace labelled "ALL" in Fig. 14), we find that the saw-tooth feature is still there but now with a "tilt" to the opposite side, thus demonstrating that the temporal form of the oscillations is sensitive to the nature of the collisions. The results presented in Fig. 14 include the initial transient part of the oscillations: we note significant modifications also in this part when we compare with the reference collisionless case.

When the collisional charge exchange drag on the ions is large, we find the formation of a positive space charge layer near $x = 0$, and the diode oscillations are modified. Details in the propagation characteristics in the space-time varying potential found in Fig. 5 disappear. Charge exchange collisions are more effective than elastic collisions in slowing down the ions, and charge exchange collisions with a cold neutrals are more effective than similar collisions with warm neutrals. All these observations are consistent with the results summarized in Fig. 14. If we take the neutral gas temperature to be very low, we find that the ion component can develop two distinct populations[39]: one being the part accelerated through the potential drop at the sheath having not yet collided, and a part formed by the charge exchange collisions and appearing as a cold component with no drift velocity. In this case we can have a kinetic ion-ion instability developing.[40] This result has interest only for very low temperatures T_n and is not elaborated further here. For very high ion collision rates the ion mobility becomes low, but the oscillations can be maintained by the electron dynamics alone, as for a Pierce diode[41] provided the conditions on geometry and end-plate bias are fulfilled. For such low ion mobilities, the average ion distribution will be non-uniform.

The almost linear scaling between oscillation period and the length of the system (shown in Fig. 3) remains valid also when we have significant amounts of collisions, but the frequency is now noticeably reduced and we have $f_0 \approx C_s/2\mathcal{L}$; see results given by squares in Fig. 3, where a full line gives the sound speed, and dotted line is the best fit to the data (squares). The difference is minute.

In Video 3 (see Fig. 16) we show the space-time variation of the diode, giving the potential as well as the phase-space information for the case where $T_n = 0.15\,T_0$. We initiate the simulation with no collisions and let the mean free path be slowly decreasing until it reaches a value slightly smaller than the one used for Fig. 14. We have $\ell_c \sim 1/t$ so that the average collision frequency becomes approximately proportional to time. The effects of charge exchange collisions begin to be noticeable when the collisional mean free path is approximately $\mathcal{L}/2$. The formation of the cold ion population due to the charge exchange processes is clearly seen in ion phase space. The results should be compared to the free oscillations shown in Video 1 (Fig. 2). Note that the number of ions reflected at the end plate is strongly reduced for the case with charge exchange collisions. The

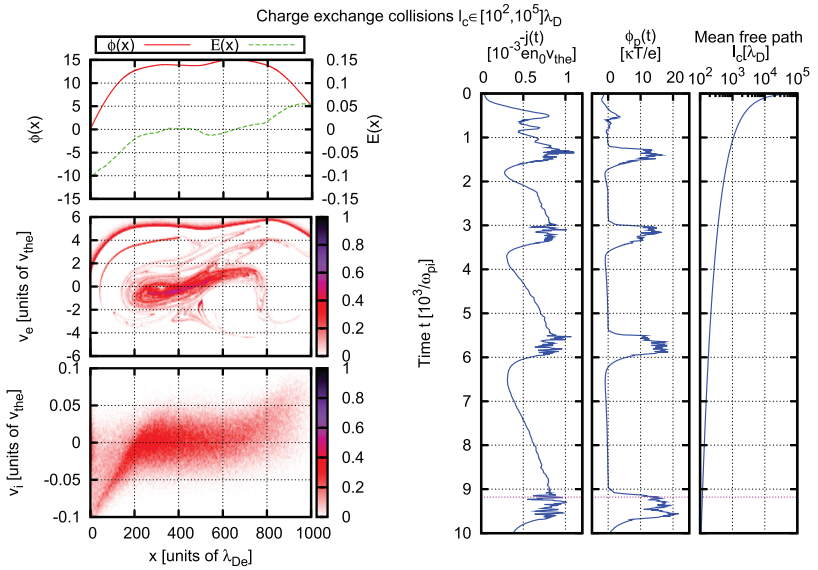

FIG. 16. Summary figure for Video 3, showing also the phase space dynamics. The simulations model the case where the ion charge exchange collisional mean free path decreases with time as shown in the third frame to the right. See Fig. 2 for a detailed description of the set-up (enhanced online) [URL: http://dx.doi.org/10.1063/1.4747620.3].

propagating double layer structure is not significant with charge exchange collisions, but the basic characteristics of the diode oscillations remain, albeit with reduced frequency and distorted temporal form of the oscillations. In Video 3 (Fig. 16) we show in the rightmost panel also the electrostatic potential as detected at a position $x = \mathcal{L}/2$. At this position we find localized potential enhancements with long quiescent time intervals in between, where all of the potential drop in the diode is found at the end sheath.

Also with collisions included, we find that the diode retains the basic properties of a van der Pol oscillator. For illustration we show in Fig. 17 the diode performance with external forcing of a diode where the ions have charge exchange collisions where $\ell_c = 150\lambda_D$. The top trace shows the diode current, the next frame is the potential applied to the end-plate. The third frame from the top gives the plasma potential in the central position of the diode, while the bottom frame gives the wavelet transform of the current. A dashed line gives for reference the natural frequency of the diode without collisions and constant positive end-plate potential. When the externally applied frequency is near the collisional diode frequency, we observe the frequency pulling in the wavelet transform of the diode current. When the difference between the natural and applied frequencies is large, we find that the oscillations return to the frequency of the constant bias diode. These low frequency oscillations modulate the high frequency applied signal resulting in bursts or "packets" of high frequency signals, most clearly observed in the wavelet transform. We note a similarity with the corresponding results in Fig. 13 for a collisionless diode.

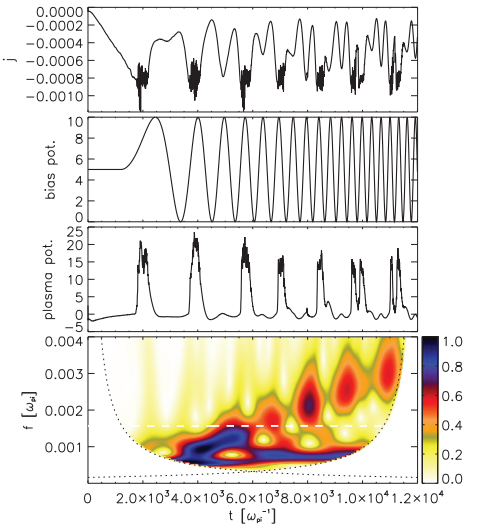

FIG. 17. External forcing of a diode with ions have charge exchange collisions where $\ell_c = 150\lambda_D$. The top trace shows the diode current, the next frame is the potential applied to the end-plate (see also Fig. 13). The third frame from the top gives the plasma potential in the central position of the diode, while the bottom frame gives the wavelet transform of the current. A dashed line gives for reference the natural frequency of the diode without collisions and constant positive end-plate potential.

VII. DISCUSSIONS

In the present study we analyzed the properties of a simple plasma diode with emphasis on the conditions with forcings applied either to the boundary of the plasma or internally by introducing either variable test charges or particle absorption. We compared the properties of the diode with solutions of the van der Pol equation. It was found that for the unperturbed oscillation, i.e., without applied forcing, a very good agreement could be found. Extending the analysis to the externally forced diode we found qualitative agreement in the sense that some basic features of the van der Pol equation could be recovered, but here it was important to specify the means of external excitation. The most effective excitation turned out to be one corresponding to an absorbing grid immersed in the plasma column. Incidentally, this method was used by some of the early investigations of the diode performance.[28] Velocity modulation by a localized electric field had a much smaller effect in comparison.

Another method of diode perturbation consists of applying a variable, externally controlled, potential to the end plate. We analyzed also this method and found that in this case elements of the results from a perturbed van der Pol equation could be recovered. It was, however, necessary to apply external amplitudes comparable to the DC bias, an observation which is after all also intuitively reasonable. This latter method of excitation is the one that comes closest to giving results similar to those found by solving the van der Pol equation with external forcing. We find, however, the similarities of the results to be more interesting than the differences: the two very different methods of excitation both reproduce the periodic pulling and mode stabilization features found in the van der Pol model.

The excitation obtained by modulating the end plate bias corresponds to applying an ideal voltage generator,[20] i.e., one that maintains a potential irrespective of the load. The case where the end plate voltage is modulated can be modeled by a dc-generator in series with a variable generator, both elements considered ideal. The alternative ideal generator used in lumped electrical circuits, the ideal current generator (one that maintains the current irrespective of the load), is not readily realized experimentally and therefore not studied here. As a first approximation it can be argued that the modulation of the ion flux passing a reference position as described in Sec. V B is equivalent to a current modulation. Such a model can be taken only as an approximation, however, since the efficiency depends on the position of the excitation along the axis of the device as evidenced by Fig. 11.

The most significant difference between the diode simulations and the numerical solutions for the van der Pol equation lies in the second and third harmonic generation. These were much more significant in the numerical simulations of the diode, and we conclude that the nonlinear term in the van der Pol model has to be elaborated for a better agreement and

found also that a simple addition of terms with exponents exceeding 2 is not sufficient. We found numerical confirmations also of experimentally observed propagating double layers.[23] Details concerning the ion population are not readily revealed experimentally, and numerical simulations like those presented here are necessary for a complete understanding. The internal modulations destroy the propagating double layer, and the stabilization of the van der Pol oscillations for that case is in part due to this effect. When the applied frequency is very high compared to the natural frequency, the perturbation reduces to a local modulation of the plasma density, where the oscillating diode returns approximately to its original state with a DC-bias.

In all cases we found that large forcing amplitudes have to be applied to the system in order to recover solutions resembling those characterizing a van der Pol oscillator. We tried various modifications of the basic van der Pol equation to make its solutions closer to observations but found that minor modifications are insufficient. Terms containing $d\xi/dt$ as well as ξ in the bracket of the nonlinear term of (4) were tried.

The effect of collisions was discussed in Sec. VI. Several types of collisions were studied. We found that charge exchange collisions were particularly effective in modifying the oscillation characteristics of the diode, with results summarized in Figs. 3 and 14. Charge exchange collisions usually have the largest cross sections and are physically the most relevant. The most important observation regarding the oscillation characteristics of the diode with collisions seem to be a pronounced reduction in oscillation frequency. Also, a change in shape of the signal is noted: the current becomes more "saw-tooth like," with an increased harmonic content with collisional ions, while electron collisions on the other hand give smoother signals, with less harmonic content. For the collisionless diode we find that the growth of the large amplitude perturbation begins at the sheath near the end plate, and progresses rapidly into the main plasma (see Video 1 (Fig. 2)). For the collisional diode, with the parameters studied here, the perturbation begins at the plasma emitting plate to propagate rapidly into the main plasma, see Video 3 (Fig. 16). Our three videos offer detailed insight into the phase space dynamics of ions as well as electrons. The general space-time characteristics of the oscillations are changed, e.g., details in the double layer like structure shown in Fig. 4 are lost.

ACKNOWLEDGMENTS

The work was supported in part by a grant from the Norwegian National Science Foundation. We thank Dr. Wojciech Miloch for his interest and for many valuable discussions on numerical problems.

APPENDIX: DETAILS OF THE COLLISION ALGORITHM

The numerical collision model developed for the present study is based on a Monte Carlo collision (MCC) model for PIC simulation codes and is directly based upon previous works.[42,43] While traditional collision models[44,45] calculate the time between collisions for each particle, the MCC-PIC package generalizes these calculations to allow for more efficient algorithms.

The collision algorithm is based on the null-collision methodology. Instead of entering the rather time-consuming evaluation of cross section $\sigma(E)$ or equivalently collision frequency $\nu(E)$ for each simulation particle at each time step, a maximum collision frequency $\nu_{\max}$ is introduced for each particle species

$$\nu_{\max} \equiv \max_E\Big(\sum_s \nu_s(E)\Big), \tag{A1}$$

where $\nu_s(E)$ is the collision frequency of type s for the given specie. Potential candidates for collision events during the time interval Δt are now draw with probability $P = 1 - \exp(-\nu_{\max}\Delta t)$. For these candidates *only* the exact evaluation of $\nu(E)$ is performed. A fraction $\nu(E)/\nu_{\max}$ of the potential candidates drawn are then subjected to an actual collision event. The remaining fraction suffer a "null-collision," that is they avoid collisions in the given time interval Δt.

The current model allows for both elastic and inelastic scattering and charge exchange collisions, for any arbitrary combination of particle species, with input parameters as cross sections, scattering angles, and VDF's of the target species given. Cross section and scattering angles are generally given as functions of kinetic energy in a centre-of-mass reference system.

The present study is restricted to constant cross sections and isotropic scattering. Realistic scattering cross sections that vary with energy and which may differ significantly from one species to another can be readily introduced. For the illustration intended with the present analysis we find that constant cross sections and, thereby, constant mean free paths will suffice. Taking the cross section to be constant, independent of energy, allows us to use a constant mean free path for all particles.

[1]R. W. Motley, *Q Machines* (Academic, New York, 1975).
[2]T. Klinger, F. Greiner, A. Rohde, and A. Piel, "Nonlinear dynamical behavior of thermionic low-pressure discharges. 2. Experimental," Phys. Plasmas **2**, 1822–1836 (1995).
[3]I. Langmuir and K. H. Kingdon, "Thermionic effects caused by vapors of alkali metals," Proc. R. Phys. Soc. Ser. A **107**, 61–79 (1925).
[4]H. B. Michaelson, "The work function of the elements and its periodicity," J. Appl. Phys. **48**, 4729–4733 (1977).
[5]F. Bauer and H. Schamel, "Spatiotemporal structures in collisionless electrostatic plasmas," Physica D **54**, 235–252 (1992).
[6]S. Kuhn, "Determination of axial steady-state potential distributions in collisionless single-ended Q-machines," Plasma Phys. **21**, 613–626 (1979).
[7]T. L. Crystal, P. C. Gray, W. S. Lawson, C. K. Birdsall, and S. Kuhn, "Trapped-electron effects on time-independent negative-bias states of a collisionless single-emitter plasma-device-theory and simulation," Phys. Fluids B-Plasma Phys. **3**, 244–254 (1991).
[8]T. Seo, J. C. I. Kim, and S. J. Hahn, "Nonlinear dynamical behaviors in a magnetized plasma diode system," J. Phys. Soc. Jpn. **80**, 034501 (2011).
[9]V. I. Kuznetsov, A. Ya. Ender, and S. Kuhn, "Collisionless self-consistent trapping of electrons into a nonstationary potential well: Dynamics of trapped electrons," Tech. Phys. **51**, 1257–1268 (2006).
[10]V. I. Babanin, I. N. Kolyshkin, V. I. Kuznetsov, A. S. Mustafaev, V. I. Sitnov, and A. Y. Ender, "Optimization of a Knudsen Cs-Ba thermionic converter," Sov. Phys. Tech. Phys. **223**, 444–766 (1978); "Optimization of a Knudsen Cs-Ba thermionic converter," Z. Tech. Fiz. **48**, 754–766 (1978).
[11]T. Gyergyek, M. Čerček, and M. Stanojević, "Experimental evidence of periodic pulling in a weakly magnetized discharge plasma column," Contrib. Plasma Phys. **37**, 399–416 (1997).

[12]H. Lashinsky, "Turbulence in Fluids and Plasmas," Microwave Research Institute Symposia Series, Vol. **18** (Polytechnic, Polytechnic Institute of Brooklyn, NY, 1969).
[13]T. Klinger, F. Greiner, A. Rohde, A. Piel, and M. E. Koepke, "van der Pol behavior of relaxation oscillations in a periodically driven thermionic discharge," Phys. Rev. E **52**, 4316–4327 (1995).
[14]K. H. Pae and S. J. Hahn, "Self-oscillation and chaos in positive-bias plasma diodes," J. Phys. Soc. Jpn. **71**, 2169–2173 (2002).
[15]A. Piel, F. Greiner, T. Klinger, N. Krahnstover, and T. Mausbach, "Chaos and chaos control in plasmas," Phys. Scr. T **84**, 128–131 (2000).
[16]A. Ya. Énder, H. Kolinsky, V. I. Kuznetsov, and H. Schamel, "Collective diode dynamics: An analytical approach," Phys. Rep. **328**, 1–72 (2000).
[17]V. I. Kuznetsov, A. Ya. Énder, H. Schamel, and P. V. Akimov, "Switching of nonneutral plasma diodes. I. Analytic theory," Phys. Plasmas **11**, 3212 (2004).
[18]V. I. Kuznetsov, A. Ya. Énder, H. Schamel, and P. V. Akimov, "Switching of nonneutral plasma diodes. II. Numerical results," Phys. Plasmas **11**, 3224 (2004).
[19]Y. A. Énder, V. I. Kuznetsov, and H. Schamel, "Theory and application of plasma diode equilibria with beam electrons and a fixed particle background of negative charge," EPJ.-Appl. Phys. **49**, 11002 (2010).
[20]F. Greiner, T. Klinger, and A. Piel, "Nonlinear dynamical behavior of thermionic low-pressure discharges. 1. Simulation," Phys. Plasmas **2**, 1810–1821 (1995).
[21]F. F. Chen, *Introduction to Plasma Physics and Controlled Fusion*, 2 ed. (Plenum, New York, 1984), Vol. 1.
[22]M. A. Lieberman and A. J. Lichtenberg, *Principles of Plasma Discharges and Materials Processing* (John Wiley & Sons, Inc., New York, 1994).
[23]S. Iizuka, P. Michelsen, J. J. Rasmussen, R. Schrittwieser, R. Hatakeyama, K. Saeki, and N. Sato, "Dynamics of a potential barrier formed on the tail of a moving double-layer in a collisionless plasma," Phys. Rev. Lett. **48**, 145–148 (1982).
[24]T. Klinger and A. Piel, "Investigations of attractors arising from the interaction of drift waves and potential relaxation instabilities," Phys. Fluids B **4**, 3990–3995 (1992).
[25]C. K. Birdsall and A. B. Langdon, *Plasma Physics via Computer Simulation* (McGraw-Hill, New York, 1985).
[26]P. Burger, "Theory of large-amplitude oscillations in 1-dimensional low-pressure cesium thermionic converter," J. Appl. Phys. **36**, 1938–1943 (1965).
[27]J. E. Crow, P. L. Auer, and J. E. Allen, "Expansion of a plasma into a vacuum," J. Plasma Phys. **14**, 65–76 (1975).
[28]P. Michelsen, H. L. Pécseli, J. J. Rasmussen, and R. Schrittwieser, "Current-driven, ion-acoustic instability in a collisionless plasma," Plasma Phys. Controlled Fusion **21**, 61–73 (1979).
[29]H. Schamel, "Electron holes, ion holes and double layers," Phys. Rep. **140**, 161–191 (1986).
[30]S. Mallat, *A Wavelet Tour of Signal Processing* (Academic, California, 1998).
[31]R. W. Gould, "Excitation of ion-acoustic waves," Phys. Rev. **136**, A991–A997 (1964).
[32]P. Michelsen and H. L. Pécseli, "Propagation of density perturbations in a collisionless Q-machine plasma," Phys. Fluids **16**, 221–225 (1973).
[33]Y. Itikawa, "Effective collision frequency of electrons in gases," Phys. Fluids **16**, 831–835 (1973).
[34]S. A. Andersen, V. O. Jensen, and P. Michelsen, "Charge-exchange cross-sections measured at low energies in Q machines," Rev. Sci. Instrum. **43**, 945–947 (1972).
[35]R. Ya. Kucherov, Z. A. Oganezov, L. S. Timoshenko, and V. K. Tskhakaya, "Electric field distribution in a Knudsen plasma," Sov. J. Plasma Phys. **15**, 766–771 (1989).
[36]H. L. Pécseli, R. Armstrong, and J. Trulsen, "Experimental observation of ion phase-space vortices," Phys. Lett. A **81**, 386–390 (1981).
[37]H. L. Pécseli, J. Trulsen, and R. Armstrong, "Formation of ion phase-space vortexes," Phys. Scr. **29**, 241–253 (1984).
[38]I. G. Gverdtsiteli, V. Ya. Karakhanov, E. A. Kashirskii, R. Ya. Kucherov, and Z. A. Oganezov, "Mechanism of flow oscillations in Knudsen cesium diode," Sov. Phys. Tech. Phys. **17**, 78–84 110 (1972); "Mechanism of flow oscillations in Knudsen cesium diode," Z. Tech. Fiz. **42**, 103–84 110 (1972).
[39]S. Børve, H. L. Pécseli, J. Trulsen, and S. Longo, "Kinetic instabilities associated with injection of a plasma beam into a neutral background," Phys. Scr. **T122**, 125–128 (2006).
[40]B. D. Fried and A. Y. Wong, "Stability limits for longitudinal waves in ion beam-plasma interaction," Phys. Fluids **9**, 1084–1089 (1966).
[41]J. R. Pierce, "Limiting stable current in electron beams in the presence of ions," J. Appl. Phys. **15**, 721–726 (1944).
[42]V. Vahedi and M. Surendra, "Monte Carlo collision model for the particle-in-cell method: Applications to argon and oxygen discharges," Comput. Phys. Commun. **87**, 179–198 (1995).
[43]C. K. Birdsall, "Particle-in-cell charged-particle simulations, plus Monte Carlo collisions with neutral atoms," IEEE Trans. Plasma Sci. **19**, 65–85 (1991).
[44]E. W. McDaniel, *Atomic Collisions: Electron and Photon Projectiles* (Wiley, New York, 1989).
[45]E. W. McDaniel, J. B. A. Mitchell, and M. E. Rudd, *Atomic Collisions: Heavy Particle Projectiles* (Wiley, New York, 1993).

Paper II

II

Self-similar evolution of an initial density discontinuity

V. L. Rekaa, H. L. Pécseli and J. K. Trulsen
Physics of Plasmas, **20**, 072117 (2013)

PHYSICS OF PLASMAS 20, 072117 (2013)

Self-similar space-time evolution of an initial density discontinuity

V. L. Rekaa,[1,a)] H. L. Pécseli,[1,b)] and J. K. Trulsen[2,c)]
[1]Department of Physics, University of Oslo, Box 1048 Blindern, N-0316 Oslo, Norway
[2]Institute of Theoretical Astrophysics, University of Oslo, Box 1029 Blindern, N-0315 Oslo, Norway

(Received 16 April 2013; accepted 3 July 2013; published online 31 July 2013)

The space-time evolution of an initial step-like plasma density variation is studied. We give particular attention to formulate the problem in a way that opens for the possibility of realizing the conditions experimentally. After a short transient time interval of the order of the electron plasma period, the solution is self-similar as illustrated by a video where the space-time evolution is reduced to be a function of the ratio x/t. Solutions of this form are usually found for problems without characteristic length and time scales, in our case the quasi-neutral limit. By introducing ion collisions with neutrals into the numerical analysis, we introduce a length scale, the collisional mean free path. We study the breakdown of the self-similarity of the solution as the mean free path is made shorter than the system length. Analytical results are presented for charge exchange collisions, demonstrating a short time collisionless evolution with an ensuing long time diffusive relaxation of the initial perturbation. For large times, we find a diffusion equation as the limiting analytical form for a charge-exchange collisional plasma, with a diffusion coefficient defined as the square of the ion sound speed divided by the (constant) ion collision frequency. The ion-neutral collision frequency acts as a parameter that allows a collisionless result to be obtained in one limit, while the solution of a diffusion equation is recovered in the opposite limit of large collision frequencies. © *2013 AIP Publishing LLC*. [http://dx.doi.org/10.1063/1.4816953]

I. INTRODUCTION

A classic dynamic problem in studies of plasma phenomena concerns the space-time evolution of an initial step-like discontinuity of the plasma density. A special limiting case is where plasma expands into vacuum.[1–3] The problem is interesting also for practical reasons: analytical and numerical studies often assume an initial condition to be given, while many laboratory experimental conditions assume some given boundary conditions. A comparison between analytical and experimental results is not always simple in such cases.[4] The step-like initial condition is one that can be realized by an absorbing grid in a streaming plasma, as found in, for instance, a single ended Q-machine.[5–7] Two time scales can be distinguished: first, an initial expansion of the electron component, where the electric field develops due to the charge imbalance caused by the electron pressure. Inertia makes the ion motion negligible on this time scale. Later, we find a slow expansion of the entire bulk plasma density, where also the ions are set into motion by the collective electric fields. The basic elements of the problem can be understood even in a spatially one dimensional analysis, and only this case will be considered here: physically it corresponds to the low frequency dynamics in a strongly magnetized Q-machine plasma, for instance.

A complete understanding of the ion dynamics requires information of the velocity distribution $f(x,u,t)$ for ions with velocities u, at positions x at times t, as described by the ion Vlasov equation for ions with mass M and charge e

$$\frac{\partial}{\partial t}f + u\frac{\partial}{\partial x}f - \frac{e}{M}\frac{\partial\phi}{\partial x}\frac{\partial}{\partial u}f = 0, \tag{1}$$

where $E \equiv -\partial\phi/\partial x$ is the electric field and ϕ is the electrostatic potential. The ion density is $n_i = \int_{-\infty}^{\infty} f\,du$. For the relevant low-frequency dynamics, we can safely assume the electrons to be Boltzmann distributes at all times, so that the electron dynamics are accounted for by the relation $n_e = n_0\exp(e\phi/T_e)$, where T_e is the electron temperature.

For times exceeding the ion plasma period, $t \gg 2\pi/\omega_{pi}$, with ω_{pi} being the ion plasma frequency, and at large scale lengths, we can assume that the plasma dynamics are quasi-neutral, $n_e \approx n_i \equiv n$. In this limit, the Debye length no longer enters the problem, and we have neither constant characteristic length nor time scales in the dynamic equations. (All we have is a velocity, the ion sound speed $C_s = \sqrt{T_e/M}$ derived from the electron temperature.) For such cases, the characteristic scales are determined solely by initial or boundary conditions. Under these conditions, we can expect the plasma dynamics to evolve self-similarly, in depending functionally on the ratio $\zeta \equiv x/t$ rather than on x and t independently,[8–12] giving $\partial/\partial t \to -t^{-2}x\partial/\partial\zeta = -t^{-1}\zeta\partial/\partial\zeta$ and $\partial/\partial x \to t^{-1}\partial/\partial\zeta$. Heaviside's step function or the δ-function are examples of functions without length scales. We thus assume an initial step-like density perturbation. By introducing the variable $\zeta \equiv x/t$, we can then reduce Eq. (1) to

$$(u-\zeta)\frac{\partial}{\partial\zeta}f - \frac{T_e}{M}\frac{1}{n}\frac{\partial n}{\partial\zeta}\frac{\partial}{\partial u}f = 0, \tag{2}$$

a)Electronic mail: v.l.rekaa@fys.uio.no
b)Electronic mail: hans.pecseli@fys.uio.no
c)Electronic mail: j.k.trulsen@astro.uio.no

after a little algebra, where we now have $f = f(\zeta, u)$ and $n = n(\zeta) \equiv \int_{-\infty}^{\infty} f(\zeta, u) du$. The collective electric field was determined by the assumption of Boltzmann distributed electrons, giving $n = n_0 \exp(e\phi/T_e)$. From Eq. (2), we have the relation

$$f(u,x,t) = \begin{cases} G_-(u) + C_s^2 \int_{-\infty}^{x/t} \frac{1}{n}\frac{\partial n}{\partial \zeta}\frac{\partial f/\partial u}{u-\zeta} d\zeta & \text{for } x/t < u, \\ G_+(u) - C_s^2 \int_{x/t}^{\infty} \frac{1}{n}\frac{\partial n}{\partial \zeta}\frac{\partial f/\partial u}{u-\zeta} d\zeta & \text{for } x/t > u, \end{cases} \tag{3}$$

where $G_-(u) \equiv f(x \to -\infty, u)$, $G_+(u) \equiv f(x \to +\infty, u)$. With the present assumptions, we have $G_-(u) = (n_0 + \Delta n) f_0(u)$ and $G_+(u) = n_0 f_0(u)$, where we for simplicity introduced the unperturbed velocity distribution in the form $n_0 f_0(u)$ with the normalization $\int_{-\infty}^{\infty} f_0(u) du = 1$. This form turns out to be convenient when we linearize the equations. The self-similarity of the solutions can also be understood by identifying a dynamic length-scale $\ell \equiv C_s t$. The self-similar variable is then recovered by the normalized length $x/\ell \sim x/t$.

The assumption of Boltzmann distributed isothermal electrons is standard for low frequency, long wave-length perturbations and is obtained analytically by ignoring the electron inertia. In this limit, the electron thermal conductivity in effect becomes infinite, and a constant T_e can be argued by a constant electron temperature reservoir present at $|x| \to \infty$ In the model assumed here, the energy for accelerating the ions originates from the ambipolar electric field build-up by the electron pressure. The constant electron temperature reservoir thus serves as a constant energy source. The argument assumes implicitly that no local potential maxima develops, where electrons can be trapped[13] with a velocity distribution deviating from the assumed Maxwellian. We find that for our problem the ion Landau damping is smoothing out small scale potential variations (the "Airy function ripples") so we have a monotonically varying plasma density as long as $T_e/T_i \leq 5$, and with this temperature restriction, the analysis is self-consistent.

In the present paper, we study the space-time evolution of a step-like initial condition for the plasma density, with particular attention to the self-similarity of the evolution. We study (both analytically and numerically) the problem under conditions that can be realized in a laboratory experiment, such as a single ended Q-machine.[14] The electron temperature is here determined by the hot end-plate of the device.

.The first part of the analysis considers collisionless plasmas. If a neutral gas is introduced, we will have ion-neutral and electron-neutral collisions modifying the dynamics. Since the basic analysis assumes the electrons to be isothermally Boltzmann distributed at all times, we do not expect electron collisions to give significant modifications of the results. Inclusion of ion-neutral collisions on the other hand introduces a new length scale, the mean free collision length, ℓ_c, and we want to analyze how this new feature modifies the self-similar evolution.

If we take the temperature of the neutral gas at rest to be very low, we find that the ion component can develop two distinct populations:[15] one being the part of the ions accelerated through the potential drop at the boundary and having not yet collided, and a part formed by the charge exchange collisions and appearing as a cold component with no drift velocity. In this case, we can have an ion velocity distribution developing that is unstable to kinetic ion-ion instabilities.[16] This result has interest only for very low neutral temperatures and is not elaborated further here.

The paper is organized as follows: in Sec. II, we present results from an exact solution of the linearized version of Eq. (3) and compare it with numerical results in Sec. III. In Sec. IV, we extend the analysis to include collisions, using a model best suited for charge exchange collisions although we use a constant collision frequency, independent of velocity, to simplify the analysis. Corresponding numerical results are shown in Sec. V. Sections III and V present results from numerical Particle in Cell (PIC) simulations of the problem. The theoretical analysis uses a Maxwellian velocity distribution as a reference since many integrals can be expressed by the plasma dispersion function. The numerical simulations address a physically realizable situation where the velocity distribution evolves by a simulated plasma production at the boundary. Section VI contains our discussions and conclusions.

II. LINEARIZED MODEL

In many cases, an initial value problem can be formulated only in a formal way; it is rather difficult to imagine how to set up an initially prescribed density variation over all space. There are of course several realizable and nontrivial examples, which are interesting for experimental tests of the results. Here, we consider the one dimensional case, where the initial perturbation consists of a step in the ion velocity distribution at $t = 0$ giving $(n_0 f_0(u) + \Delta n g(u))$ for $x < 0$ and $n_0 f_0(u)$ for $x > 0$, with $\Delta n \ll n_0$ and $\int_{-\infty}^{\infty} f_0(u) du = 1$. The analysis allows in principle for having a perturbation of the ion velocity distribution function $\Delta n\, g(u) \neq \Delta n f_0(u)$, but we do not make use of this additional freedom of choice here.[5,17]

The space-time variation of the perturbation of the ion velocity distribution function can be obtained by linearizing Eq. (3) to give

$$\frac{f_1(u,x,t)}{\Delta n} = \begin{cases} f_0(u) - C_s^2 f_0'(u) \int_{-\infty}^{x/t} \frac{h_0(\gamma)}{u-\gamma} d\gamma, & \text{for } x/t < u, \\ C_s^2 f_0'(u) \int_{x/t}^{\infty} \frac{h_0(\gamma)}{u-\gamma} d\gamma, & \text{for } x/t > u, \end{cases} \tag{4}$$

with $C_s^2 \equiv T_e/M$ and $n_1(x,t) \equiv \int_{-\infty}^{\infty} f_1(u,x,t) du$. The distribution function $f_1(u,x,t)$ has an integrable singularity for $x/t = u$. There are no singularities for the integrations in Eq. (4). We introduced $h_0(\zeta) \equiv -d(n_1(\zeta)/\Delta n)/d\zeta$ for simplicity. After some algebra[5,18] (see also Sec. IV A), we find for linearly stable plasmas

$$h_0(\gamma) \equiv \frac{1}{\pi} \Im \left\{ \left(P \int_{-\infty}^{\infty} \frac{f_0(u)}{u-\gamma} du + i\pi f_0(\gamma) \right) \times \left(1 - C_s^2 P \int_{-\infty}^{\infty} \frac{f_0'(u)}{u-\gamma} du - i\pi C_s^2 f_0'(\gamma) \right)^{-1} \right\}, \tag{5}$$

where $\Im\{\}$ denotes the imaginary part of the expression in the brackets $\{\}$, and $P\int$ denotes the principal value of the integral. We illustrate $h_0(\gamma)$ in Fig. 1 for the reference case of $f_0(u)$ being a Maxwellian. Here, we can introduce the plasma dispersion function[19] and obtain $h_0(\gamma)$ analytically. In particular, for $T_e = 0$ we find $h_0(\gamma) = f_0(\gamma)$, giving the free streaming results as for a Knudsen gas. In the present quasi-neutral limit, charge separations are completely shielded by cold electrons, and the entire plasma dynamics is then controlled by the ion pressure.

The analytically obtained velocity distribution function $f_1(u,x,t)$ has to be added to the background distribution $f_0(u)$, so it is not unphysical to have $f_1(u,x,t) < 0$. The singularity at $u = x/t$ is an artifact resulting from the linearization together with the idealized initial condition consisting of a Heaviside step-function.

The space-time evolution of the perturbation in ion density is obtained as

$$n_1(x,t) = \Delta n \int_{x/t}^{\infty} h_0(\gamma) d\gamma, \tag{6}$$

while the corresponding perturbation of the ion flux $F_1(x,t)$ is obtained from the ion continuity equation in the general self-similar form

$$-\zeta \frac{\partial n}{\partial \zeta} + \frac{\partial F}{\partial \zeta} = 0. \tag{7}$$

Inserting Eq. (6), we find

$$F_1(x,t) = \Delta n \int_{x/t}^{\infty} \gamma h_0(\gamma) d\gamma. \tag{8}$$

The density as well as the ion flux evolves self-similarly in the present limit for any velocity distribution $f_0(u)$, just as the perturbation of the ion velocity distribution function.[3,5,8,9]

We presented linear analytical results for the density, ion flux, and average ion velocity. More generally, the linearized version of Eq. (2) gives

$$(u-\zeta)\frac{\partial}{\partial \zeta} f_1 - C_s^2 \frac{\partial n_1}{\partial \zeta} f_0'(u) = 0. \tag{9}$$

Inserting Eq. (6), we can also obtain more complicated expressions, such as

$$\int_{-\infty}^{\infty} u^2 f_1(u,x,t) du = \Delta n \left(\int_{-\infty}^{\infty} u^2 f_0(u) du + \int_{-\infty}^{x/t} (C_s^2 - \gamma^2) h_0(\gamma) d\gamma \right), \tag{10}$$

found by multiplying Eq. (9) with u and integrating. A term containing $\int_{-\infty}^{\infty} u f_1 du$ is rewritten by use of Eq. (8). An integration constant is given by $\int_{-\infty}^{\infty} u^2 f_1(u,x,t) du \to \Delta n \int_{-\infty}^{\infty} u^2 f_0(u) du$ for $x/t \to -\infty$. Recall that $f_1(u,x,t)$ represents a deviation from $f_0(u)$ and can take negative values also.

The analytical form (6) is shown in Fig. 2(a) for two temperature ratios $T_e/T_i = 3$ and $T_e/T_i = 6$, for a reference Maxwellian ion distribution with no drift velocity. In the density evolution, we can distinguish the forward propagating signal and the backward moving rarefaction wave. At the origin, we have at all times $n_1 = \frac{1}{2}\Delta n$ for symmetry reasons. Note that the rarefaction wave prevails also in the limit of

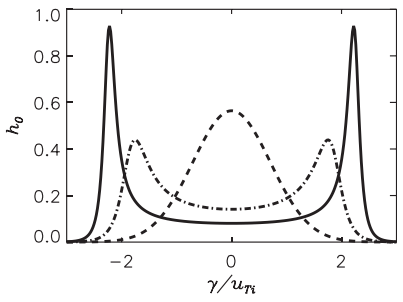

FIG. 1. Illustration of the function $h_0(\gamma/u_{Ti})$ as given by Eq. (5), here shown for the reference case where $f_0(u)$ is a Maxwellian with no drift velocity. The normalizing velocity is defined as $u_{Ti} = \sqrt{2T_i/M}$. Results are shown for two temperature ratios, $T_e/T_i = 6$ (full line) and $T_e/T_i = 3$ (dotted-dashed line). For reference, we show also the result for $T_e = 0$ with a dashed line. The area covered by the three curves is the same.

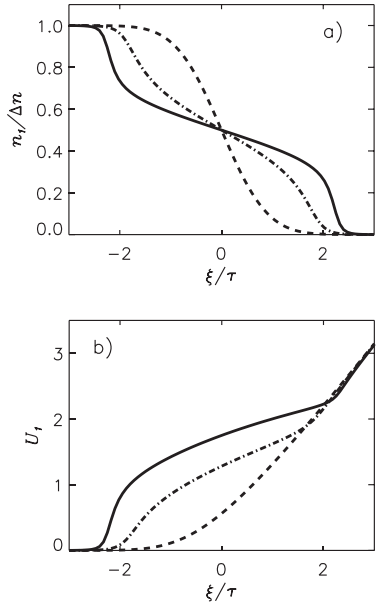

FIG. 2. Illustration in (a): The analytical expression for the evolution of the self-similar normalized density $n_1/\Delta n$ for two temperature ratios, $T_e/T_i = 6$ (full line) and $T_e/T_i = 3$ (dotted-dashed line). The corresponding normalized average ion velocities U_1 are shown in (b). The results are obtained by integrations involving the h_0-function shown in Fig. 1. The ion velocity distribution is here taken to be a Maxwellian with no average drift velocity. For reference, we show also the free streaming Knudsen gas results with dashed lines.

freely streaming ions, i.e., for $T_e = 0$ for instance with a Maxwellian $f_0(u)$. As the electron-ion temperature ratio increases, we note a steepening of the density variation. For the free streaming solution, we find a constant sign for the curvature for $x/t > 0$ and $x/t < 0$, respectively. For the two temperature ratios shown, we note a change in curvature in the two ranges mentioned. The separating case is $T_e/T_i = 1$. For $T_e/T_i \to \infty$, the forward and backward propagating signals will approach the step-functions found by the corresponding fluid analysis. Due to the assumption of Boltzmann distributed electrons, the density perturbation is directly proportional to the electrostatic potential in the present small amplitude, quasi-neutral limit. The electric field is given as $E = -\partial\phi/\partial x = -(T_e/en_0)\partial n/\partial x$. According to Eq. (6), we then have $E(x/t) \sim h_0(x/t)$ as shown in Fig. 1.

The space-time varying local average ion velocity is given as the ratio of the ion flux and the ion density, which by use of Eqs. (6) and (8) gives

$$U_1(x,t) \equiv \frac{F_1(x,t)}{n_1(x,t)} = \frac{\int_{x/t}^{\infty} \gamma h_0(\gamma) d\gamma}{\int_{x/t}^{\infty} h_0(\gamma) d\gamma}, \tag{11}$$

independent of Δn. For illustration of U_1, see Fig. 2(b). For $x/t \to \infty$, we find that this velocity increases without limit, although the density of these fast particles becomes small since $n_1(x,t) = \Delta n \int_{x/t}^{\infty} h_0(\gamma) d\gamma \to 0$ here. We find it interesting to note that the asymptotic limit of $U_1(\zeta \to \infty)$ is the same for all T_e/T_i, even in the absence of collective interaction (i.e., $T_e = 0$). The few particles experiencing the large initial electric fields are accelerated to high velocities, i.e., velocities exceeding the ion thermal velocity u_{th}. The present result is thus consistent with other studies,[1] where it is argued that a small number of ions get accelerated to very high velocities in front of an expanding plasma pulse. The results in Fig. 2 include also the free streaming result: we note that the fastest particles (i.e., the largest U_1 found at large ξ) in the present model are freely streaming, corresponding to a ballistic motion. One limitation of the analysis is found in the assumption of Boltzmann distributed electrons: for large local ion velocities this assumption brakes down, but as said, this limitation affects only a small number of ions. For very large average ion velocities, the present simplified self-similar model breaks down, but we find the trend shown in Fig. 2(b) interesting.

The phase space variation of the ion velocity distribution is illustrated in Figs. 3 and 4 for the two temperature ratios $T_e/T_i = 3$ and $T_e/T_i = 6$ analyzed before. The analysis assumes as in Fig. 2 that the unperturbed ion velocity distribution $f_0(u)$ is a Maxwellian. If we integrate the distributions in Figs. 3 and 4 with respect to velocity u, we obtain the density variations shown in Fig. 2. The figures illustrate how particles are accelerated by the collective electric fields, giving a surplus for positive velocities and a corresponding deficit for negative velocity regions. The collective electric fields are stronger for larger temperature ratios: if we take $T_e/T_i = 1$, we see very little difference as compared to the case with $T_e = 0$, indicating that dispersion by free streaming ions dominates the space-time plasma evolution for $T_e/T_i \leq 1$.

We show results for the illustrative reference case where $f_0(u)$ is a Maxwellian with vanishing average velocity. Results for a drifting Maxwellian are easily obtained by a change in the origin of the x/t-axis and the velocity axis in Figs. 3 and 4.

Concerning normalization of these and following results we note that with a Maxwellian velocity distribution an ion thermal velocity enters as a natural unit for velocity normalization. In the present self-similar limit, there are no natural length or time scales, so we can normalize position and time with the ion Debye length λ_i and the ion plasma period $1/\omega_{pi}$, respectively, but we can choose the combination $\alpha\lambda_i$ and α/ω_{pi} as well, with arbitrary values of α. In the following, we choose $\alpha = 1$ also when normalizing collision frequencies. We thus have normalized relative positions $\xi \equiv (x - x_g)/\lambda_i$ and $\tau \equiv (t - t_0)/\omega_{pi}$ in terms of a reference position x_g and a reference time t_0, so that the ratio ξ/τ is normalized by C_s.

III. NUMERICAL SIMULATIONS

The numerical studies are carried out by a PIC simulation using a code described elsewhere.[20] We formulate the

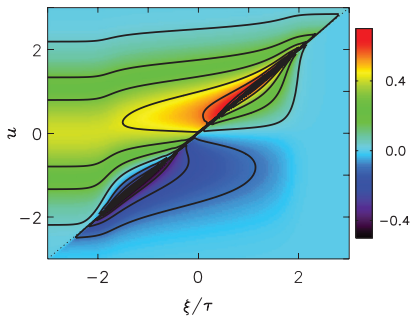

FIG. 3. Color coded ion velocity distribution for $T_e/T_i = 3$, obtained for the reference case with $f_0(u)$ being a Maxwellian ion velocity distribution, see also Figs. 1 and 2.

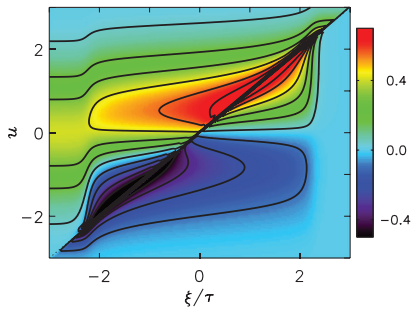

FIG. 4. Color coded ion velocity distribution for $T_e/T_i = 6$. See also Fig. 3.

problem and its boundary conditions so that it applies for the operation of a single ended Q-machine,[14,21] where electrons are emitted thermally, while ions are produced by surface ionization at a hot cathode. Under steady state conditions, the ion velocity distribution in the main plasma (outside the end-sheaths) is a truncated Maxwellian.[14] In the basic version of the Q-machine, the ions are produced by contact ionization[22] of hot alkali metals with suitable work functions.[23] The metal plate also supplies electrons by Richardson emission. We will in the following assume that a confining homogeneous axial magnetic field is sufficiently strong to justify a description in one spatial dimension.

Assuming standard operating conditions for a Q-machine in our simulations, we use electron rich conditions, where the hot plate at $x=0$ can supply electrons in abundance. The electrons are emitted with a velocity distribution $n_{0e}\sqrt{m/2\pi T_0}\exp(-\frac{1}{2}mu^2/T_0)$ for $u>0$, where T_0 is the hot plate temperature in energy units, and similarly for the ions we have $n_{0i}\sqrt{M/2\pi T_0}\exp(-\frac{1}{2}Mu^2/T_0)$ for $u\geq 0$. Our reference case corresponds to $n_{0e}/n_{0i}=1/3$. For such cases, the plasma assumes a negative potential in front of the cathode in order to reflect the surplus of electrons, while ions on the other hand are accelerated by the potential drop to give a net ion flow through the device. A step-like initial condition is obtained by absorbing a part of the ions passing through a grid at a reference position at $x=x_g$. At a time when a steady state condition is achieved, we have a step-like condition with an ion density $n_0+\Delta n$ for $x<x_g$ and n_0 for $x>x_g$, where Δn depends on the absorption rate. At a reference time t_0, the ion absorption is cancelled and the initial density discontinuity is allowed to evolve freely. This condition can be realized in a Q-machine by immersing a fine meshed grid at $x=x_g$. The ion absorption can be controlled by an externally applied potential.[5,18] The physical conditions summarized here are those being simulated by use of our PIC code.[20]

In Video 1, with corresponding still-figure or "snapshot" in Fig. 5, we show an illustrative case with 50% ion absorption at the reference positions $x_g=0$. We initialize the analysis by an empty plasma column. First, we see the filling-up of the plasma, and when a steady state condition has been obtained, we stop the ion absorption at $t=t_0$ and the entire ion-population is allowed to expand into the region $x>0$. The code is general, and does not make use of quasi-neutral assumptions, so we observe the Debye shielding with the electron density extending a distance of the order of λ_{De} into the region $x>x_g$ at times $t<t_0$. The electron-rich sheaths at the two ends of the plasma column are noticeable.

The self-similar nature of the space-time evolution is shown best by a video. In this case, we use the video as a diagnostic tool and not merely for illustration. After the reference time t_0 where the ion absorption is stopped, we continuously rescale the x-axis to show the figure as a function $(x-x_g)/(t-t_0)$, see Video 2. See also still-figure or snapshot in Fig. 6. The code allows also the electron time-scale to be resolved. We note that after a short transient time interval of the order of $1/\omega_{pe}$, the space-time evolution becomes nearly self-similar: this is evidenced by the velocity distribution as well as the potential becoming stationary when represented as functions of $(\xi/\tau)/C_s=(x-x_g)/(t-t_0)$. For small $\Delta n/n_0$, we find that the self-similar variation is nearly perfect for $t>1/\omega_{pe}$. For the nonlinear case in Video 2 (see also Fig. 6), we note at late times a "detachment" of the distribution function from the line $u=x/t$ for velocities $u\leq u_{th}$, the ion thermal velocity, resulting in a "void" in phase space. For large velocities, where the phase space

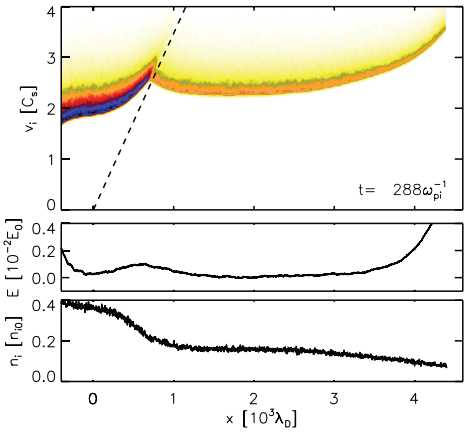

FIG. 5. We show here the space-time evolution of ion phase-space, the electric field, and the ion density for a case where $\Delta n/n_0=0.50$. The dashed line gives $u=x/t$ for reference. The code does not assume quasi-neutrality and Poisson's equation is retained for generality. We can consequently observe the Debye shielding of the charge surrounding the absorbing grid up to a distance of the order of λ_{De} (enhanced online) [URL: http://dx.doi.org/10.1063/1.4816953.1].

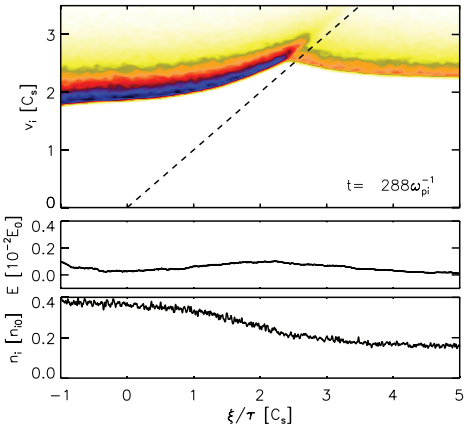

FIG. 6. We show here a restricted part of the space-time evolution in Video 1 (see Fig. 5), now in terms of the normalized self-similar variable ξ/τ. We have $\Delta n/n_0=0.5$. Only a part of the axis is shown, since the two electron rich sheaths at the ends of the plasma column are not accounted for in the present analysis (enhanced online) [URL: http://dx.doi.org/10.1063/1.4816953.2].

density is small, we find that the self-similarity remains to a good approximation. This nonlinear effect was anticipated by analytical studies.[9]

In Fig. 7, we show "snap-shots" or still-figures of ion phase-space, electric field, and ion density all obtained at $t - t_0 = 112\omega_{pi}^{-1}$. Note that for the conditions relevant, for instance, for Q-machines, there is no symmetry in the distribution of particles faster and slower than the average velocity, respectively. The symmetry found in, for instance, Fig. 2 for the forward and backward propagating density variations will be lost. The self-similarity of the solution is, however, independent of any symmetry conditions (see Sec. II) and will remain. We can give a simple illustration of the loss of symmetry by considering the freely streaming ions, which is included in Eq. (4) for $T_e = 0$. Taking $f_0(u) = (1/a)\exp(-\frac{1}{2}Mu^2/T_i)$ for $u > u_{min}$ and $f_0(u) = 0$ for $u < u_{min}$ for some minimum velocity u_{min} (as in our simulations and in most Q-machine experiments[14]), we have the normalization constant $a = \sqrt{\pi/2}\sqrt{T_i/M}\big(1 - \mathrm{erf}\,(u_{min}\sqrt{M/2T_i})\big)$, and $n(x,t) = \Delta n\sqrt{\pi/2}\sqrt{T_i/M}\big(1 - \mathrm{erf}\,(\sqrt{M/2T_i}\,x/t)\big)/a$ for $x/t \geq u_{min}$ and $n(x,t) = \Delta n$ for $x/t < u_{min}$.

A. Nonlinear effects

The analysis in Sec. II applies for small perturbations only. By the numerical simulations, we can study the deviations from these results as the amplitude Δn of the perturbation is increased. For illustration, we show in Fig. 7 results from four simulations with different values of Δn. For the smallest perturbation level $\Delta n = 0.1$, we improve the signal-to-noise ratio by taking the average of four runs with different initializations of the random number generators injecting the particles. The singular line $u = x/t$ remains in the velocity distribution also for nonlinear perturbations as anticipated by expression (3) derived from first principles with the given approximations. For moderate temperature ratios, $T_e/T_i \leq 6$, the results for $\Delta n/n_0 \leq 0.25$ are in good agreement with what we expect from a linearized analysis, as also found in related laboratory experiments.[5]

In Fig. 8, we illustrate the space-time evolution of a condition with a relatively large initial perturbation, here $\Delta n/n_0 = 0.5$. The figure illustrates the most conspicuous nonlinear effect found in the density evolution, namely ions reflected by the propagating density step. The velocity of these reflected particles is close to twice the step velocity,

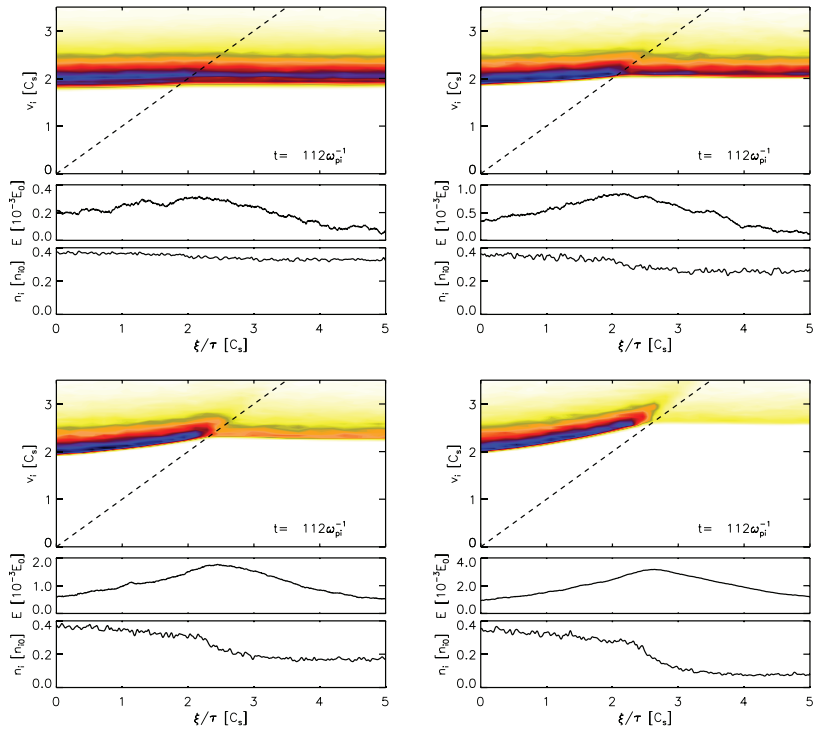

FIG. 7. Illustrations of results for the ion velocity distributions, variations of electric fields, and density for varying perturbation amplitudes, as functions of $\xi/\tau \equiv x/t/C_s$, here with $\Delta n/n_0 = 0.10$, 0.25 (top left and right) 0.5, and 0.75 (bottom left and right). A dashed line in the phase-space representation gives $u = x/t$, with the origin being at the reference grid position. The figures are all obtained at a time $112\,\omega_{pi}^{-1}$.

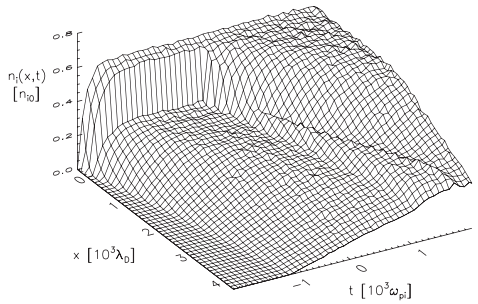

FIG. 8. Space-time evolution of the ion density in the numerical simulations of a collisionless plasma. The figure shows the initial filling-in of the system, with a step discontinuity with $\Delta n/n_0 = 0.5$, which is released at $t = 0$. Note the small amplitude precursor that propagates with approximately twice the speed of sound. The figure is obtained by average of 30 realizations with different initializations of the random number generators.

i.e., approximately $2C_s$. In order to improve the signal-to-noise ratio in Fig. 8, we averaged 30 runs with identical macroscopic conditions but different initializations of the random number generators. Otherwise, the reflected particles would be masked by the fluctuation due to discrete particle effects.

IV. THE EFFECTS OF NEUTRAL COLLISIONS

To account for collisional interactions, the ion Vlasov equation is often modified by a simple collision term as $-\nu\big(f(u,x,t) - n_0 f_0(u)\big)$, or its generalizations. In the present study, we distinguish elastic ion collisions with neutrals, and charge exchange collisions. Both cases are studied numerically. For the latter processes, we can obtain a closed analytical solution by introducing a physically realistic collision model in the ion Vlasov equation.

Analytical results using a general energy conserving Bhatnagar–Gross–Krook (BGK)-model in a kinetic description can be found in the literature,[24,25] but these results refer to discontinuities initiated by a moving piston. Here, we outline analytical results directly applicable for the present initial value problem. For some special cases, the results become remarkably simple.

A. Analytical models for charge-exchange collisions

Consider a model for charge exchange collisions based on a simple collisional term of the form $-\nu(f_1 - n_1 f_0(u))$, where again $n_1 \equiv \int f_1 du$ and $\int f_0(u) du = 1$. In linearized form, the collision term becomes $-\nu(f_1 - f_0(u) n_1)$ to be added to the right hand side of the linearized ion Vlasov equation. It turns out to be relatively easy to retain a velocity dependence of the collision frequency $\nu = \nu(u)$ within the following analysis. The integral transforms found in the following can, however, no longer be expressed in terms of known functions, and the practical value of the results will be limited. We, therefore, here take ν to be constant, and make the transformation $f_* \equiv f_1 \exp(\nu t)$, giving $n_* \equiv n_1 \exp(\nu t)$, to find

$$\frac{\partial}{\partial t} f_* + u \frac{\partial}{\partial x} f_* - \frac{T_e}{M} \frac{\partial n_*}{\partial x} \frac{\partial}{\partial u} f_0(u) - \nu f_0(u) n_* = 0. \quad (12)$$

A constant value for ν implies that the collisional cross sections vary as $\sigma \sim 1/u$ with varying velocity, and serves only as a solvable convenient model for charge exchange collisions. More generally, we have, however, that polarization forces ("Maxwellian molecules") give constant ν for a wide range of velocities[26] so the model as such is not unphysical.

After a temporal Laplace transform (with complex s) and spatial Fourier transform (with real k) of Eq. (12), we have

$$(s + iku) f_*(k,u,s) - n_*(k,s)\left(ik \frac{T_e}{M} f_0'(u) + \nu f_0(u)\right) = f_*(k,u,t=0) = i \frac{\Delta n}{k} g(u), \quad (13)$$

or

$$f_*(k,u,s) = i \frac{\Delta n}{k} \frac{g(u)}{s + iku} + n_*(k,s) \frac{ikC_s^2 f_0'(u) + \nu f_0(u)}{s + iku}, \quad (14)$$

giving

$$n_*(k,s) = \frac{i \frac{\Delta n}{k} \int \frac{g(u)}{s + iku} du}{1 - \int \frac{ikC_s^2 f_0'(u) + \nu f_0(u)}{s + iku} du}, \quad (15)$$

where $g(u)$ is the velocity distribution in the perturbation for $x < 0$. Integration limits are omitted for simplicity: they are $\int_{-\infty}^{\infty} du$ in all cases shown. The ensuing method of solution can be used for this general case, but a remarkable simplification results by taking $g(u) = f_0(u)$. In this case, the analysis contains only one nontrivial complex function, which can then be related to the plasma dispersion function for a Maxwellian choice of $f_0(u)$. The solution of the problem is then obtained by methods outlined in the literature.[27] We have

$$n_*(k,s) = \frac{\Delta n}{k^2} \frac{h_*(is/k)}{1 + i(\nu/k) h_*(is/k)} \equiv \frac{\Delta n}{k^2} N_*(k,s), \quad (16)$$

where we introduced the complex function

$$h_*(is/k) \equiv \frac{\int \frac{f_0(u)}{u - is/k} du}{1 - C_s^2 \int \frac{f_0'(u)}{u - is/k} du}.$$

For the ensuing inverse transforms, we note that for $k < 0$ the singularity at $is/k = u$ is *below* the u-axis for the velocity integration, while it is *above* for $k > 0$. To distinguish the two cases, we introduce the notation $n_*^{(1)}(k,s)$ for $k < 0$ and $n_*^{(2)}(k,s)$ for $k > 0$.

We have

$$n_*(x,s) = \frac{1}{2\pi} \int_{-\infty}^{0} \frac{\Delta n}{k^2} N_*^{(1)}(k,s) e^{ikx} dk + \frac{1}{2\pi} \int_{0}^{\infty} \frac{\Delta n}{k^2} N_*^{(2)}(k,s) e^{ikx} dk$$

and

$$n_*(x,t) = \frac{1}{i2\pi}\int_{s_0-i\infty}^{s_0+i\infty} n_*(x,s)e^{st}ds,$$

where $s_0 > 0$. The inverse Fourier transform is separated into two parts, $-\infty < k \le 0$ and $0 \le k < \infty$ as shown. We introduce the variable $\gamma \equiv is/k$ with γ real, giving $d\gamma = -is\,dk/k^2$. With this choice, we have h_* to be a function of a real variable, i.e., $h_* = h_*(\gamma)$, and we also have $N_*(k,s) \to N_*(\gamma,s) = h_*(\gamma)/(1+(\nu/s)\gamma h_*(\gamma))$. Deforming the integration contour as shown in Fig. 9, we find

$$n_*(x,s) = \frac{\Delta n}{2\pi}\int_0^\infty \frac{N_*^{(1)}(\gamma,s) - N_*^{(2)}(\gamma,s)}{is}e^{-sx/\gamma}d\gamma. \qquad (17)$$

The integrals along the circular contours in Fig. 9 vanish when $R \to \infty$. The integrations along the two closed contours shown (containing I and III, and II and IV, respectively) are vanishing. We note that we have a zero for the denominator of $n_*(\gamma,s)$ for $s = -\nu\gamma h_*(\gamma)$, recalling that, in general, $h_*(\gamma)$ is a complex function of real γ.

For linearly stable plasmas, the inverse Laplace transform of

$$\frac{h_*(\gamma)}{1+(\nu/s)\gamma h_*(\gamma)}\frac{e^{-sx/\gamma}}{is}$$

is determined to give the final result in the form

$$\begin{aligned} n_*(x,t) &= \frac{\Delta n}{2\pi} i\int_{x/t}^\infty [h_*^{(2)}(\gamma)\exp\big(t\nu(\gamma - x/t)h_*^{(2)}(\gamma)\big) \\ &\quad - h_*^{(1)}(\gamma)\exp\big(t\nu(\gamma - x/t)h_*^{(1)}(\gamma)\big)]\,d\gamma \\ &= \frac{\Delta n}{\pi}\int_{x/t}^\infty [\Im\{h_*^{(2)}(\gamma)\}\cos(\Im\{h_*^{(2)}(\gamma)\}t\nu(\gamma - x/t)) \\ &\quad - \Re\{h_*^{(2)}(\gamma)\}\sin(\Im\{h_*^{(2)}(\gamma)\}t\nu(\gamma - x/t))] \\ &\quad \times \exp\big(-\Re\{h_*^{(2)}(\gamma)\}t\nu(\gamma - x/t)\big)\,d\gamma, \end{aligned} \qquad (18)$$

where the two functions $h_*^{(2)}(\gamma)$ and $h_*^{(1)}(\gamma)$ are complex conjugates and $\Im\{h_*^{(2)}(\gamma)\}/\pi \equiv h_0(\gamma)$. By $\Re\{\}$, we understand the real part of the function in the brackets. Expression (18) is strongly simplified in the limit $\nu \to 0$, and we recover here the special case (6) where we use definition (5). The self-similar x/t-dependence is lost when $\nu \neq 0$, see Fig. 10. For short times, $t \ll 1/\nu$ we have solutions close to the previous

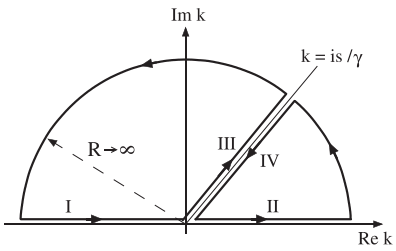

FIG. 9. Integration contours in the complex k-plane.

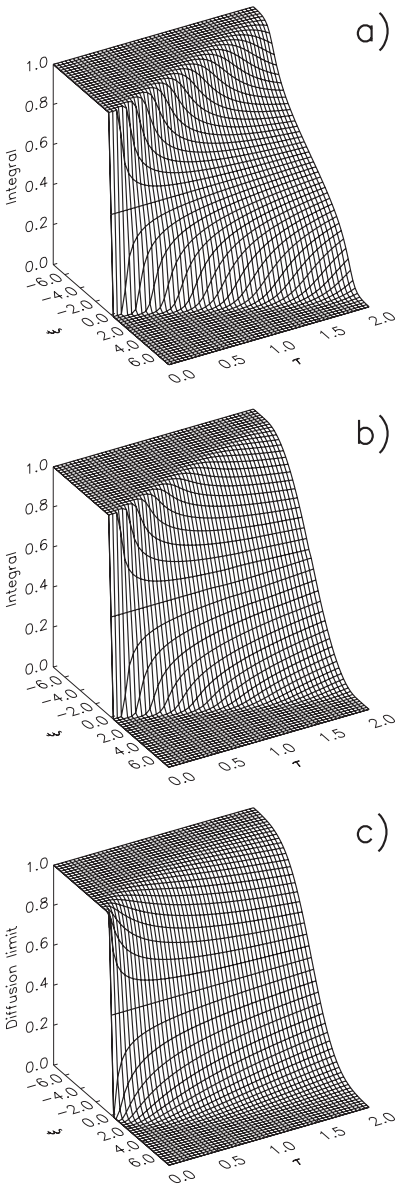

FIG. 10. The space-time evolution of the normalized plasma density $n/\Delta n$ for a step-like initial perturbation with $T_e/T_i = 3$, including collisional effects with $\nu/\omega_{pi} = 2$ is shown in (b). For reference, we show the collisionless case with $\nu = 0$ in (a) and the corresponding solution for the diffusion equation in (c), where the normalized diffusion coefficient is here $D \equiv (C_s/u_{ti})^2/(\nu/\omega_{pi})$. For large times, we find that the density variations shown in (b) and (c) are almost identical, while for short times the density variations in (a) and (b) are almost identical.

self-similar result, but for later times deviations develop, and the solution approaches the form characterizing diffusion equations.

The result (18) may at first sight appear complicated. In reality, it contains only elementary functions in addition to $h_0(\gamma)$ which, in turn, can here be expressed by the Z-function[19] for Maxwellian velocity distributions or sums of such. The integral in Eq. (18) is readily carried out numerically, the only complication being the oscillatory integrand.

For the velocity distribution function we find by Eq. (12), where now $n_*(x,t)$ is known

$$f_*(x,u,t)/\Delta n = g(u)\mathcal{H}(u-x/t) + C_s^2\frac{\partial f_0(u)}{\partial u}\int_0^t \frac{\partial n_*(x-u(t-t'),t')}{\partial x}dt' + \nu f_0(u)\int_0^t n_*(x-u(t-t'),t')\,dt', \tag{19}$$

where the first term (containing Heaviside's step function $\mathcal{H}$) corresponds to the free streaming contribution from the initial perturbation, here taken as $g(u) = f_0(u)$. The final results are obtained as $n_1 = n_* e^{-\nu t}$ and $f_1 = f_* e^{-\nu t}$. Since the self-similarity of the solution is lost for large times when $\nu \neq 0$, we no longer have any singularity at $x/t = u$: it is smoothed over by the collisions. The time-integrations in Eq. (19) are not easily carried out analytically due to the $\int_{x/t}^{\infty} d\gamma$-integral entering the expression for the density. For large times, the most significant contribution to $f_*(x,u,t)$ comes from the last term in Eq. (19).

Results based on Eq. (19) are shown as ion phase-space diagrams in Fig. 11 for 2 different times for a normalized spatial variable. For $t < 1/\nu$, the results are almost indistinguishable from that shown in Fig. 3 in agreement also with experimental results[5] where the space-time evolution of ion velocity distributions was measured. For late times, on the other hand, we find a collision-dominated evolution of the velocity distribution function. The case with high collision frequency is illustrated in Fig. 12, to be compared to Fig. 11. The two figures are obtained at the same time in units of ω_{pi}^{-1}, but the collision frequency is doubled in Fig. 12.

Result (19) together with (18) offers a theoretical result which, albeit somewhat complicated, allows for illustrating a continuous transition from a collisionless to a collision-dominated space-time evolution of the ion velocity distribution for the given step-like initial condition.

B. Strongly collisional regime

Using $n_1 = n_* e^{-\nu t}$ and $f_1 = f_* e^{-\nu t}$ and integrating Eq. (12) with respect to u, we obtain the continuity equation for n_1. Multiplying the expressions with u and integrating as before, we have the momentum equation. Assuming $T_e \gg T_i$ and large ν, this expression contains Fick's first law in the form $nU \approx -(C_s^2/\nu)\partial n/\partial x$, where U is the average ion velocity for the perturbation. Using this expression in the continuity equation, we obtain a diffusion equation for the plasma density with diffusion coefficient $D \equiv C_s^2/\nu$. When the collisional mean free path is the shortest length scale in the system (i.e., shorter than the length-scale for the density gradient), we can approximate the dynamics by a simple diffusion equation having the relevant solution in the form

$$n_1(x,t) = \frac{\Delta n}{2}\left(1 - \mathrm{erf}\left(\frac{x}{\sqrt{4Dt}}\right)\right), \tag{20}$$

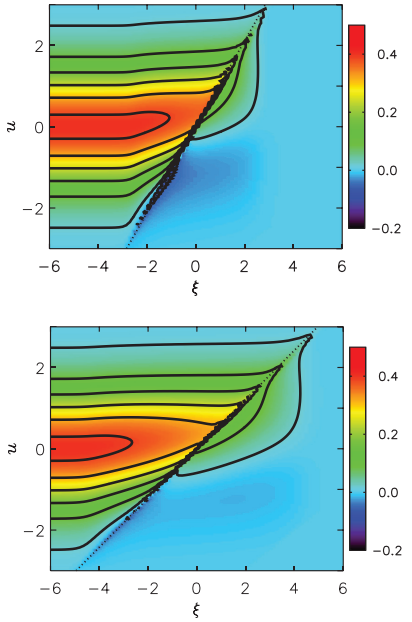

FIG. 11. Analytical results for the ion velocity distribution in normalized phase-space, as obtained from Eq. (19) with $\nu \neq 0$ and $T_e/T_i = 3$. We show the phase-space for two times, $t = 0.5/\nu$ and $0.85/\nu$. The dotted line shows $u = x/t$, for reference. Note that the evolution is no longer self-similar. The figures are to be compared to the collisionless case shown in Fig. 3 obtained with the same temperature ratio.

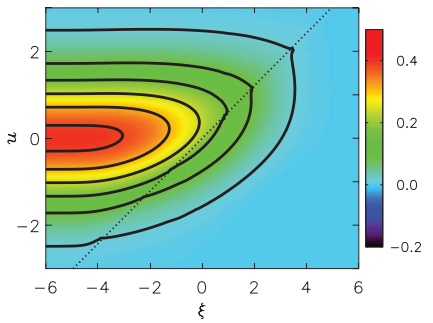

FIG. 12. Analytical results for the ion velocity distribution in normalized phase-space with doubled collision frequency as compared to Fig. 11. Other parameters are the same as in Fig. 11.

in terms of the error function, $\mathrm{erf}(x) \equiv (2/\sqrt{\pi})\int_0^x e^{-y^2}dy$. In this limit, we have a dynamic length scale $\sqrt{Dt}$ characterising the time evolution of the initial condition, and the self-similar variable x/t from the analysis in Sec. II is lost. In the diffusion limit, the ion velocity distribution remains close to $f_0(u)$, which for realistic conditions is a Maxwellian with constant temperature T_i. Result (20) is shown for reference in Fig. 10(c).

We note that Eq. (19) with $f_1 = f_* e^{-\nu t}$ offers a general relation between the plasma density and the ion velocity distribution function as described by the ion Vlasov equation with collisional effects included. We analyzed also the ion velocity distribution for late times obtained by using the analytical form (20) in Eq. (19). The result obtained for $f_1(x,u,t)$ by this procedure is almost identical to the late time expression obtained analytically with collisional effects retained in Eq. (12). We confirmed also here that for large times the most significant contribution to $f_1(x,u,t)$ comes from the last term in Eq. (19).

V. NUMERICAL RESULTS FOR PLASMAS WITH CHARGE EXCHANGE COLLISIONS

We analyze the effects of ion neutral collisions numerically, and consider two cases: elastic and charge exchange collisions between the plasma ions and a neutral background. Also other types of collisions can be important, but we expect these two to be representative for collisional interactions in general.

Charge exchange collisions often have the largest cross section, this type of interaction being resonant,[28] and will be particularly important for many realistic cases.

In Fig. 13, we show the space-time evolution of the plasma density for two cases, where $\ell_c = 1000$ and $500\,\lambda_{De}$, respectively. The absorbing grid is placed at $x = 0$. The filling in of the plasma column (including the effect of the charge exchange collisions) begins at $t = -2$ as in Fig. 8, and the step-like density perturbation is released at $t = 0$. We find that the signal has an enhanced noise level due to the collisions, although 30 realizations are averaged as in Fig. 8. Note that the step-like front found in Fig. 8 is no longer present, as expected from the analytical results. Rather we find (for both mean free paths shown) a monotonically decreasing plasma density as in Fig. 10(c). Due to the charge exchange collisions, the average ion flow velocity is reduced along the axis. Flux conservation of the ion flow from the origin (the hot plate in a Q-machine) along the x-axis will give rise to an enhancement of the plasma density as compared to the case without collisions.

In Fig. 14, we show numerical results (to be compared with the phase-space results for the collisionless simulations in Fig. 7 and density variations in Fig. 8) with charge exchange effects included. We show results for two collisional mean free paths, in both cases with $\Delta n/n_0 = 1/2$. The most conspicuous effect of the collisions is that the step-like front seen in, for instance, Fig. 10 disappears, and is replaced by a variation closer to the one given by Eq. (20). The neutral component is taken to be at rest, and we see the formation of a slow ion component composed by particles that has

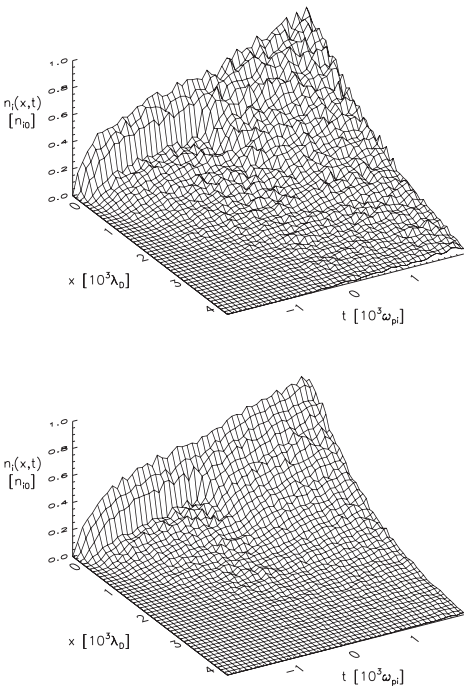

FIG. 13. Space-time variation of the plasma density with charge exchange collisions included, with mean free path $\ell_c = 1000$ (top) and $500\,\lambda_{De}$ (bottom). Both cases have $\Delta n/n_0 = 0.5$. As compared to Fig. 8, the signal has an enhanced noise level due to the collisions, although 30 realizations are averaged also here as in Fig. 8. The absorbing grid is placed at $x = 0$. The filling in of the plasma column (including the effect of the charge exchange collisions) begins at $t = -2$ as in Fig. 8, while the step-function is released at $t = 0$.

undergone a charge exchange collision. This is seen best for the smallest mean free path, $\ell_c = 500\,\lambda_{De}$. The average velocity of these particles is positive, since they are also accelerated by the collective electric fields. In Video 3 (see also corresponding "snap-shot" in Fig. 15), we show the space-time evolutions for density, electric field, and ion phase-space. Note how the self-similarity disappears as time increases.

One basic conclusion from the collisional simulations is that a laboratory experiment for realizing a step-like initial condition is best performed for a collisionless case: we find that the charge exchange collisions induce an inhomogeneous plasma density along the axis of the device and the ideal unperturbed state is not obtained. We find, however, a qualitative agreement with the analytical results.

Our code also allows for inclusion of elastic ion collisions. Also, these processes have been studied numerically, and some differences can be noted, but need not be presented here, since our analytical model applies best for the charge exchange collisions.

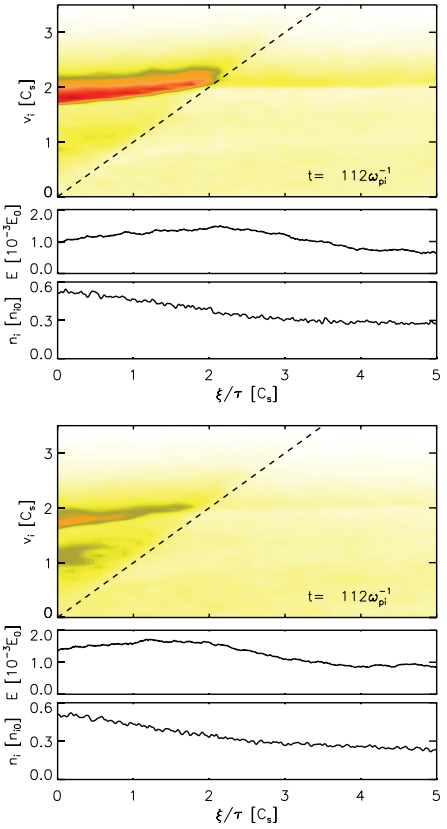

FIG. 14. Numerical simulations with charge exchange collisions, with mean-free collision paths $\ell_c = 1000$ and $500\,\lambda_{De}$.

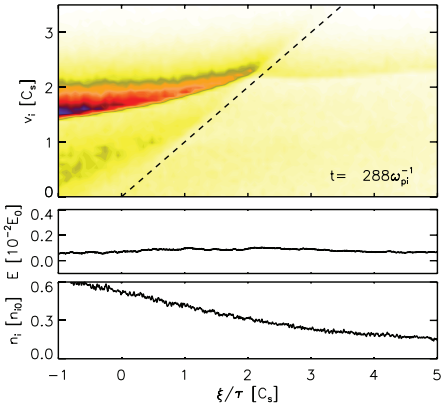

FIG. 15. Numerical simulations where charge exchange collisions are included. We show the space-time evolution of the ion density (bottom frame) electric field (middle frame) and the phase-space for the ion velocity distribution (top frame) for a case where $\Delta n/n_0 = 0.50$, with mean-free collision paths $\ell_c = 1000$ (enhanced online) [URL: http://dx.doi.org/10.1063/1.4816953.3].

VI. DISCUSSIONS

The results in the present work are formally obtained without assumptions on the ratio T_i/T_e. In principle, they apply to Q-machine conditions as well as those met in, for instance, Double Plasma (DP) devices. With the assumption of quasi-neutrality, we do not have the Debye length in the basic equations and we do not recover the dispersive ripples associated with the time evolution of an initial discontinuity.[29] For Q-machine experiments, we have typically an effective temperature ratio in the range $1 < T_e/T_i \leq 3$, so the dispersive ripples are heavily ion Landau damped in those cases. The restriction by the assumed quasi-neutrality is of minor importance in these cases and we find that the results in the present paper are in excellent agreement with the experimental results obtained in a Q-machine[5] also concerning experimentally obtained ion velocity distributions. For larger temperature ratios, it might be an advantage to retain Poisson's equation. Also, this analysis has been carried out in one spatial dimension.[27,30] In this case, the self-similarity of the solution is lost: self-similarity is a property of problems without any characteristic length and time scales. In the quasi-neutral limit of kinetic ion-acoustic waves, we have neither the ion plasma frequency nor the Debye lengths as characteristic quantities; all we have is a characteristic velocity, C_s.

Our numerical results confirmed the analytically obtained self-similar space-time evolution. The theoretical results were illustrated for the special reference case where the unperturbed ion velocity distribution is a full Maxwellian. This case is facilitated by allowing the plasma dispersion function[19] to be introduced. The actual unperturbed ion velocity distribution is a truncated Maxwellian. The symmetry of the forward propagating density pulse and the backward propagating rarefaction wave found in the reference case is lost in our simulations, but the forward propagating density enhancement, and the potential and electric field derived from it, follow the analytical results well.

The time evolution of an initially step-like perturbation in plasmas with large electron-to-ion temperature ratios was investigated by a very elegant method in a DP-device.[31] In this case, the initial perturbation was introduced by a collimated "flash" of light from a vacuum spark between Molybdenum electrodes. The intense light ionizes a fraction of the neutral background gas in the device, and thus produces a "slab" of additional plasma to the pre-existing uniform background plasma produced by the standard DP-operation. Because of the large temperature ratio, the dispersive ripples were clearly observable in this experiment. By a quasi-neutral approximation, such ripples are in effect smoothed out in the analytical results presented in our analysis.

We extended our analysis by introducing ion collisions. Analytical results were obtained by a linearized model with charge exchange collisions. We can follow the transition from the short time collisionless limit to the long time

collisional case, with some basic results shown in Fig. 10. We find it interesting that with a Maxwellian plasma the collisional term contributes with an expression given via the plasma dispersion function, even in the case where collective interactions are turned off by setting $T_e = 0$. Formally, it is a simple matter to retain a velocity dependence of the collision frequency by having a $\nu = \nu(u)$ factor entering the integrands, but then the Hilbert transforms can no longer be easily expressed in terms of the plasma dispersion function, and the practical value of the results is limited. The analytical result (18) contains the collisionless self-similar linearized kinetic result by setting $\nu = 0$, while it for large times, $\nu t \gg 1$, contains the results for a diffusion equation that also has an exact solution (20). These three results are summarized in Fig. 10.

The linearized analysis was carried out for a step-like initial condition. By differentiating this result with respect to the spatial variable x, we can obtain the results for the space-time evolution of an initial $\delta(x)$-perturbation. From this result, arbitrary spatially distributed initial perturbations can be constructed. In this sense, our linear analytical results have general applicability for collisionless as well as collisional plasmas for cases where charge exchange is dominant.

When comparing our results to numerical or laboratory experimental observations, we note that the presentation based on figures such as Figs. 2–4 or Fig. 10 is easy when shown as a function of position for fixed times. For most laboratory studies, it is easier to visualize a temporal variation for fixed position,[5] and in such cases the figures can be redrawn with advantage.

The present analytical results are exact for a linearized model equation, derived from the Vlasov equation including a collision term. The results are thus *not* obtained by use of some first or least damped pole approximation for the entire plasma dispersion relation. Since we used a linearized analysis, the results are not directly applicable, for instance, for plasma expanding into vacuum,[1] but we believe the results to have value as qualitative indications also for this case. This latter problem has received attention for experimental conditions with imposed initial conditions[6] but it can also be relevant for plasma flowing into the wake forming behind macroscopic solid objects immersed in plasmas at large relative flow velocities.[11,12,32,33]

ACKNOWLEDGMENTS

This work was supported in part by a grant from the Norwegian National Science Foundation. We thank Dr. Wojciech Miloch for his interest and for many valuable discussions on numerical problems.

[1]J. E. Crow, P. L. Auer, and J. E. Allen, "Expansion of a plasma into a vacuum," J. Plasma Phys. **14**, 65–76 (1975).
[2]Yu. V. Medvedev, "Ion front in an expanding collisionless plasma," Plasma Phys. Controlled Fusion **53**, 125007 (2011).
[3]Y. Huang, Y. Bi, X. Duan, X. Lan, N. Wang, X. Tang, and Y. He, "Self-similar neutral-plasma isothermal expansion into a vacuum," Appl. Phys. Lett. **92**, 031501 (2008).
[4]R. W. Gould, "Excitation of ion–acoustic waves," Phys. Rev. **136**, A991–A997 (1964).
[5]P. Michelsen and H. L. Pécseli, "Propagation of density perturbations in a collisionless Q-machine plasma," Phys. Fluids **16**, 221–225 (1973).
[6]V. Vanek and T. C. Marshall, "Ion-acoustic collisionless shocks in a Q-machine," Plasma Phys. **14**, 925–934 (1972).
[7]H. K. Andersen, N. D'Angelo, P. Michelsen, and P. Nielsen, "Investigation of Landau-damping effects on shock formation," Phys. Rev. Lett. **19**, 149–151 (1967).
[8]A. L. Gurevich, L. I. Pariĭskaya, and L. P. Pitaevskiĭ, "Self similar motion of rarefied plasma," J. Exp. Theor. Fiz. (U.S.S.R.) **49**, 647–654 (1965) [see also Sov. Phys. JETP 22, 449–454 (1966)].
[9]A. L. Gurevich, L. I. Pariĭskaya, and L. P. Pitaevskiĭ, "Self similar motion of a low-density plasma. II," Zh. Eksp. Teor. Fiz. **54**, 891–904 (1968) [see also Sov. Phys. JETP 27, 476–482 (1968)].
[10]J. Denavit, "Collisionless plasma expansion into a vacuum," Phys. Fluids **22**, 1384 (1979).
[11]T. Nakagawa, "Ion entry into the wake behind a nonmagnetized obstacle in the solar wind: Two-dimensional particle-in-cell simulations," J. Geophys. Res., [Space Phys.] **118**, 1849–1860, doi: 10.1002/jgra.50129 (2013).
[12]N. Singh and R. W. Schunk, "Numerical calculations relevant to the initial expansion of the polar wind," J. Geophys. Res. **87**, 9154–9170, doi:10.1029/JA087iA11p09154 (1982).
[13]D. Grésillon and P. L. Galison, "Instantaneous electron energy distribution function in ion waves," Phys. Fluids **16**, 2180–2183 (1973).
[14]R. W. Motley, *Q Machines* (Academic Press, New York, 1975).
[15]S. Børve, H. L. Pécseli, J. Trulsen, and S. Longo, "Kinetic instabilities associated with injection of a plasma beam into a neutral background," Phys. Scr. **T122**, 125–128 (2006).
[16]B. D. Fried and A. Y. Wong, "Stability limits for longitudinal waves in ion beam-plasma interaction," Phys. Fluids **9**, 1084–1089 (1966).
[17]H. L. Pécseli, *Waves and Oscillations in Plasmas* (Taylor & Francis, London, 2012).
[18]S. A. Andersen, G. B. Christoffersen, V. O. Jensen, P. Michelsen, and P. Nielsen, "Measurements of wave-particle interaction in a single ended Q-machine," Phys. Fluids **14**, 990–998 (1971).
[19]B. D. Fried and S. D. Conte, *The Plasma Dispersion Function* (Academic Press, New York, 1961).
[20]V. L. Rekaa, H. L. Pécseli, and J. K. Trulsen, "Numerical studies of a plasma diode with external forcing," Phys. Plasmas **19**, 082115 (2012).
[21]T. Klinger, F. Greiner, A. Rohde, and A. Piel, "Nonlinear dynamical behavior of thermionic low-pressure discharges. 2. Experimental," Phys. Plasmas **2**, 1822–1836 (1995).
[22]I. Langmuir and K. H. Kingdon, "Thermionic effects caused by vapors of alkali metals," Proc. R. Phys. Soc., Ser. A **107**, 61–79 (1925).
[23]H. B. Michaelson, "The work function of the elements and its periodicity," J. Appl. Phys. **48**, 4729–4733 (1977).
[24]R. J. Mason, "Weak shock generation according to the energy-conserving Bhatnagar-Gross-Krook kinetic equation," Phys. Fluids **13**, 1467–1472 (1970).
[25]R. J. Mason, "Electric field penetration into a plasma with a fractionally accommodating boundary," J. Math. Phys. **9**, 868–874 (1968).
[26]B. A. Trubnikov, "Particle interactions in fully ionized plasmas," in *Reviews of Plasma Physics*, edited by M. A. Leontovich (Consultants Bureau, New York, 1965), Vol. 1, pp. 105–204.
[27]R. J. Mason, "Structure of evolving ion-acoustic fronts in collisionless plasmas," Phys. Fluids **13**, 1042–1048 (1970).
[28]S. A. Andersen, V. O. Jensen, and P. Michelsen, "Charge-exchange cross-sections measured at low energies in Q machines," Rev. Sci. Instrum. **43**, 945–947 (1972).
[29]G. B. Whitham, *Linear and Nonlinear Waves* (John Wiley & Sons, New York, 1974).
[30]R. J. Mason, "Computer simulation of ion-acoustic shocks. The diaphragm problem," Phys. Fluids **14**, 1943–1958 (1971).
[31]D. B. Cohn and K. R. MacKenzie, "Electrostatic ion-acoustic shocks produced by density steps," Phys. Rev. Lett. **28**, 656–658 (1972).
[32]W. J. Miloch, H. L. Pécseli, and J. Trulsen, "Numerical studies of ion focusing behind macroscopic obstacles in a supersonic plasma flow," Phys. Rev. E **77**, 056408 (2008).
[33]S. Kimura and T. Nakagawa, "Electromagnetic full particle simulation of the electric field structure around the moon and the lunar wake," Earth, Planets Space **60**, 591–599 (2008).

Paper III

Ion pre-acceleration in fully self-consistent PIC simulations of supercritical perpendicular reforming shocks in multiple ion species plasmas

V. L. Rekaa, S. C. Chapman and R. O. Dendy
Astrophysical Journal, (submitted, 2014)

III

Ion pre-acceleration in fully self-consistent PIC simulations of supercritical perpendicular reforming shocks in multiple ion species plasmas

V. L. Rekaa[1]
[1] *Department of Physics, University of Oslo, Box 1048 Blindern, N-0316 Oslo, Norway*
v.l.rekaa@fys.uio.no
and

S. C. Chapman[2,3,4]
[2] *CFSA, Department of Physics, University of Warwick, Coventry CV4 7AL, U.K.*
[3] *MPI-PKS, Nöthnitzer Str. 38, D-01187 Dresden, Germany*
[4] *Dept. of Math. and Stat., Univ. of Tromsø, Box 6050 Langnes, N-9037 Tromsø, Norway*
and

R. O. Dendy[5,2]
[5] *CCFE, Culham Science Centre, Oxfordshire OX14 3DB, U.K.*

ABSTRACT

Supernova remnant and Heliopause termination shock plasmas may contain significant populations of minority heavy ions, with relative number densities n_α/n_i up to 50%. Preliminary kinetic simulations of collisionless shocks in these environments (Chapman et al. 2005) showed that the reformation cycle and acceleration mechanisms at quasi-perpendicular shocks can depend on the value of n_α/n_i. Shock reformation unfolds on ion spatio-temporal scales, requiring fully kinetic simulations of particle dynamics, together with the self-consistent electric and magnetic fields. This paper presents the first set of particle-in-cell simulations for two ion species, protons (n_p) and α-particles (n_α), with differing mass and charge-to-mass ratios, that spans the entire range of n_α/n_i from 0% to 100%. The interplay between the differing gyro length and time scales of the ion species is crucial to the time evolving phenomenology of the shocks, the downstream turbulence and the particle acceleration at different n_α/n_i. We show how the overall energisation changes with n_α/n_i, and relate this to the processes individual ions undergo in the shock region and in the downstream turbulence, and to the power spectra of magnetic field fluctuations. The cross over between shocks dominated by the respective ion species happens when $n_\alpha/n_i = 25\%$, and minority ion energisation is strongest in this regime. Energisation of the majority ion species scales with injection energy. The power spectrum of the downstream turbulence includes peaks at sequential ion cyclotron harmonics, suggestive of ion ring-beam collective instability.

Subject headings: collisionless shocks, cosmic rays, supernovae remnants, heliospheric termination shock

1. Introduction

Identification of the mechanisms by which particles are accelerated to cosmic ray energies in supernova remnants (SNR) and at the Heliopause termination shock (HTS) is an outstanding problem in astrophysics. While diffusive shock acceleration (Fermi 1949; Bell 1978; Blandford & Ostriker 1978) offers a potentially efficient process for acceleration of particles that are already mildly relativistic, the "injection" problem remains: what physical processes pre-accelerate ambient background ions and electrons from low energies to mildly relativistic energies, at which stage diffusive shock acceleration can take over? Resolving this question requires careful analysis of plasma astrophysical kinetic processes (Kirk & Dendy 2001) in astrophysical shock environments through theory and direct numerical simulation. These efforts (e.g. Dieckmann et al. (2006); McClements et al. (2001)) complement indirect and direct observations of particles in SNRs and at the HTS (Koyama et al. 1995; Enomoto et al. 2002), which show energy spectra suggesting that perpendicular shocks are sites at which pre-acceleration mechanisms operate.

Recent Particle-in-Cell (PIC) simulations of SNR and HTS shocks (Lembege & Savoini 1992; Schmitz et al. 2002a,b; Scholer et al. 2003; Shimada & Hoshino 2000; Lee et al. 2004, 2005a,b) show that the inclusion of full electron kinetics yields non-stationary solutions: self-reforming shocks, where the reformation occurs on the gyro scales of the incoming ions. The process is controlled by accumulation of reflected ions, where the shock ramp width is on the electron length scale. Reforming solutions of perpendicular shocks were obtained in hybrid simulations by Hellinger et al. (2002), given a suitable tuning of the electron viscosity component.

Detailed studies of particle trajectories have been performed for a range of shock geometries and parameters to investigate the mechanisms that pre-accelerate background ions to mildly relativistic energies. These studies either directly process the trajectories of ions self-consistently evolved in kinetic simulations (e.g. Lee et al. (2005a)), or use these simulations to provide the spatio-temporal fields in which the trajectories of test-particles are traced (e.g. Zank et al. (1996); Burrows et al. (2010); Yang et al. (2011b)). A major focus has been on Shock Drift Acceleration (SDA) and Shock Surfing Acceleration (SSA) mechanisms which respectively involve: acceleration as ions drift along the shock front, and (possibly multiple) reflection at the ramp and gyration in the foot region. In reforming shocks, the timing has been found to be crucial in determining the energisation of each ion, given that the structure of the ramp varies with the reformation process (Lee et al. 2005a).

SNR plasmas contain significant populations of minority heavy ions (Henry 1986; Ellison et al. 1997, 2001), with relative number densities up to 50% and multiple ion species with ion masses of order ten proton masses. Here, we perform the first fully kinetic self-consistent simulations which systematically investigate the physical consequences of multispecies ions on the physics of ion pre-acceleration at reforming supercritical shocks. For simpliciy we restrict this first study to two ion species with moderate mass ratio, that is, protons and α-particles. With this choice of this moderate mass ratio it is computationally feasable to span the full range of alpha particle/proton concentration ratios from 0 to 100%. This will identify any thresholds in mass concentration ratio at which ion pre-acceleration mechanisms change. Quasi-perpendicular shocks with multiple-ion species plasmas have only been treated self-consistently up to $n_\alpha/n_i = 25\%$ (Chapman et al. 2005). Non-self-consistent studies (Yang et al. 2011a) have allowed parametric studies of ion injection processes. Both these studies show that the reforming shock can accelerate the minority ion population. The preliminary self-consistent simulation (Chapman et al. 2005) showed that even moderate concentrations of heavy ions can modify the shock reformation spatio-temporal scales.

We perform the first systematic study of perpendicular magnetosonic shocks in plasmas, spanning the full range of relative α-particle densities n_α/n_i from 0% to 100%, where all particle species and fields are modelled self-consistently. The structure of the article is as follows: In section 2, we describe the numerical methods used in this study, and discuss shock geometry and plasma conditions. In section 3, we introduce our results, in which we: 1) demonstrate how the phase space dynamics of the ions change as we increase α-

particle density n_α/n_i; 2) investigate overall ion energisation with energy spectra for several n_α/n_i; 3) interpret these with phase space trajectories of individual ions; and finally 4) relate ion energisation to power spectral densities of downstream magnetic fields. In section 4, we summarize our results and present our conclusions. In these simulations, we can identify candidate acceleration mechanisms that occur upon shock injection as well as stochastic diffusion downstream, and we investigate how these depend on the relative ion density n_α/n_i. We do not attempt, nor is it feasible within our framework, to evolve the diffusion process to obtain final (saturated) energy spectra.

2. Simulation details

We use a 1D3V (where scalar and all three components of vector quantities are functions of one spatial coordinate and time) relativistic electromagnetic Particle-in-Cell (PIC) code EPOCH. This follows the structure outlined by Lapenta (2012) and has been used to study plasma kinetics across a broad range of applications. including the energisation of minority α-particle populations in magnetically confined fusion plasmas (Cook et al. 2010, 2011a,b, 2013). Here we simulate supercritical, collisionless, perpendicular magnetosonic shocks.

Our simulation setup resembles that of Chapman et al. (2005). Particles are injected through the upstream boundary, where we assume shifted Maxwellian distribution functions satisfying zero charge density and zero current in the upstream region. The upstream magnetic field is set to $\mathbf{B} = B_1\hat{\mathbf{z}}$, and the electric field $\mathbf{E} = E_1\hat{\mathbf{y}}$ is calculated self-consistently, where $\hat{\mathbf{y}}$ and $\hat{\mathbf{z}}$ are unit vectors perpendicular to the plasma inflow. We use the piston-method to generate the shock at the lower boundary, and shock following algorithms to obtain sufficiently long run times (Schmitz et al. 2002b).

To capture both multi-ion species and electron dynamics, we use reduced mass ratios $m_p/m_e = 20$ and $m_\alpha/m_e = 80$ ($m_\alpha/m_p = 4$) and charge ratios $q_p/q_e = -1$ and $q_\alpha/q_p = 2$, corresponding to a plasma consisting of electrons, protons and α-particles (fully ionized helium). The ratio of plasma frequency ω_{pe} to gyro frequency Ω_e of electrons is $\omega_{pe}/\Omega_e = 20$. In terms of ion dynamics and the overall shock reformation process, numerical simulations in one and two spatial dimensions (retaining all three velocity and field vector components) (Lembege & Savoini 1992; Shinohara et al. 2011) and with reduced mass ratio of protons to electrons (Scholer et al. 2003; Shinohara et al. 2011), are found to produce similar results to simulations in three spatial dimensions and (but not simultaneously) with realistic mass ratios.

The upstream magnetic field is set to $B_1 = 10^{-7}$T and temperature T_1 corresponding to plasma $\beta = 0.15$ for all species, the values of which are chosen to be those used by Schmitz et al. (2002a,b); Lee et al. (2004, 2005a,b); Chapman et al. (2005) to allow comparison of results, while being consistent with estimates of SNR conditions by e.g. Lucek & Bell (2000). We have electron number density $n_e \approx 4 \times 10^8\mathrm{m}^{-3}$ and ion number densities satisfying charge neutrality upstream, $n_e = n_i + 2n_\alpha$, for a given heavy ion density ratio n_α/n_i. We impose an upstream inflow velocity $V_0 = 2 \times 10^7\mathrm{m\ s}^{-1}$ (for an electron-proton plasma) of Mach $M = 8$, with respect to the magnetosonic speed $\sqrt{T_1/m_p + B_1^2/2\mu_0\rho}$. In the shock rest frame, the far upstream (1) and downstream (2) values of shock-normal velocity components are $u_1 = 1.5V_1$, $u_2 = 0.5V_1$, and the magnetic field $B_2/B_1 = 3$. If we scale these factors to realistic mass ratios m_p/m_e, as in Lee et al. (2004), we obtain $M \approx 100$, $\mathcal{E}_{p1} = 6$MeV and $T_1 = 100$eV.

We simulate a domain of size $L = 20\lambda_{p1}$, where $\lambda_{p1} = m_pV_1/eB_1$ is the upstream gyro radius of protons. Our spatial resolution Δx equals the plasma Debye length $\lambda_D = \epsilon_0 T/\sum_s n_s q_s^2$, and the time step Δt satisfies the Courant-Friedrichs-Levy condition for electromagnetic waves: $c\Delta t < \Delta x$ so that $\Delta t \approx 3 \times 10^{-6}\tau_{p1}$, where $\tau_{p1} = 2\pi\Omega_{p1}^{-1} = 2\pi m_p/eB_1$ is the upstream gyro period of protons. The ratio $L/\Delta x$ gives $\sim 70\,000$ cells on our spatial grid, with typically 50 computational particles per species per cell. Our shock following algorithm ensures that the inflow boundary is always at least $5\lambda_{p1}$ upstream of the shock front, which allows ample space for reflected ions in front of the shock and fluctuations in the downstream plasma. All results presented here are in the rest frame of the downstream plasma.

We perform a series of simulations of shocks with the same Mach number for different ratios

of ion densities n_α/n_i. Since all other macroscopic quantities are related to each other through the Mach number, we will fix the upstream magnetic field B_1 and allow all other quantities to vary. Specifically, the injection speed V_1, upstream proton kinetic energy $\mathcal{E}_{p1} = m_p V_1^2/2$, upstream gyro radius $\lambda_{p1} = m_p V_1/eB_1$ and corresponding wave number $k_{p1} = 2\pi/\lambda_{p1}$, vary from one simulation to the next. To allow consistent comparison, where the Mach number is the same for all ion densities, we use normalisation constants V_1, $\mathcal{E}_{p1}$, λ_{p1} and k_{p1} for each relative ion density n_α/n_i. These relate to each other as shown in Table 1, where values for V_1, $\mathcal{E}_{p1}$ and k_{p1} are given relative to reference values V_0, $\mathcal{E}_0$ and k_0 for a pure electron-proton plasma, $n_\alpha/n_i = 0\%$. Normalization constants for frequency $\Omega_{p1} = eB_1/m_p$ and time $\tau_{p1} = 2\pi/\Omega_{p1}$ does not depend on V_1 and do not vary with n_α/n_i.

Table 1:
Normalization constants

n_α/n_i	V_1 $[V_0]$	$\mathcal{E}_{p1}$ $[\mathcal{E}_0]$	k_{p1} $[k_0]$
0%	1.00	1.00	1.00
5%	0.96	0.92	1.04
10%	0.93	0.86	1.08
25%	0.86	0.74	1.16
50%	0.80	0.64	1.25
75%	0.76	0.58	1.31
95%	0.74	0.55	1.34
100%	0.74	0.55	1.35

3. Simulation results

3.1. Bulk particle dynamics and heating

We first present an overview of how the shock and ion dynamics vary with n_α/n_i. Figure 1 shows the magnetic field as function of position and time in the vicinity of the shock front for both a proton dominated plasma, $n_\alpha/n_i = 5\%$, and an α-particle dominated plasma, $n_\alpha/n_i = 95\%$. These plots are in the downstream plasma rest frame and the shock is propagating towards increasing x values. We see that the spatio-temporal scales of the reforming foot and ramp region are governed by the gyro period of the dominant ion species in both cases. We next look in detail at the phase space of ions at the times indicated by the horizontal lines in Fig. 1.

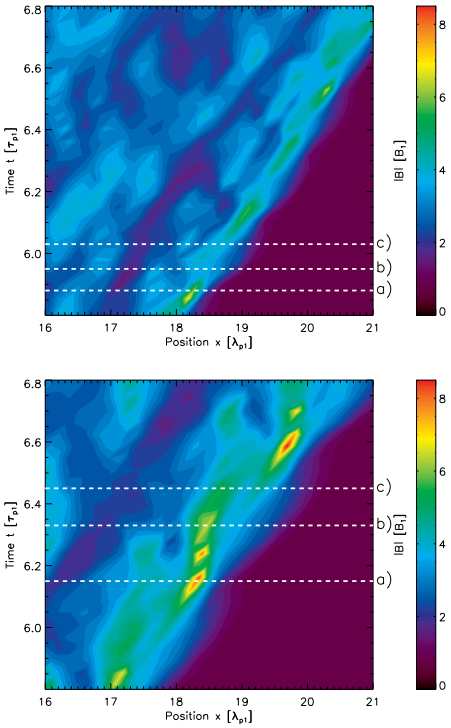

Fig. 1.—: Magnetic field $|B(x,t)|$ (normalized to upstream magnetic field B_1) for $n_\alpha/n_i = 5\%$ (top panel) and $n_\alpha/n_i = 95\%$ (bottom panel) in the rest frame of the downstream plasma, plotted as a function of position x on the horizontal axis (normalized to upstream proton gyro radius λ_{p1}) and time t on the vertical axis (normalized to upstream proton gyro period τ_{p1}). Field strength is indicated by the colour bar to the right. The white horizontal dashed lines indicate the times of the snapshots shown in Figs. 2 and 3.

Figure 2 shows snapshots at three phases of the shock reformation cycle, at times indicated in the top panel of Fig. 1 for $n_\alpha/n_i = 5\%$ when the shock foot extent is (a) minimum, (b) growing and (c)

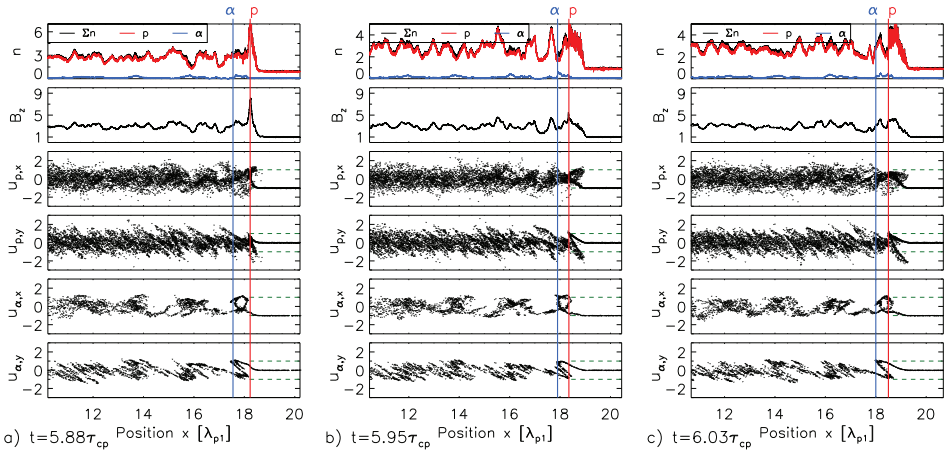

Fig. 2.—: Snapshots in the rest frame of the downstream plasma for $n_\alpha/n_i = 5\%$ at three consecutive times (normalized to upstream proton gyro period τ_{p1}) when the foot region extent is: (a) $t = t_0 = 5.88\tau_{p1}$ minimum; (b) $t = t_0 + 0.07\tau_{p1}$ growing; and (c) $t = t_0 + 0.15\tau_{p1}$ maximum. Panels from top to bottom show quantities plotted against position x (normalized to upstream proton gyro radius λ_{p1}): (1) total ion, proton and α-particle number densities ($\sum n = n_p + n_\alpha$, n_p; and n_α) (normalized to upstream electron density n_{e1}), (2) perpendicular magnetic field component B_z (normalized to upstream magnetic field B_1), and velocities (normalized to upstream injection velocity V_1 calculated for the respective n_α/n_i, see section 2) (3) proton velocity parallel to the inflow $u_{p,x}$ and (4) perpendicular to the inflow and magnetic field $u_{p,y}$; (5) α-particle $u_{\alpha,x}$ and (6) $u_{\alpha,y}$. Vertical lines indicate the reflection points near the shock front of protons (colored red online) and α-particles (blue online). Green dashed horizontal lines in velocity panels indicate $u = \pm V_1$.

maximum. Here we present snapshots of the u_x versus x and u_y versus x phase space of both ion species, as well as the magnetic field $B_z(x)$ and ion densities n_p, n_α and $\sum n = n_p + n_\alpha$. The first reflection points of protons and α-particles at the shock are indicated by vertical red and blue lines, respectively. We see that proton dynamics follow the phase of the reformation cycle during which they are incident on the shock front. Protons are quickly thermalized downstream, indicating stochastic acceleration, that is, multiple scattering of ions on the fluctuating electromagnetic fields in the downstream region, leading to diffusive acceleration. α-particles, however, are directly transmitted through the shock front as a mono-energetic beam, following coherent (ordered) trajectories in phase space.

Figure 3 is for a $n_\alpha/n_i = 95\%$ simulation, in the same format as Fig. 2, for times indicated in the bottom panel of Fig. 1. Here the roles of the protons and α-particles, and the overall dynamicsi, are reversed compared to Fig. 2: protons now follow coherent trajectories in phase space because all are reflected at the front regardless of the shock reformation phase, whereas α-particles now follow the shock reformation cycle. One key difference between the two simulations is that, when the α-particles are the minority species, they do not gain net energy as they travel through the shock. Energy associated with the bulk motion upstream V_1 translates to gyration downstream with $u_\perp = V_1$. On the other hand, when the protons are in the minority, they gyrate in the front region and gain $u_\perp \to V_1$. Subsequently they energise downstream and gain $u_\perp \to 2V_1$.

Figure 4 shows a sequence of simulations which span the range $n_\alpha/n_i = 5\% - 95\%$. These are in the same format as Figs. 2 and 3, for times when

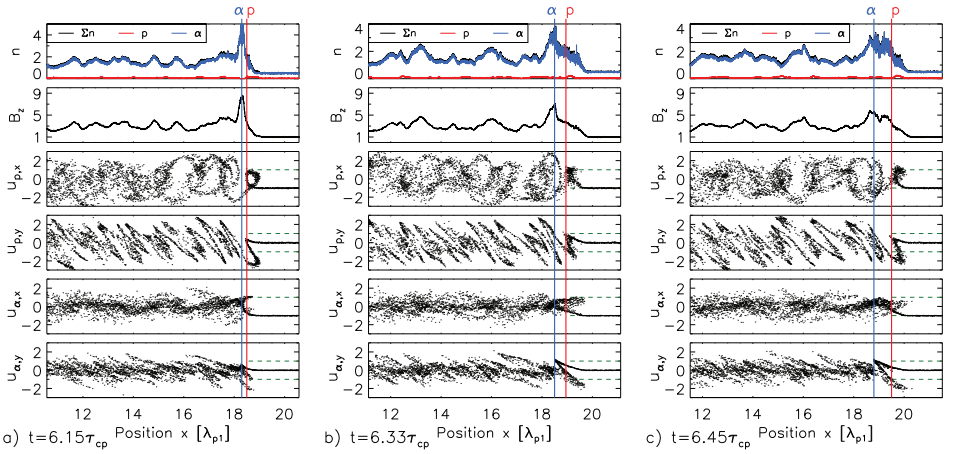

Fig. 3.—: Snapshots in the rest frame of the downstream plasma at three consecutive times for $n_\alpha/n_i = 95\%$ when the extent of the shock foot is: (a) $t = t_0 = 6.15\tau_{p1}$ minimum; (b) $t = t_0 + 0.18\tau_{p1}$ growing; and (c) $t = t_0 + 0.30\tau_{p1}$ maximum. Format and normalization as in Figure 2 for $n_\alpha/n_i = 95\%$ (for normalization, see section 2).

the foot extent is minimum. There is a transition, at $n_\alpha/n_i \sim 25\% - 50\%$, from proton to α-particles as the species which follows the reformation dynamics of the shock. The majority species appears to be more rapidly thermalized downstream compared to the minority species, for which the motion remains more coherent. The downstream dynamics result in strong density fluctuations which closely correspond to the fluctuations in the downstream magnetic field. In the foot-ramp region of the shock, we find for intermediate α-particle densities, double ramps due to density peaks of the respective ion species. The reflection point of protons is consistently found upstream of that of α-particles. Both species always gain at most velocity V_1 in the foot region, consistent with reflection at a stationary shock (Lee et al. 2004), which has been found to be the case in reforming shocks as different from non-reforming quasi-perpendicular shocks. Subsequently, in all these cases, the protons when in minority are accelerated to $\sim 2V_1$ in the ramp, while the α-particles when in minority do not gain energy in the foot-ramp region.

3.2. Energetic particle dynamics

The key result found in Figs. 2-4 is that the majority species controls the shock reformation while minority species perform coherent dynamics, including acceleration, in the foot-ramp region. We now investigate phase space trajectories and energisation of individual ions as they move through the shock and propagate downstream.

We can calculate the work done on each particle using its full spatio-temporal history $x(t)$ and velocity $\mathbf{u}(t)$, and the fields experienced along the trajectory, $\mathbf{E}(x(t), t)$ and $\mathbf{B}(x(t), t)$. The particle energy gain between t_0 and t_1 is

$$\Delta\mathcal{E}(t_0, t_1) \equiv q \int_{t_0}^{t_1} \mathbf{u}(t) \cdot \mathbf{E}(t) dt \ . \qquad (1)$$

We investigate energisation associated with x- and y-motion by plotting the components of the change in energy,

$$\Delta\mathcal{E}_x = q \int u_x E_x dt, \ \ \Delta\mathcal{E}_y = q \int u_y E_y dt, \qquad (2)$$

where x-motion is parallel to the inflow and y-motion is parallel to the induced upstream electric field $\mathbf{E} = E_1 \hat{\mathbf{y}}$.

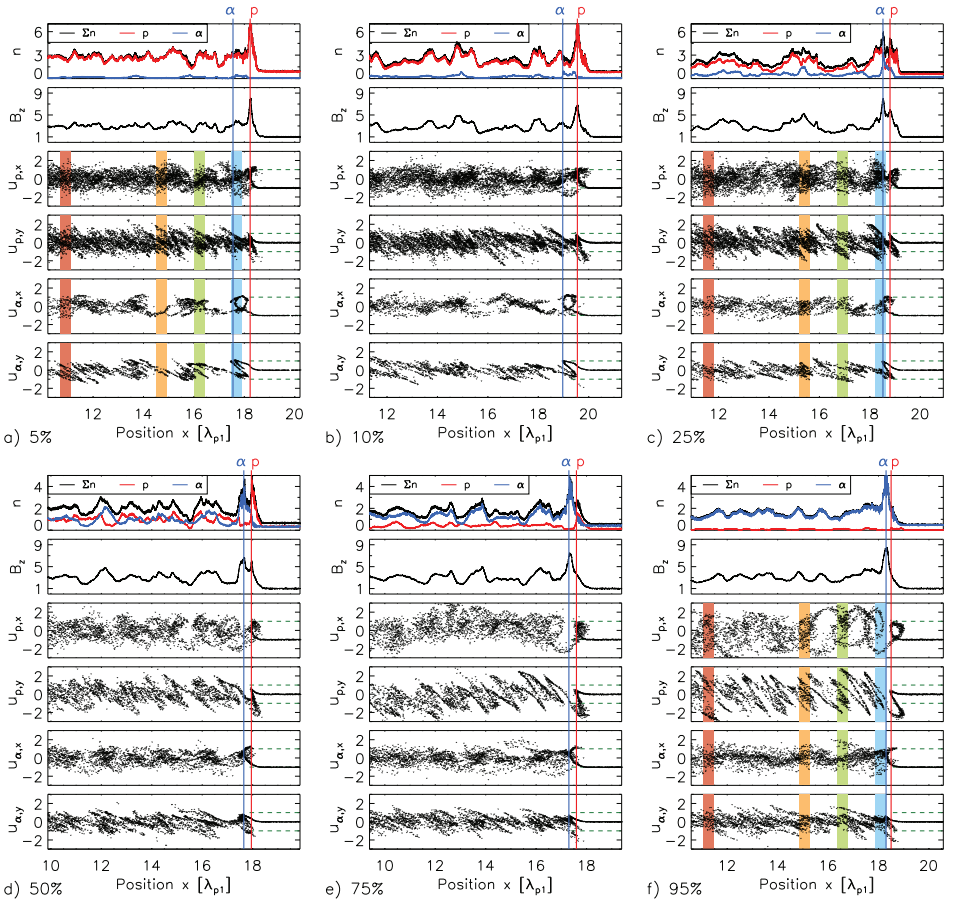

Fig. 4.—: Snapshots in the rest frame of the downstream plasma at times when the foot region extent is minimum (corresponding to left hand panels of Figs. 2 and 3) for a) $n_\alpha/n_i = 5\%$, b) 10%, c) 25%, d) 50%, e) 75% and f) 95%, in the same format as Figs. 2 and 3, with normalization constants calculated for the respective n_α/n_i (see section 2). Shaded regions in the phase space diagrams indicate centroid positions relative to the shock ramp $\Delta x = -7.5\lambda_{p1}$ (colored red online), $-3.5\lambda_{p1}$ (orange online), $-1.7\lambda_{p1}$ (green online) and $-0.5\lambda_{p1}$ (blue online) of particle ensembles for which energy spectra presented in section 3.2 are calculated.

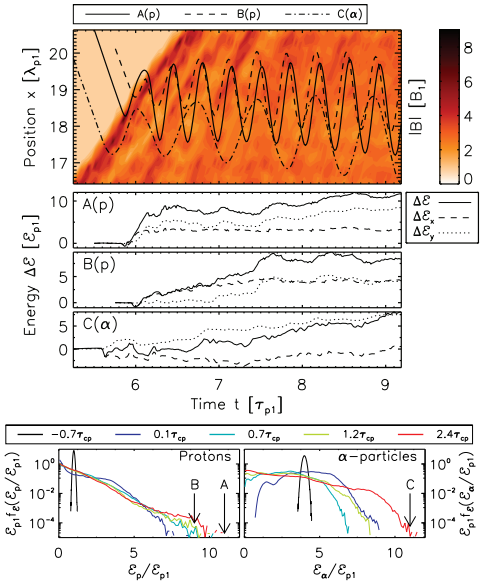

Fig. 5.—: Individual trajectories of protons (A,B) and an α-particle (C) in the rest frame of the downstream plasma for a simulation with $n_\alpha/n_i = 5\%$, plotted as functions of time (normalized to upstream gyro period τ_{p1} of protons). Upper panel: particle position $x(t)$ (normalized to upstream gyro radius of protons λ_{p1}) plotted over the spatio-temporal evolution of magnetic field $|B(x,t)|$ (normalized to upstream magnetic field B_1). Lower three panels plot change in kinetic energies: in total $\Delta\mathcal{E}(t)$; of x-motion $\Delta\mathcal{E}_x(t)$; and y-motion $\Delta\mathcal{E}_y(t)$, normalized to proton injection energy $\mathcal{E}_{p1}$ calculated for the given n_α/n_i (see section 2). Bottom panels: energy spectra of protons (left) and α-particles (right). Energy spectra are calculated at five consecutive times $\Delta\tau$, one before crossing the shock front, $\Delta\tau = -0.7\tau_{p1}$ and four after $\Delta\tau = 0.1\tau_{p1}$, $0.7\tau_{p1}$, $1.2\tau_{p1}$ and $2.4\tau_{p1}$, with corresponding particle ensemble centroid locations as indicated by shaded regions in Fig. 4. The final energies of trajectories A, B and C are indicated by arrows.

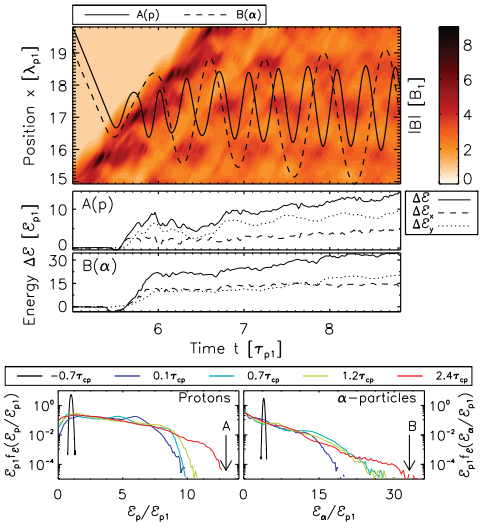

Fig. 6.—: Individual trajectories of a proton (A) and α-particle (B) in the rest frame of the downstream plasma for $n_\alpha/n_i = 95\%$, together with ion energy spectra, in the same format as Fig. 5.

Trajectories of individual ions, drawn from the most energetic component of the population downstream, are shown for $n_\alpha/n_i = 5\%$ in the upper panels of Figure 5, for $n_\alpha/n_i = 95\%$ in Figure 6 and for an intermediate case $n_\alpha/n_i = 25\%$ in Figure 7. Here we compare spatio-temporal trajectories $x(t)$ plotted over magnetic field strength with energisation $\Delta\mathcal{E}(t)$, $\Delta\mathcal{E}_x(t)$ and $\Delta\mathcal{E}_y(t)$.

In the lower panels of Figs. 5-7, we plot total energy spectra $f_\mathcal{E}(\mathcal{E}_p)$ and $f_\mathcal{E}(\mathcal{E}_\alpha)$, normalized to unity $\int \mathcal{E}_{p1} f_\mathcal{E}(\mathcal{E}_p/\mathcal{E}_{p1}) d\mathcal{E}_p = \int \mathcal{E}_{p1} f_\mathcal{E}(\mathcal{E}_\alpha/\mathcal{E}_{p1}) d\mathcal{E}_\alpha = 1$, where $\mathcal{E}_i = \mathcal{E}_{i1} + \Delta\mathcal{E}(t)$. Spectra are calculated from ensembles of 700 000 particles, initially selected while upstream, then traced as they travel through the shock front. Spectra are calculated once upstream, at time $\Delta\tau = -0.7\tau_{p1}$ relative to when the ensembles arrive at the shock front (where $\tau_{p1} = 2\pi\Omega_{p1}^{-1}$ is the upstream proton gyro period), and at four times downstream $\Delta\tau = 0.1\tau_{p1}$, $0.7\tau_{p1}$, $1.2\tau_{p1}$ and $2.4\tau_{p1}$. At the latter time, the ions have typically completed 10 (protons) and 5 (α-particles) gyro orbits. En-

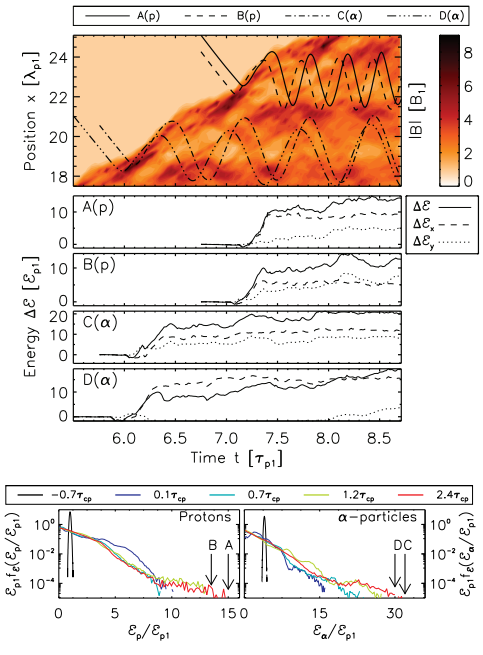

Fig. 7.—: Individual trajectories of protons (A,B) and α-particle (C,D) in the rest frame of the downstream plasma for $n_\alpha/n_i = 25\%$, together with ion energy spectra, in the same format as Figs. 5 and 6.

ergy is normalized to proton injection energy $\mathcal{E}_{p1}$ of the respective ion densities n_α/n_i which, from the arguments given in section 2, decreases with increasing n_α/n_i. The centroid positions of the particle ensembles at times $\Delta\tau$ are indicated by shaded regions in Fig. 4.

Figure 5 shows two proton trajectories (A,B) and one α-particle trajectory (C) for a proton dominated plasma, $n_\alpha/n_i = 5\%$. The final particle energies are indicated by arrows in the energy spectra in the same figure. The most prominent difference between protons A and B is that proton A is accelerated at the shock front, whereas B is directly transmitted without significant acceleration. Stochastic acceleration downstream remains equally efficient for the two, regardless of their shock front energisation. The α-particle (C), on the other hand, gains no energy at the front and is only accelerated further downstream. Energisation due to y-motion may have saturated for B, but not for A and C. The energy spectra support this interpretation, because the high energy tails continue to evolve at late times in these simulations. The knee (or cut-off) in the α-particle energy spectra further indicates that thermalization is not complete.

Figure 6 shows one proton (A) and one α-particle (B) trajectory in an α-particle dominated plasma, $n_\alpha/n_i = 95\%$, where the final energies of A and B are indicated in the energy spectra. The time history of α-particle B, which is now the majority species, closely resembles that of proton A in Fig. 5 where protons are the majority species. In both cases, energy spectra $f_\mathcal{E}(\mathcal{E})$ of the majority species have formed energetic tails while the minority species have not.

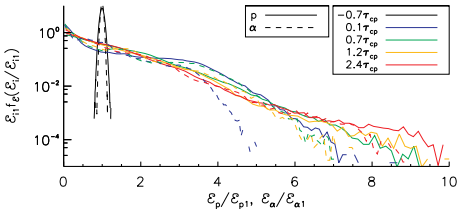

Fig. 8.—: Energy spectra of the majority ion species in the rest frame of the downstream plasma, i.e. protons for $n_\alpha/n_i = 5\%$ and α-particles for $n_\alpha/n_i = 95\%$. Energy spectra are calculated at five consecutive times $\Delta\tau$, one before crossing the shock front, $\Delta\tau = -0.7\tau_{p1}$ and four after $\Delta\tau = 0.1\tau_{p1}$, $0.7\tau_{p1}$, $1.2\tau_{p1}$ and $2.4\tau_{p1}$, with corresponding particle ensemble centroid locations as indicated by shaded regions in Fig. 4. Spectra of both species are normalized to each respective upstream injection kinetic energy, i.e. $\mathcal{E}_p/\mathcal{E}_{p1}$ and $\mathcal{E}_\alpha/\mathcal{E}_{\alpha 1}$, satisfying $\int \mathcal{E}_1 f_\mathcal{E}(\mathcal{E}/\mathcal{E}_i)d\mathcal{E}_i = 1$ for both ion species.

Figure 7 shows an intermediate case where $n_\alpha/n_i = 25\%$. We find a much larger variation in phase space trajectories in this simulation compared to those for $n_\alpha/n_i = 5\%$ and 95%, suggesting that a broader variety of energisation paths

are available to both species. We also see more extended high energy tails for both ion species in the energy spectra, suggesting that these intermediate cases are potentially more efficient at particle acceleration.

In Figure 8 we test the idea that the majority species energisation follows a simple parametric scaling. The energy spectra of two simulations, here $n_\alpha/n_i = 5\%$ and 95%, are normalized to the upstream injection kinetic energy of the majority species, i.e. $\mathcal{E}_{\alpha 1} f_\mathcal{E}(\mathcal{E}_\alpha/\mathcal{E}_{\alpha 1})$ and $\mathcal{E}_{p1} f_\mathcal{E}(\mathcal{E}_p/\mathcal{E}_{p1})$. These spectra then collapse over each other except at the highest energies where statistics are poor. The energy spectra of the majority species, when scaled to each respective ion species injection energy, $\mathcal{E}_{p1}$ and $\mathcal{E}_{\alpha 1}$, overlap well, indicating that shock energisation scales with the injection energy of the ion species. This is not the case for the minority ion species, where protons are found to gain more energy relative to their injection energy than α-particles. In this case, at least for the acceleration in the foot-ramp, the scaling is identifiable from Figs. 2-4, where minority protons gain $2V_1$.

3.3. Wave energy

In Figures 2-4, the beginning of thermalization can be seen in the downstream region when ions can scatter off magnetic field fluctuations. Whilst these simulations cannot run for a sufficient length of time to follow the full thermalization and stochastic heating of the ions, we can identify the nature of the downstream fluctuations that contribute to this stochastic process.

We analyse power spectra $P(k, \omega)$ of the magnetic field $|B(x, t)|$ as functions of wave number k and frequencies ω in the rest frame of the downstream plasma, during a finite time $[t_0, t_0 + T_D]$ and within a finite region $[x_0, x_0 + L_D]$, using Welch's method (Welch 1967). We integrate the power spectra $P(k, \omega)$ for $\omega > 0$ over k to obtain the frequency spectrum $P(\omega)$. The discrete nature of the input signal $B(x, t)$, reflecting the finite diagnostic output time interval $\Delta t_D = \tau_{p1}/20$ and total sampling time $T_D = 1.6\tau_{p1}$, places upper and lower limits on the frequency domain, $\omega \in [2\pi/T_D, 2\pi/\Delta t_D] = [0.6\Omega_{p1}, 20\Omega_{p1}]$.

Figure 9 shows frequency spectra $P(\omega)$ for simulations with ion densities ranging from $n_\alpha/n_i =$ 0% to 100%. The spectra have multiple peaks at harmonics of the downstream ion gyro frequencies of the protons and α-particles. The gyro frequencies in the magnetic field far downstream (2) $\langle B_2 \rangle = 3B_1$, are indicated in the plot for protons Ω_{p2} and α-particles $\Omega_{\alpha 2}$. As the fraction of α-particles is increased, the total power increases. As Ω_{p2} harmonics are coincident with $\Omega_{\alpha 2}$, these are always present. We can see that there is a systematic increase in power at the harmonics of $\Omega_{\alpha 2}$ as the relative ion density n_α/n_i is increased.

There appear to be points of contact between the simulation results encapsulated in Fig. 9 and the physics of edge-localised minority energetic ions in magnetic confinement fusion plasmas. Specifically, suprathermal emission at multiple sequential ion cyclotron harmonics is observed in fusion plasmas containing a minority ring-beam population of energetic ions. Perhaps most notably, this ion cyclotron emission (ICE) was driven by minority energetic (3.5 MeV) minority-particles born in fusion reactions between thermal (10keV to 20keV) deuterons and tritons confined in the JET and TFTR experiments. Here energetic minority ring-beam populations arose naturally at the outer mid-plane edge (Cottrell et al. 1993; Dendy et al. 1995) because of drift orbit effects. ICE was detected using heating antennas, designed to launch the fast Alfven wave, as receivers on JET. Analytical theory, contemporary with the JET and TFTR observations, suggested that the excitation mechanism for ICE is the magnetoacoustic cyclotron instability (MCI), driven by a set of centrally born fusion products, lying just inside the trapped-passing boundary in velocity space, whose drift orbits make large radial excursions to the outer mid-plane edge (Dendy et al. 1994; Cauffman et al. 1995). Recent first-principles fully nonlinear PIC (Cook et al. 2013) and hybrid (Carbajal et al. 2014) simulations of the MCI confirm that the dominant excited modes are fast Alfven. That is, fluctuations in density and magnetic field strength are approximately in phase, as is also the case in the downstream turbulence giving rise to Fig. 9. Phenomenology similar to ICE in fusion experiments has been observed in terrestrial magnetospheric plasmas (McClements & Dendy 1993; Dendy & McClements 1993). The possibility of related effects at SNR shocks was noted by McClements et al. (1996). For example, first princi-

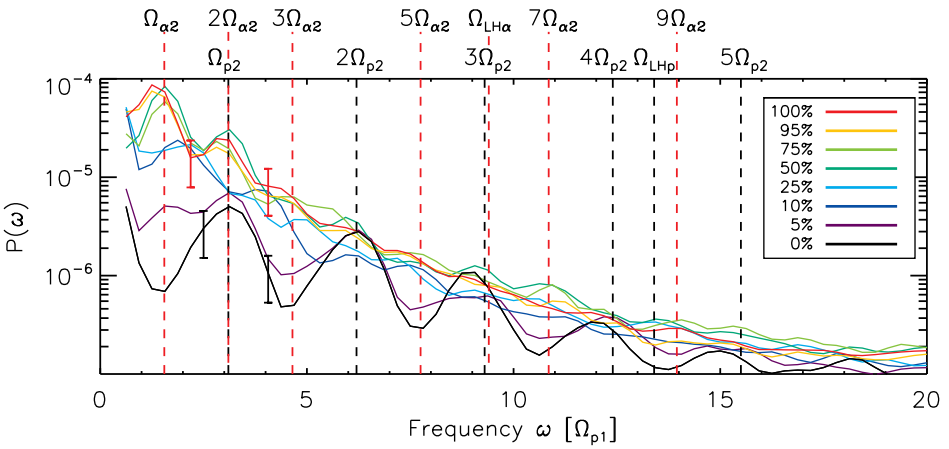

Fig. 9.—: Power spectra of temporal fluctuations in the magnetic field $|B(x,t)|$, downstream of the shock front, in the plasma rest frame. Spectra are shown for n_α/n_i = 0%, 5%, 10%, 25%, 50%, 75%, 95% and 100%. B is normalized to the ratio of injection kinetic energy of protons $\mathcal{E}_{p1}$ to the upstream gyro frequency Ω_{p1}. We plot $P(\omega)$ versus frequency ω/Ω_{p1} for $\omega > 0$. Gyro frequencies of protons Ω_{p2} and α-particles $\Omega_{\alpha 2}$ (and higher harmonics of these) in a downstream magnetic field $B_2 = 3B_1$ are indicated by vertical dashed lines (red for α-particles, black for protons). The expected values of lower hybrid frequencies of an electron-proton plasma Ω_{LHp} and electron-α-particle plasma $\Omega_{LH\alpha}$, are also indicated.

ples direct numerical simulations show that waves excited in this range of frequency and wavelength are capable of pre-accelerating electrons in SNR environments (Dieckmann et al. 2000; Schmitz et al. 2002b,a).

There is a spectral peak a $\Omega_{LH\alpha}$ for the lowest α-particle concentrations $n_\alpha/n_i \leq 5\%$. While waves in this frequency range are known to be excited by ring-beam (and other) minority energetic alpha-particle populations (Cook et al. 2010, 2011a,b), this peak is more likely to be the third cyclotron harmonic of the protons, which is nearly degenerate with the lower hybrid frequency of α-particles. No noticeable peak is found at the lower hybrid frequency of protons in any proton dominated simulation, and no peak at the lower hybrid frequency of α-particles is found in simulations where α-particles dominate

Finally, in Figure 10, we plot a representative power spectrum $P(k,\omega)$ against wave number and frequency for a simulation where $n_\alpha/n_i = 50\%$. The full k,ω-spectrum is broadband but has most energy within the phase speeds $\omega/k = (0.6-1)V_1$. The value $0.6V_1$ corresponds to the magnetosonic wave speed in the downstream regions, assuming average downstream (2) macroscopic values for the magnetic field $\langle B_2\rangle \approx 3B_1$, mass density $\langle \rho_2\rangle \approx 2.5\rho_1$ and temperature $\langle T_2\rangle \approx 50T_1$ with respect to upstream quantities (1). However, we can also interpret these fluctuations as a non-propagating mode that arises as a consequence of the density fluctuations downstream, which in turn directly relate to the downstream ion dynamics. We have seen that magnetic field B_2 and ion density n_2 fluctuations strongly correlate downstream. The spatial scale is then that of the downstream gyration $u_\perp/\Omega$, and the temporal scale is that of the downstream gyro period $1/\Omega$. Thus $\omega/k \equiv u_\perp$, and the value $u_\perp$ ranges from V_1 to $\sim 0.5V_1$ for directly transmitted and accelerated ions.

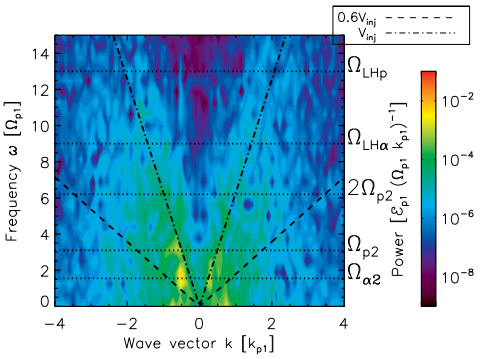

Fig. 10.—: Power spectrum of spatio-temporal fluctuations in the magnetic field $|B(x,t)|$ of the downstream region for $n_\alpha/n_i = 50\%$, in the rest frame of the plasma. B is normalized to the ratio of injection kinetic energy of protons $\mathcal{E}_{p1}$ to the upstream gyro frequency Ω_{p1}, and wave number to the upstream gyro radius $k_{p1} = 2\pi\lambda_{p1}^{-1}$. We plot $P(k,\omega)$ versus frequency ω/Ω_{p1} and wave number k/k_{p1} for $\omega > 0$. Gyro frequencies in the downstream magnetic field $\langle B_2\rangle = 3B_1$, $\Omega_{\alpha 2}$ and Ω_{p2} (and their higher harmonics), as well as lower hybrid oscillation frequencies $\Omega_{LH\alpha}$, and Ω_{LHp} are indicated by horizontal (dotted) lines. Lines for $\omega/k = \pm u$ are plotted for $u = 0.6V_1$ (dash) and $u = V_1$ (dash-dot).

4. Conclusions

In this paper, we present the first fully self-consistent PIC simulations that systematically span the range of relative heavy ion densities $n_\alpha/n_i = 0\%-100\%$. We find that spatio-temporal scales of the foot-ramp region and downstream fluctuations depend on n_α/n_i. In a shock dominated by one ion species, the shock dynamics are controlled by the majority species and the energy gain of the majority species scales with the inflow energy for a given Mach number. Thermalization of the majority species downstream is rapid although not complete. Energisation occurs both by reflection of subsets of ions at the foot-ramp and by stochastic motion in turbulence generated downstream. The interaction with the foot-ramp may be characterized as a single coherent gyrationr; we do not see multiple interactions with the foot-ramp region as are suggested to occur in for example SSA. The minority species dynamics remain coherent through the shock. On encountering the foot-ramp, the upstream bulk speed V_1 is translated to gyrational motion with perpendicular velocity $u_\perp \to V_1$. The α-particles do not gain net energy, whereas the protons ultimately gain up to $u_\perp \to 2V_1$. For intermediate cases of n_α/n_i, there are several paths to energisation, and net energisation of both species is enhanced compared to the cases where one species is the majority. Fluctuations downstream embody dominant density structures that are in turn generated by the ion dynamics. These can act to thermalize the ions. Our results are consistent with the findings of Chapman et al. (2005) and Yang et al. (2011a).

Astrophysical plasmas typically contain several minority species with intermediate relative number densities. Our simulations show that ion energisation, for intermediate heavy ion densities, gives rise to extended high energy tails in the energy spectra. This suggests that real astrophysical shocks have favourable conditions for accelerating ions to supra-thermal energies.

Oblique wave modes, and waves propagating perpendicular to the direction of inflow, are not captured by the current simulations, due to the exact perpendicular geometry of the shock. We are thus unable to model wave-particle interactions due to such wave modes and energy transport perpendicular to the inflow. However, our simulations are sufficient to capture the essential shock reformation process.

Acknowledgements

The work was supported in part by the Research Council of Norway, the UK Engineering and Physics Sciences Research Council under grant EP/G003955 and by the European Communities under the contract of association between Euratom and CCFE. The views and opinions expressed herein do not necessarily represent those of the European Communities. The EPOCH code used in this research was developed under UK Engineering and Physics Sciences Research Council grants EP/G054940/1, EP/G055165/1 and EP/G056803/1. We thank Profs. H. L. Pécseli and J. K. Trulsen for their interest and many

valuable discussions on the subject.

REFERENCES

Bell, A. B. 1978, MNRAS, 182, 147

Blandford, R. D. & Ostriker, J. P. 1978, Astrophysical Journal, 221, L29

Burrows, R. H., Zank, G. P., Webb, G. M., Burlaga, L. F., & Ness, N. F. 2010, The Astrophysical Journal, 715, 1109

Carbajal, L., Dendy, R. O., Chapman, S. C., & Cook, J. W. S. 2014, Physics of Plasmas, 21, 012106

Cauffman, S., Majeski, R., McClements, K., & Dendy, R. 1995, Nuclear Fusion, 35, 1597

Chapman, S. C., Lee, R. E., & Dendy, R. O. 2005, Space Science Reviews, 121, 5

Cook, J. W. S., Chapman, S. C., & Dendy, R. O. 2010, Physical Review Letters, 105, 255003

Cook, J. W. S., Chapman, S. C., Dendy, R. O., & Brady, C. S. 2011a, Plasma Physics and Controlled Fusion, 53, 065006

Cook, J. W. S., Dendy, R. O., & Chapman, S. C. 2011b, Plasma Physics and Controlled Fusion, 53, 074019

—. 2013, Plasma Physics and Controlled Fusion, 55, 065003

Cottrell, G. A., Bhatnagar, V., Costa, O. D., et al. 1993, Nuclear Fusion, 33, 1365

Dendy, R., McClements, K., Lashmore-Davies, C., et al. 1995, Nuclear Fusion, 35, 1733

Dendy, R. O., LashmoreDavies, C. N., McClements, K. G., & Cottrell, G. A. 1994, Physics of Plasmas, 1, 1918

Dendy, R. O. & McClements, K. G. 1993, Journal of Geophysical Research, 98, 15531

Dieckmann, M. E., Eliasson, B., Shukla, P. K., Sircombe, N. J., & Dendy, R. O. 2006, Plasma Physics and Controlled Fusion, 48, B303

Dieckmann, M. E., McClements, K. G., Chapman, S. C., Dendy, R. O., & Drury, L. O. 2000, Astronomy & Astrophysics, 356, 377

Ellison, D. C., Drury, L. O., & Meyer, J.-P. 1997, Astrophysical Journal, 487, 197

Ellison, D. C., Slane, P., & Gaensler, B. M. 2001, Astrophysical Journal, 563, 191

Enomoto, R., Tanimori, T., Naito, T., et al. 2002, Nature, 416, 423

Fermi, E. 1949, Physical Review, 75, 1169

Hellinger, P., Travnicek, P., & Matsumoto, H. 2002, Geophysical Research Letters, 29, 2234

Henry, R. C. B. 1986, Publ. Astron. Soc. Pacific, 98, 1044

Kirk, J. G. & Dendy, R. O. 2001, Journal of Physics G: Nuclear and Particle Physics, 27, 1589

Koyama, K., Petre, R., & Gotthelf, E. V. 1995, Nature, 378, 225

Lapenta, G. 2012, Journal of Computational Physics, 231, 795

Lee, R. E., Chapman, S. C., & Dendy, R. O. 2004, Astrophysical Journal, 604, 187

—. 2005a, Physics of Plasmas, 12, 012901

—. 2005b, Annales Geophysicae, 23, 643

Lembege, B. & Savoini, P. 1992, Physics of Fluids B: Plasma Physics, 4, 3533

Lucek, S. G. & Bell, A. R. 2000, MNRAS, 314, 65

McClements, K., Dieckmann, M. E., Ynnerman, A., Chapman, S., & Dendy, R. 2001, Physical Review Letters, 87, 255002

McClements, K. G. & Dendy, R. O. 1993, Journal of Geophysical Research, 98, 11689

McClements, K. G., Dendy, R. O., Drury, L. O., & Duffy, P. 1996, MNRAS, 280, 219

Schmitz, H., Chapman, S. C., & Dendy, R. O. 2002a, Astrophysical Journal, 579, 327

—. 2002b, Astrophysical Journal, 570, 637

Scholer, M., Shinohara, I., & Matsukiyo, S. 2003, Journal of Geophysical Research, 108, 4